COMPUTATIONAL FLUID DYNAMICS ANALYSIS OF ORIFICE PLATE METERING SITUATIONS UNDER ABNORMAL CONFIGURATIONS

Dr W. Malalasekera

Version 3.0

August 2013

COMPUTATIONAL FLUID DYNAMICS ANALYSIS OF ORIFICE PLATE METERING SITUATIONS UNDER ABNORMAL CONFIGURATIONS

1. Introduction

Orifice plates are widely used in oil and gas industries to measure flow rates. These orifice plate configurations need to satisfy plate metering standard, ISO 5167, and conform to numerous criteria [1, 2]. Due to various reasons orifice plate configurations and installations may not conform to these standards. The problem considered in this work is such an unusual situation where the orifice plate has been placed in an incorrect manner and the work undertaken here considers the flow analysis using computational fluid dynamics (CFD) in this unusual configuration. In this work a CFD analysis is used to predict resulting differential pressure (DP) under this abnormal geometry configuration. The developed CFD models are verified and validated by comparing the model results with measurements taken in normal conditions as well as with experimental measurements taken under abnormal conditions.

1.1 Principles of orifice plate flow measurements

The basic principle of orifice plate flow measurements is based on the measurement of pressure loss when an orifice plate is installed in a pipe line carrying the fluid (in this case natural gas). Shown in Figure 1 is a typical orifice plate. Orifice plates used in practice should conform to standards such as ISO 5167. Therefore dimensions, tolerances, installation details, positions of pressure tappings for pressure drop measurements etc. are all specified by standards (ISO 5167). Under such standard conditions the mass flow rate, q_m, can be obtained using equation (1):

$$q_m = \frac{C}{\sqrt{\left(1 - \beta^4\right)}} . \varepsilon . \frac{\pi d^4}{4} \sqrt{2 \Delta p . \rho_1} \tag{1}$$

Where $\beta = d/D$
$\Delta p \equiv$ Pressure difference across the orifice plate (Pa)

$D \equiv$ Pipe diameter (m)

$d \equiv$ Orifice diameter (m)

$C \equiv$ Coefficient of discharge (function of Re number and β)

$\varepsilon \equiv$ Expansibility factor (function of $p_2/p_1, \beta$, κ the isentropic exponent, and temperature)

$\rho_1 \equiv$ Fluid density (kg/m³)

Equations are available for the calculation of c and ε in ISO-5167.

1.2   Orifice plate geometrical data

Figure 1 shows dimensions used in characterising a typical orifice plate. In operation an orifice plate is placed with its centre concentric with the centre of the pipe cross section. The locations of the pressure tappings (Figure 2) are also specified in ISO 5167. ISO-5167 specifies that l_1^d and l_2^d shown in Figure 2 should be 25.4 ±1 mm.

Figure 1. Geometrical details of an orifice plate.

Figure 2. Pressure tapping for orifice plates.

1.3   Flow under abnormal conditions

The above formula (1) is used in the determination of the flow rate under standard conditions. Under normal operating conditions the centre of the orifice plate should be in line with the centre line of the pipe. Any misalignment or geometrical abnormalities will result in an erroneous measurement as the above orifice plate formula is based on an axisymmetric geometry. The problem considered here is a situation where an error has occurred due to misalignment of an orifice plate. The error has been caused by severe misalignment of an orifice plate in the pipe as illustrated in Figure 3. Here CFD modelling is used to support physical on site flow rate tests in this configuration.
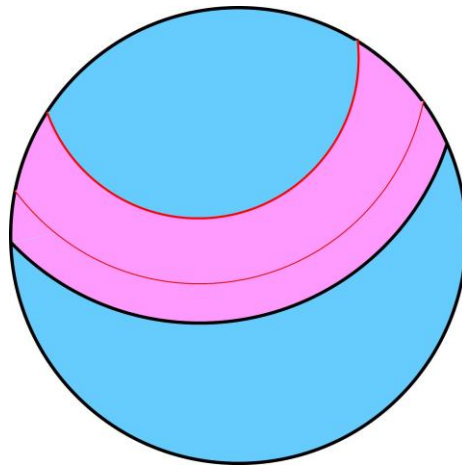
Figure 3. An illustration of a misaligned orifice plate – cross sectional view.

1.4 Orifice plate installations

Typical orifice plate installations used in gas industry use an orifice plate carrier arrangement to change orifice plates from time to time. The carrier arrangement used in the problem considered here is shown in Figure 4(a) and (b). Figure 4 (a) is the outside view of the arrangement and Figure 4(b) is a cross sectional view of the geometry. This kind of carrier arrangement allows for changing of the plate without de-pressurising the pipe-line by having a chamber above the pipe which can be isolated to remove the plate. The orifice plate is inserted through the top side opening of the geometry. Inside the carrier geometry, there is a carrier mechanism that is operated by a screw and lowers the orifice plate, held by an arm attached to the screw mechanism, into the pipe position and places it at the correct position which has been preset by appropriately adjusted locating screws at the bottom of the geometry. However if the screw winding mechanism is not wound down to the correct position the orifice plate which is held by the carrier arm may not be at the correct concentric position inside the geometry. The position of the orifice is gauged by an indicating counter at the top of the carrier geometry.
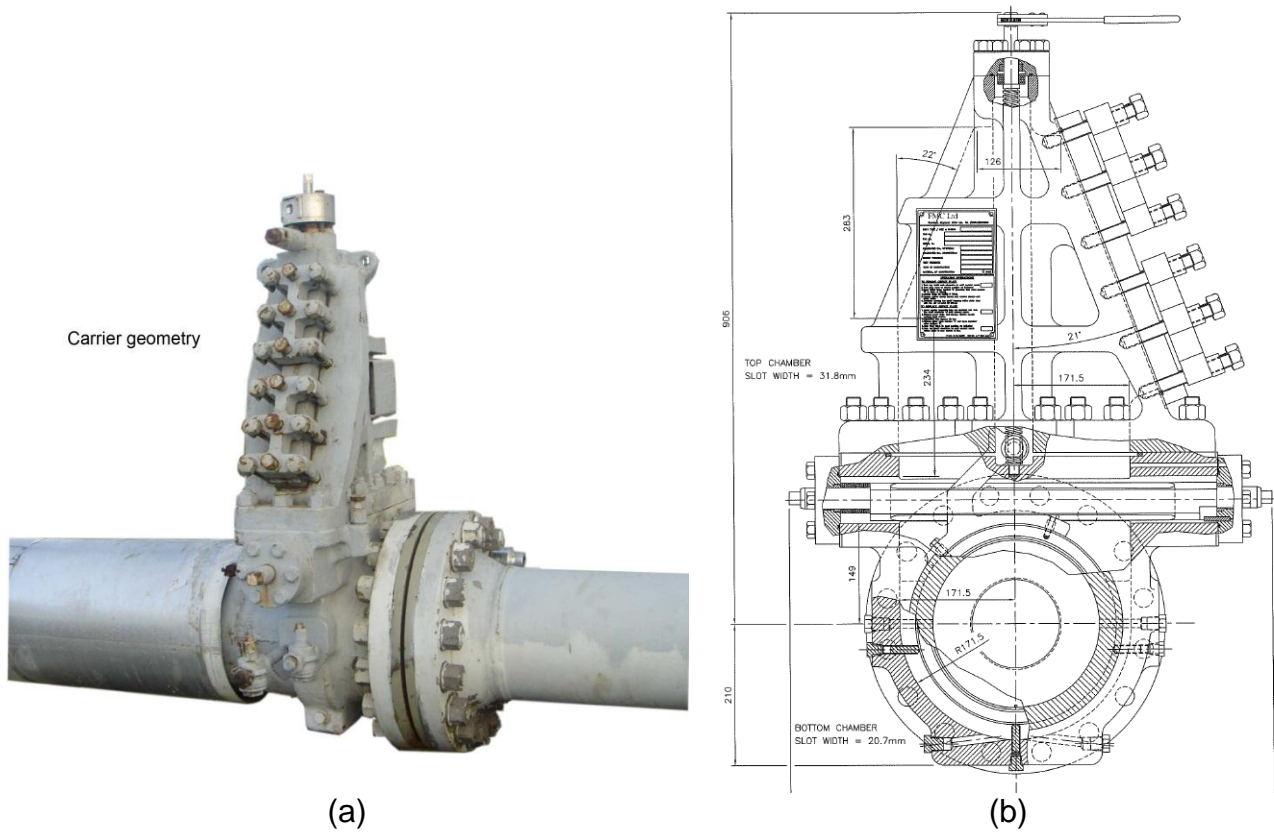
Figure 4 – An illustration of the orifice plate installation considered in this study.

The problem considered here is a situation where the orifice plate has not been wound down correctly to its correct position hence creating a misaligned orifice plate situation as shown in Figure 3.

1.5 Objectives of the CFD study and its remit

In this work a comprehensive CFD model, based on the complex geometry including the carrier chamber is constructed with the view of analysing and visualising the flow conditions resulting from different misalignment positions of the orifice plate. The primary aim of the CFD model is to predict DP for given flow rates in configurations with severe misalignment of the orifice plate. Experiments have been conducted to measure resulting DP values under various flow rates at different misaligned positions of the orifice plate. Results obtained from CFD will be compared against experimental data from site experimental tests. Data is also available to validate the CFD model for correctly aligned orifice plate positions. Resulting CFD predicted DP values will also serve as a confirmation of the experimental data and would be used to explain resulting flow features due to misalignment.

2. Outline of the CFD model

The CFD analysis in this case is conducted in two stages. In the first stage an orifice plate flow model is created for correctly placed orifice plate configurations. When the orifice plate is in the correct position the upper chamber of the geometry is completely sealed-off from the main flow and the geometry is a simple configuration which includes a straight pipe and an orifice plate. Measured data in the form of pressure drop and flow rates are available to validate simple orifice plate models. In the second stage of modelling, complex geometry models including the upper chamber of the carrier geometry are constructed and the orifice plate is placed at eccentric misaligned positions depending on the case considered. Experimental data obtained in site tests for several misaligned orifice plate positions are available for the validation of the second stage of modelling.

3. Carrier geometry details and other data

3.1 Carrier geometrical data

Detailed drawings of the carrier geometry were available for the construction of a model of the carrier geometry and the chamber above the pipe. For example, the drawing Figure 4(b) shows the cross-section of the carrier geometry. In addition, measured site data for the orifice plate arm dimensions and corresponding orifice plate centre positions for various positions of the carrier screw settings were also available. Carrier screw positions are identified by a set of numbers. Due to the way the screw mechanism is designed to operate, the orifice plate centre position can have different eccentric positions depending on whether the plate is inserted in or taken out. Figure 5 for example shows a site photograph of the orifice plate position inside the pipe for the winding-in position identified as 99984. The centre of the orifice plate is misaligned (from the centre of the pipe cross-section) in both vertical and horizontal directions as the plate moves sideways during insertion and extraction. During the experiments the positions of the centre of the orifice plate for various screw positions have been measured with respect to the fixed pipe diameter. Figure 6 shows the two parameters A and B used in the identification of the orifice centre position. Table 1 shows the measured A and B parameters for various screw positions when the plate is moving upwards against counter reading and Table 2 shows the measured A and B values when the plate is moving downwards along the counter readings. In the simulation cases considered later, A and B values when the plate is moving downwards have been used. For the case known as 99985 interpolated A and B values from Table 2 are used.
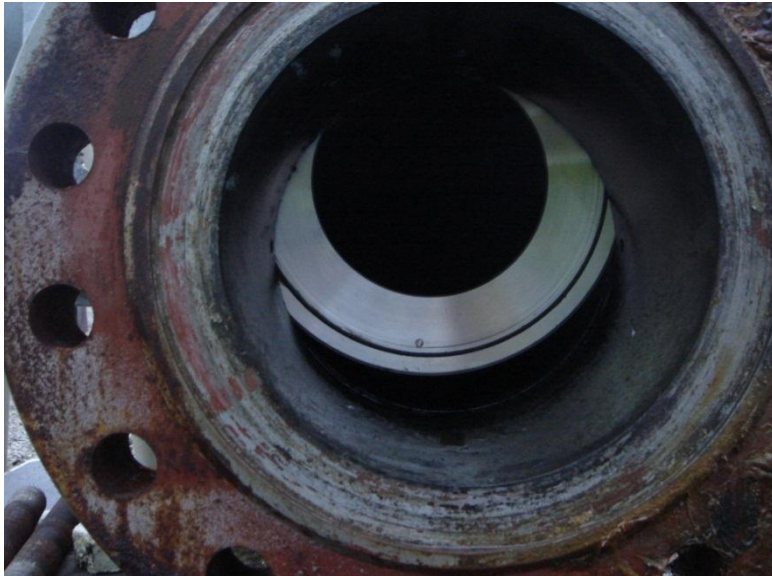
Figure 5. Photograph of the orifice plate position for the counter reading 99984 during winding-in.
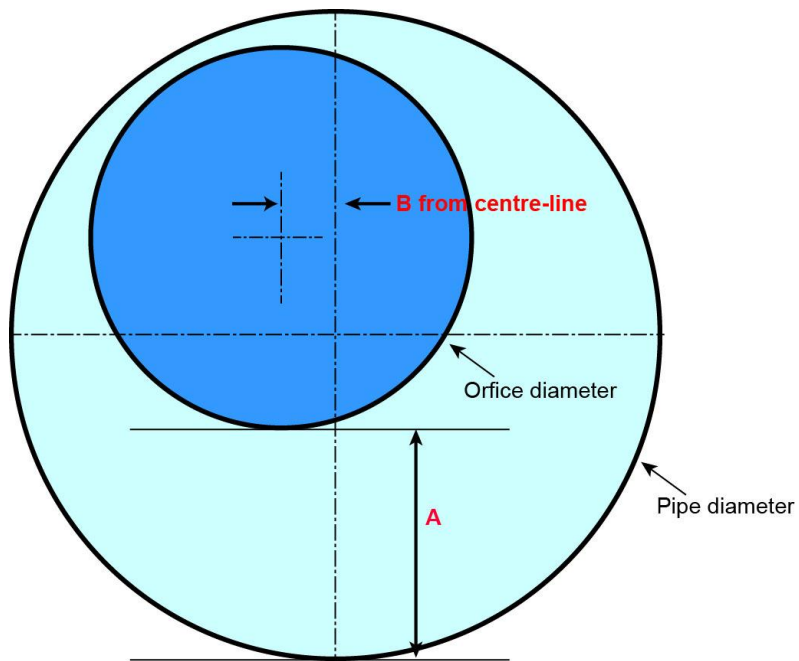

Figure 6. Illustration of the parameters A and B used to identify the orifice plate position.

Table 1 – Position of the orifice plate centre moving upwards against counter reading

Counter reading	A Position (mm)	B+ Position (mm)
00001	39.0	0.0
99995	50.4	0.0
99984	88.7	11.5
99970	137.9	17.5
99960	174.0	24.5
99950	209.8	22.5
99940	244.0	14.5

Table 2 – Position of the orifice plate centre moving downwards along the counter reading

Counter reading	A Position (mm)	B- Position (mm)
00040	245.5	22.5
99950	210.5	22.5
99960	175.0	26.5
99970	139.1	25.5
99984	90.8	19.5
99995	52.5	0.0
00000	39.0	0.0

3.2 Pipe layout details of the installation

The pipe layout at the location is shown in Figure 7. Upstream of the orifice fitting the pipe run has a length of twenty-two pipe diameters (22D) to a flanged spool piece connection of two diameters (2D) in length. Upstream of this spool piece is another straight length of 20D to a 10" to 12" expander followed by a full flow isolation ball valve. Some distance upstream, the pipe enters underground at an angle of 45°.

Figure 7. Photograph of the site and pipe layout near the metering location

Immediately downstream of the orifice fitting there is a flanged section of pipe approximately 6D in length. A further section of straight pipe extends to 12D where there is a 90° bend. A 4-wire RTD temperature element is installed in a thermowell at 9D downstream of the orifice plate. These details are incorporated in constructing upstream and downstream pipe lengths of the model. Details and dimensions of the thermowell are shown in Figure 8.
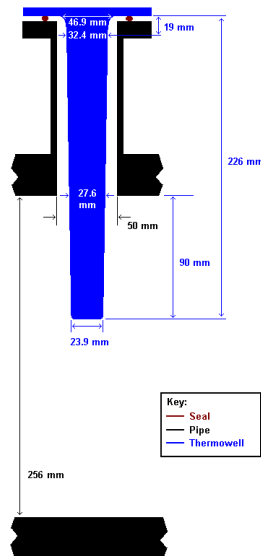

Figure 8. Details of the Thermowell.

4. General details of the CFD modelling methodology

CFD models used in the analysis solve fundamental fluid flow governing equations given by the Navier-Stokes equations. The method is based on the finite volume technique where the geometry is divided into a large number of cells known as a mesh. In each of these cells, discretised Reynolds Averaged Navier-Stokes (RANS) equations are solved with a turbulence model to calculate time averaged flow properties. Here the CFD calculations are treated as incompressible. The procedure is based on the SIMPLE algorithm. Full details of the equations used, turbulence model details, the pressure based SIMPLE algorithm and discretisation techniques are described in reference [3]. In the construction of models, all geometrical details have been incorporated as accurately as possible. Orifice plate edge details have been incorporated into models according to details given in plate certificates and pipe lengths before and after the orifice plate location have been selected to provide most accurate boundary conditions. References [4-6] provide some guidance for the selection of inlet and outlet pipe lengths for orifice plate numerical calculations. During the peer review of the work presented here it was proposed to shorten the selected lengths to 2D upstream and 10D downstream of the orifice plate. This recommendation was implemented and a series of test cases were run with a shorter model. The results obtained with a shorter model did not produce better results than the longer model (the full model) presented in this report. For information, the results of the shorter model for a complete test series are presented in Appendix A. A separate pipe flow calculation is carried out to obtain a fully developed flow profile for the inlet boundary condition. Given flow rate data are used as inlet boundary conditions in the inlet pipe flow calculation. Fluid flow properties are set as Methane. From the data supplied the actual flow rate (kg/h), density and viscosity are the main inputs for CFD models. For all flow rates considered, calculated Reynolds numbers ($\mathrm{Re} = \rho u D / \mu$) indicate that the flow is fully turbulent in all cases. Therefore the well-known $k - \varepsilon$ turbulence model which solves equations for turbulence kinetic energy and turbulence energy dissipation rate is used as the turbulence model option. Other turbulence model options such as $k - \omega$ SST were tested in the initial stages of modelling and the results showed that that the $k - \varepsilon$ turbulence model provided the best overall results across the entire model series considered in this study. The simulations give detailed flow and pressure fields and the results are then post-processed to visualise the flow behaviour and obtain relevant important parameters. Here the CFD predicted DP is obtained from the solutions and compared against the measured DP values.

Mesh construction for CFD model is also given adequate attention. Geometry is subdivided into appropriate zones so that different mesh models could be adopted to achieve desired mesh distributions. In this process complex geometry areas are meshed with tetrahedral elements while hexahedral meshes are employed in other areas as much as possible.

In all CFD models nonslip wall boundary conditions are applied at wall boundaries and wall roughness for pipe internal surfaces are taken to be 32.6 Ra. Orifice plate surfaces and edges are considered to be smooth. Applying wall boundary condition in CFD models also requires a parameter known as y+ to be maintained between 11 and 500 at wall boundaries. To achieve this careful consideration is given during the construction of meshes to satisfy this requirement. For this purpose, boundary layer meshes are incorporated at all possible wall boundaries to maintain y+ within required limits. In each simulation case presented later in this report three levels of meshes (grids) are employed to perform CFD calculations. This provides an indication of grid independence of the CFD results and in most cases it is shown that there is very small difference between the results of two finer level meshes.

5. CFD models of standard orifice plate metering situations

Here as validation exercises CFD analysis is conducted for three standard orifice plate metering situations, i.e. when the orifice plate is correctly positioned in the pipe. For reporting purposes these three test cases are referred to as Case 1, Case 2 and Case 3. Case 1 and 2 have low flow rates compared to the high flow rate in Case 3. The mass flow rate, density and viscosity are used to specify the problem boundary conditions and properties. Orifice plate dimensions are taken from the test certificates corresponding to measurements. Orifice plate edge details and bevel angle etc. have been accurately incorporated in constructing geometries for each case. In the model a 2 m pipe length is used as the inlet section before the metering location. A separate pipe flow CFD calculation is used to obtain a fully developed inlet flow profile for the main model. Downstream pipe lengths are selected from pipe-layout details given in Section 3.2. After the metering location (orifice plate) a pipe length of 18D is used before the bend and then a further 15m pipe length is used after the bend. The thermowell is placed at 9D after the orifice plate.

5.1 Operating conditions and simulation data

The measured flow rates and corresponding properties are considered in the simulations. Table 5 below summarises the data considered and the properties.

5.2   Model details

The CFD model used here solves time averaged Navier-Stokes equations based on the CFD methodology outlined in section 4. From the data supplied in Table 5 the actual flow rate (kg/h), density and viscosity are the main inputs to CFD models. The simulations give detailed flow and pressure fields and the results are then post-processed to visualise the flow behaviour by plotting vector and contour plots. DP in each metering situation is obtained from the model by extracting static pressure values at pressure tapping locations. It should be noted that the static pressure reported here is the relative static pressure where the reference point is the inlet plane. In CFD calculations actual pressure is not required. In solving momentum equations pressure gradients in respective directions drive the momentum equations, therefore relative pressure is used. Here the CFD predicted DP is obtained from the solution at pressure tapping locations and compared against the measured DP values.

5.3   Orifice plate geometrical data – Case 1, 2 and 3

Data from the test certificate corresponding to measurements are used. Table 3 summarises key data used in the construction of the model for Cases 1 and 2. This data has been taken from the orifice plate with serial no. 050/4. Parameters used in Table 3 are marked in Figure 1. Table 4 shows the orifice plate data for Case 3. The orifice plate used for Case 3 is the orifice plate with serial no. 050/2. These details are incorporated in the construction of CFD geometries.

Table 3 – Orifice plate data: Plate id. 050/4

Parameter	Value
Pipe diameter (D)	256.466 mm
Orifice diameter (d)	177.2103 mm
Diameter ratio (β)	0.6909
Plate thickness (E)	6.262 mm
Edge thickness (e)	3.1 mm
Bevel angle (α)	45 °

Table 4 – Orifice plate data: Plate id. 050/2

Parameter	Value
Pipe diameter (D)	256.446 mm
Orifice diameter (d)	177.154 mm
Diameter ratio (β)	0.6908
Plate thickness (E)	6.308 mm
Edge thickness (e)	4.699 mm
Bevel angle (α)	38.3 °

Table 5 – Flow data and properties for test cases 1, 2 and 3

		21-Jul-09	10-Aug-10	Test 3
CFD Case identification		**Case 1**	**Case 2**	**Case 3**
DP (measured)	**mbar**	**12.947**	**24.433**	**439.41**
Temperature	deg C	13.399	13.548	10.09
Std Volumetric Flow Rate	scm/h	30111	42094	178737
Orifice Plate Bore Diameter @ cal T	mm	177.2103	177.2128	177.1536
cal T	deg C	19.8	20.2	20.4
Orifice Plate Bore Diameter @ line T	mm	177.1922	177.1939	177.1243
Pipe Internal Diameter @ cal T	mm	256.4660	256.4661	256.4661
cal T	deg C	20.0	20.0	20.0
Pipe Internal Diameter @ line T	mm	256.4474	256.4479	256.438
Isentropic Index		1.34935	1.35652	1.36448
Dynamic Viscosity	**Pa.s**	**0.0000124**	**0.0000125**	**1.24389E-05**
Density	**kg/m^3**	**56.005**	**57.184**	**57.653**
Mass Flow Rate	**kg/h**	**23201.215**	**32445.017**	**137047.908**
Actual Volumetric Flow Rate	**m^3/h**	**414.2697**	**567.3747**	**2377.10757**

5.4   Measurement uncertainties

Depending on the rate of flow and recorded DP, flow meters have certain level of uncertainties. Figures 9 and 10 below show the estimated uncertainty of measurements for different DP ranges. It can be seen that low DP recordings are subject to higher uncertainties and high DP values have much lower uncertainties. Comparison of predicted DP should be viewed in relation to uncertainties of the measurements.
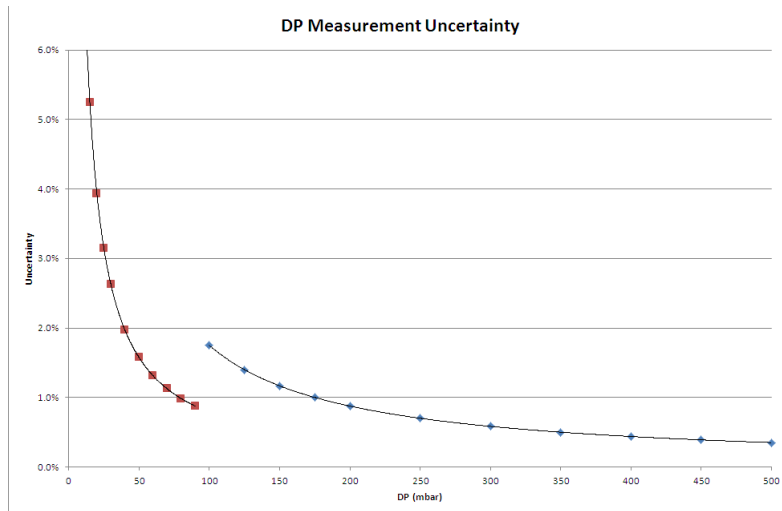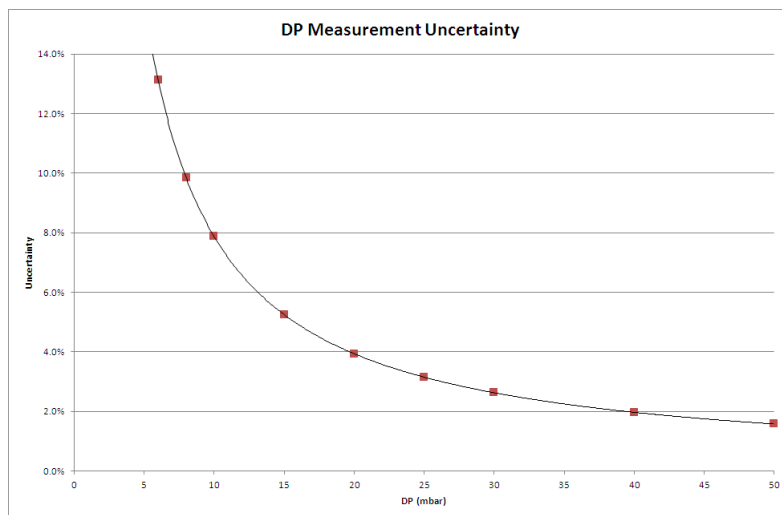

Figure 9. DP measurement uncertainty at high DP range

Figure 10. DP measurement uncertainty at low DP range

5.5   Results – Case 1

For Case 1 the actual flow rate of 414.2697 m³/h is used as the inlet boundary condition. Density ρ = 56.005 kg/m³ and viscosity μ = 0.0000124 Pa.s. Three CFD grids have been used to perform CFD calculations. These grids are identified as Grid 1, Grid 2 and Grid 3. In general all grids have been designed to incorporate and represent geometrical details as accurately as possible and fine details of the orifice plate edges and bevel angles have been represented by placing very small elements along those edges. Grid 1 contained 2324882 (2.32 million) elements, Grid 2 contained 2872671 (2.87 million) elements and Grid 3 contained 2997933 (3.00 million) elements. As explained in section 4, a combination of tetrahedral and hexahedral elements has been used in the meshing. Figure 11 shows a portion of the Grid 3 used in these simulations. The results presented below have been conducted using the $k - \varepsilon$ turbulence model. In the solution process the second order upwind discretisation scheme was used for all equations. Grid 3 results are used in the presentation of graphical description of the results. For Case 1, calculated static pressure distribution across a central plane through the orifice plate is shown in Figure 12. Figure 13 shows the pressure distribution along a line very near the pipe wall. It can be seen that there is a sudden drop in pressure across the orifice plate. The measured DP value given in Table 5 for this case is 12.94 mbar. Results of CFD predicted values using three levels of grids are compared with this and shown in Table 6. The difference between the CFD predicted DP and the experimental value are 1.5% for the coarse mesh calculation and less than 1% for the two fine mesh calculations. Figure 10 indicate that the uncertainty of the measurements for this range of DP is between 5 – 6%. Therefore the agreement between CFD predicted DP values and the measured value is very good. Table 5 also shows that CFD results of Grid 2 and 3 are very close and the difference between the two fine grid calculations is only 0.3%. Figure 14 shows contours of axial velocity through the central mid x-y plane. This illustrates the flow acceleration through the orifice and the recirculation patterns behind the orifice plate indicated by negative axial velocities.
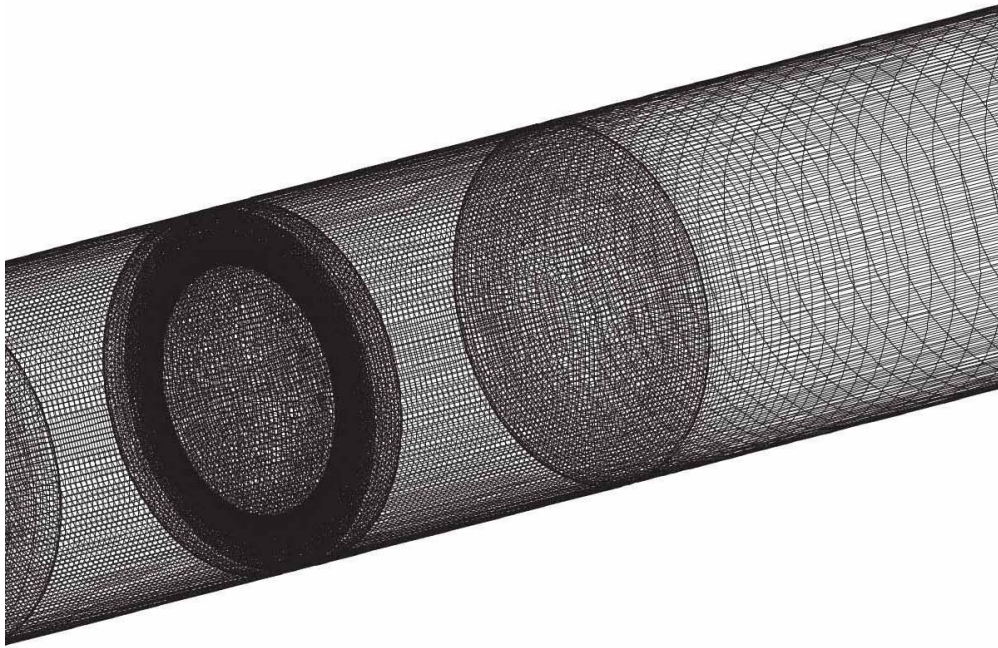
Figure 11 Case 1 – A section of the CFD Grid 3

Table 6 Comparison of CFD results with experimental data for Case 1

Case 1 – With correct orifice position and a flow rate of 414.2697 m^3/h				
	DP (mbar)	% Error between CFD and experimental	Uncertainty of measurements	Difference in error between simulations
Measured value	12.94			
CFD Simulation 1 – Grid 1 (2324882 cells)	12.74	1.5%	5 – 6%	
CFD Simulation 2 – Grid 2 (2872671 cells)	12.82	0.9%	5 – 6%	between 1 & 2 0.6%
CFD Simulation 3 – Grid 3 (2997933 cells)	12.85	0.6%	5 – 6%	between 2 & 3 0.3%
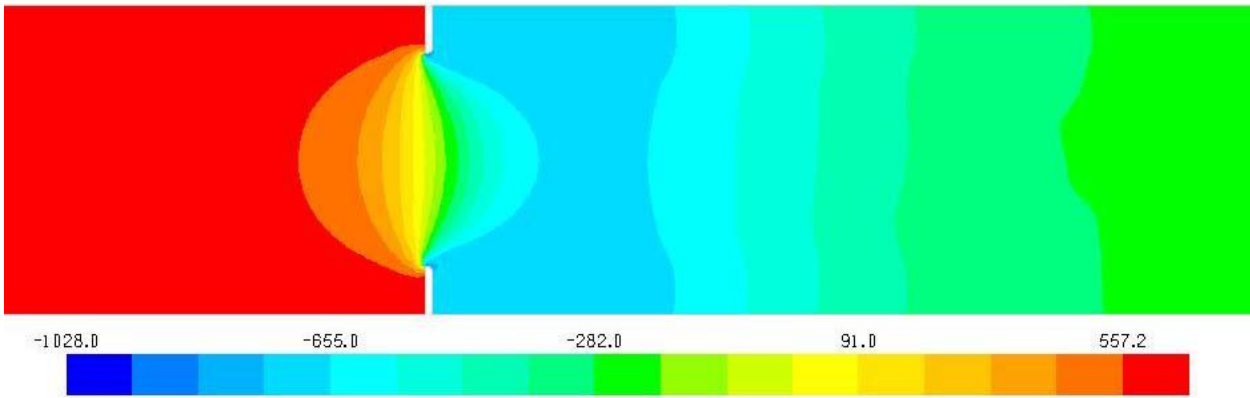
Figure 12. Case 1 – Relative static pressure distribution at an x-y mid plane through the orifice plate.
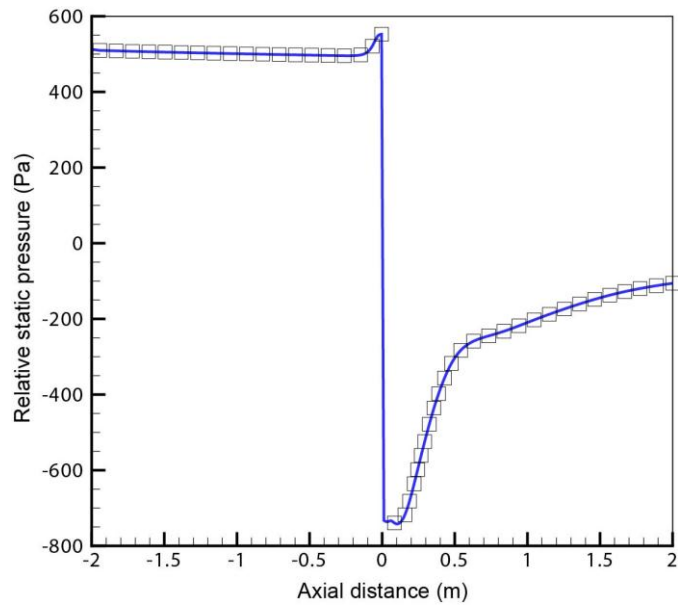

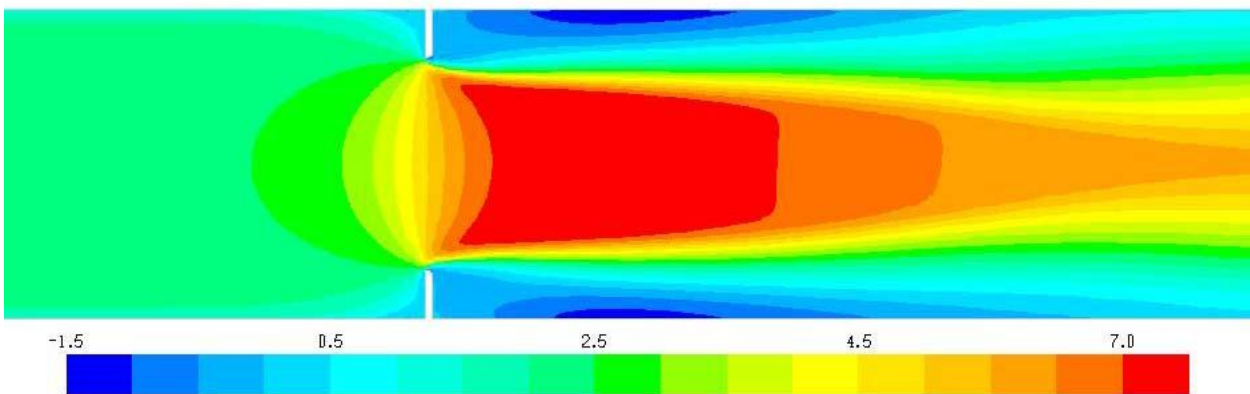Figure 13 – Case 1 Pressure distribution along the pipe wall.

Figure 14. Case 1 – Contours of axial velocity at an x-y mid plane through the orifice plate.

5.6   Results – Case 2

For Case 2 the actual flow rate of 567.3747 m^3/h is used as the inlet boundary condition. Density ρ = 57.184 kg/m^3 and viscosity μ = 0.0000125 Pa.s. Grid 3 simulations are used in the illustration of flow features. For Case 2, calculated static pressure distribution across a central plane through the orifice plate is shown in Figure 15. Figure 16 shows the pressure distribution along a line very near the wall. The measured DP value given in Table 5 for this case is 24.43 mbar. Results of CFD predicted values using three levels of grids are compared with this and shown in Table 7. In the Grid 2 calculation the difference between the CFD predicted DP and the experimental value is 0.5%. In Grid 1 and Grid 3 calculations the error is 0.2%. The uncertainty of the measurements for this range of DP is between 5 – 6%. Therefore the agreement between CFD predicted DP values and the measured value are very good. Table 7 also shows that CFD results of Grid 2 and 3 are very close and the difference between the two fine grid calculations is only 0.3%. Figure 17 shows contours of axial velocity through the central mid x-y plane in this case. This shows the flow acceleration through the orifice and the recirculation patterns behind the orifice plate indicated by negative axial velocities.

Table 7 Comparison of CFD results with experimental data for Case 2

| Case 2 – With correct orifice position and a flow rate of 567.374 m^3/h				
	DP (mbar)	% Error between CFD and experimental	Uncertainty of measurements	Difference in error between simulations
Measured value	24.43			
CFD Simulation 1 – Grid 1 (2324882 cells)	24.50	0.2%	5 – 6%	
CFD Simulation 2 – Grid 2 (2872671 cells)	24.57	0.5%	5 – 6%	between 1 & 2 0.3%
CFD Simulation 3 – Grid 3 (2997933 cells)	24.50	0.2%	5 – 6%	between 2 & 3 0.3%
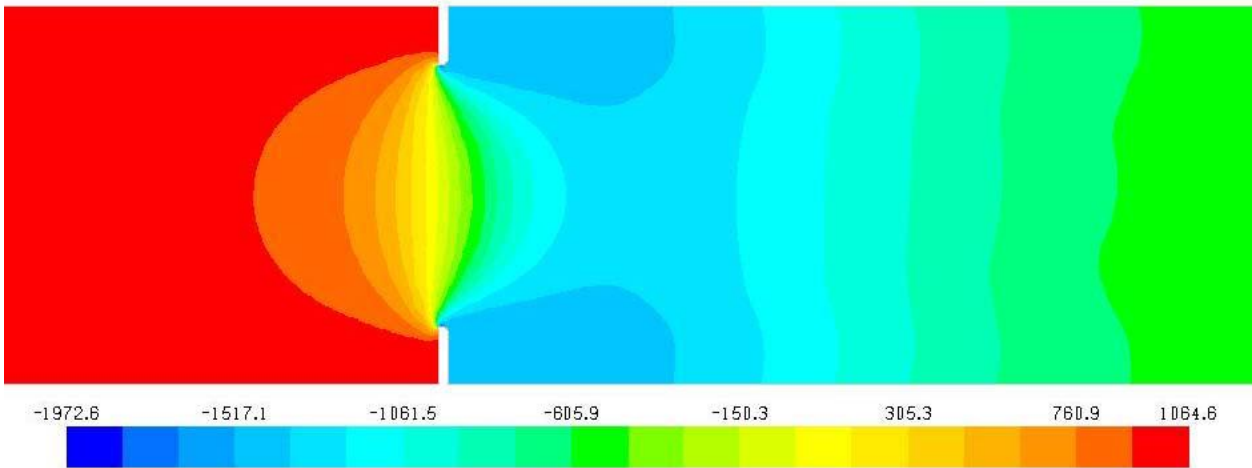
Figure 15. Case 2 – Relative static pressure distribution at an x-y mid plane through the orifice plate.
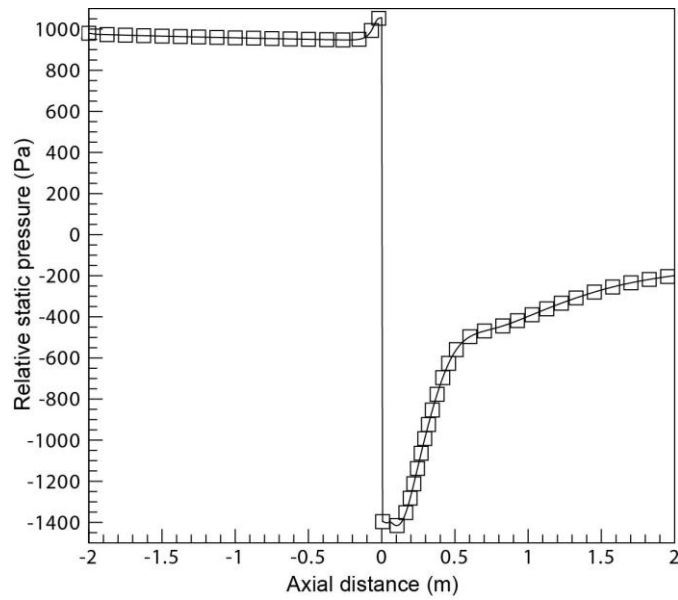

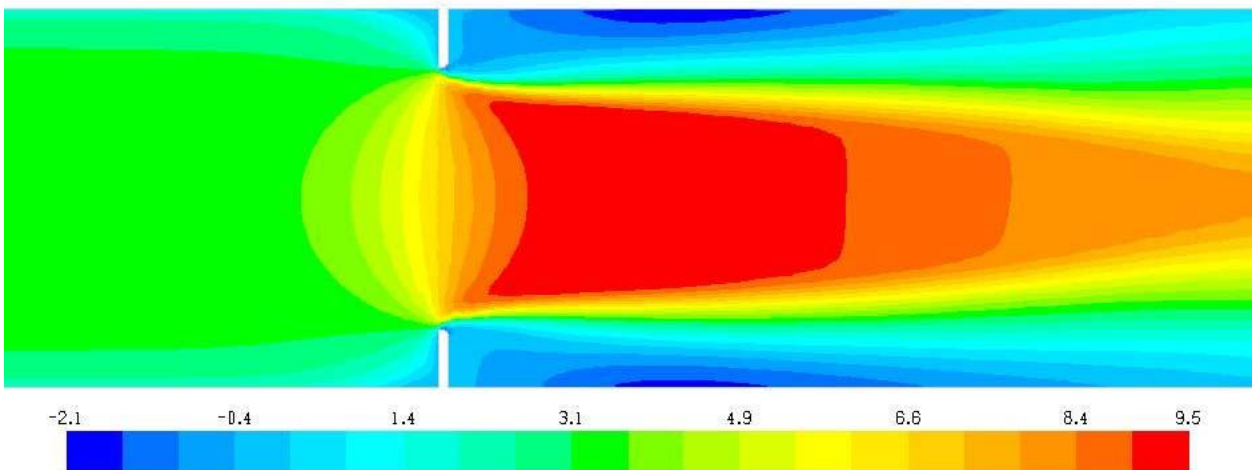Figure 16 Case 2 – Pressure distribution along the pipe wall

Figure 17. Case 2 – Contours of axial velocity at an x-y mid plane through the orifice

plate.

5.7   Results – Case 3

For Case 3 the actual flow rate of 2377.1075 m^3/h is used as the inlet boundary condition. Density ρ = 57.653 kg/m^3 and viscosity μ = 1.24389x10^{-5} Pa.s. Orifice plate data from Table 4 was used in the CFD model. Three grids are used in the simulations. These grids are identified as Grid 1, Grid 2 and Grid 3. All grids have been designed to incorporate and represent geometrical details as accurately as possible and fine details of the orifice plate edges and bevel angles have been represented by placing very small elements along those edges. Grid 1 contained 2347212 (2.35 million) elements, Grid 2 contained 2599239 (2.60 million) elements and Grid 3 contained 3011613 (3.01 million) elements. As explained in section 4, a combination of tetrahedral and hexahedral elements has been used in the meshing (majority hexahedral). A portion of the Grid 3 used in these simulations is shown in Figure 18. For Case 3, calculated static pressure distribution across a central plane through the orifice plate is shown in Figure 19. Figure 20 shows the pressure distribution along a line very near the wall. The measured DP value given in Table 5 for this case is 439.41 mbar. Results of CFD predicted values using three levels of grids are compared with this value and shown in Table 8. The difference between the CFD predicted DP and the experimental value is 0.3% for Grids 1 and Grid 2 calculations and 0.6% for the Grid 3 calculation. The uncertainty of the measurement for this range of DP is less than 1%. Therefore the agreement between CFD predicted DP values and the measured value are very good. Table 8 also shows that the difference between the two fine grid calculations is only 0.3%. Figure 21 shows contours of axial velocity through the central mid x-y plane in this case. This illustrates flow acceleration through the orifice and the recirculation patterns after the orifice.
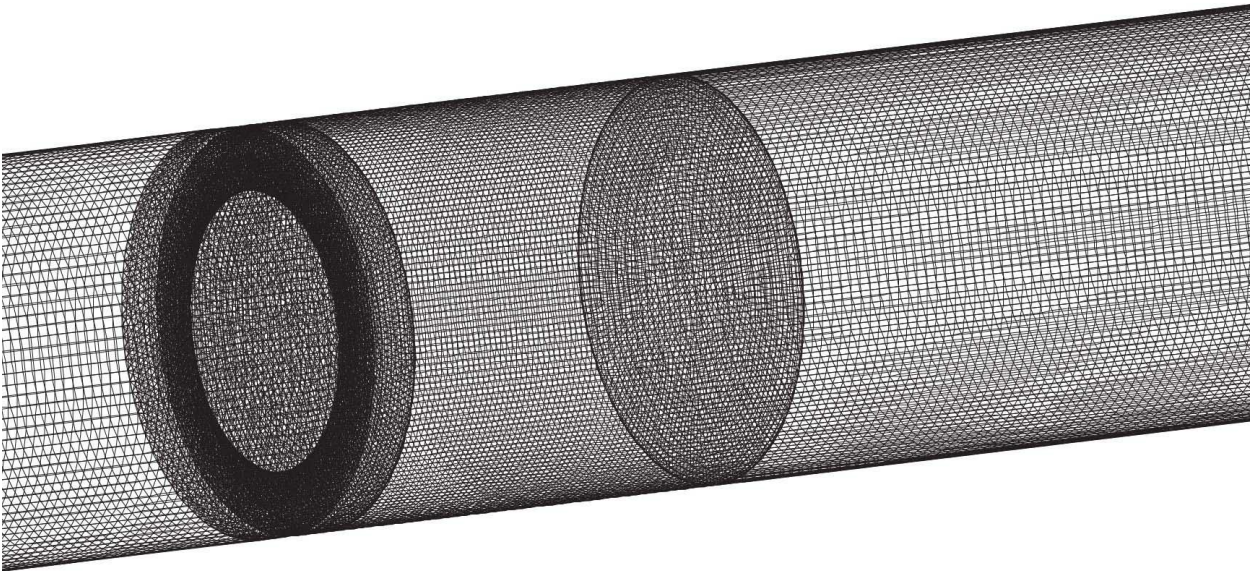
Figure 18. Case 3 – Mid section of CFD mesh used for Case 3.

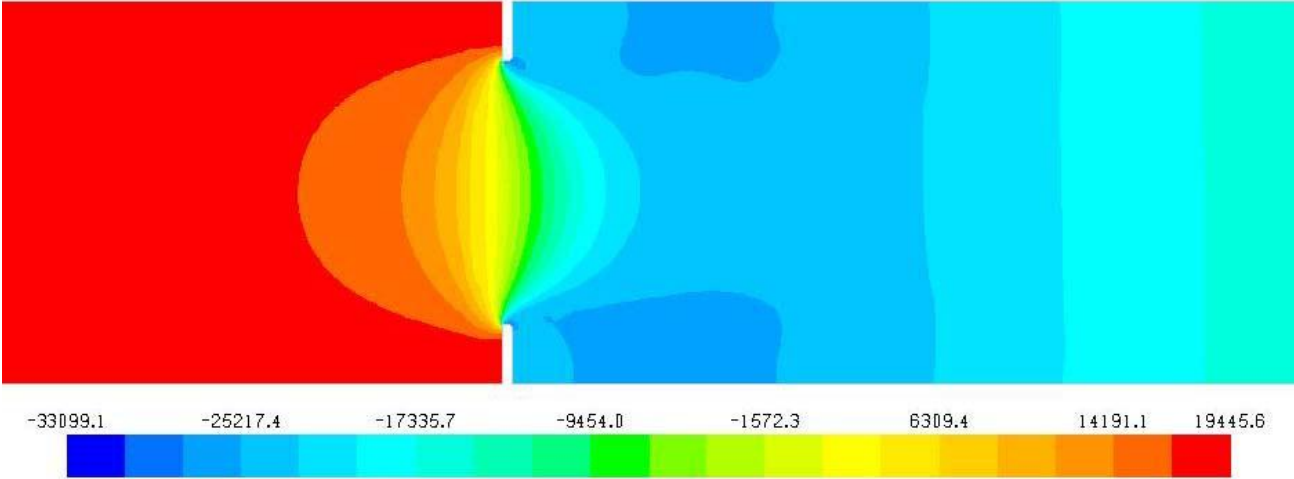| -33099.1 | -25217.4 | -17335.7 | -9454.0 | -1572.3 | 6309.4 | 14191.1 | 19445.6 |

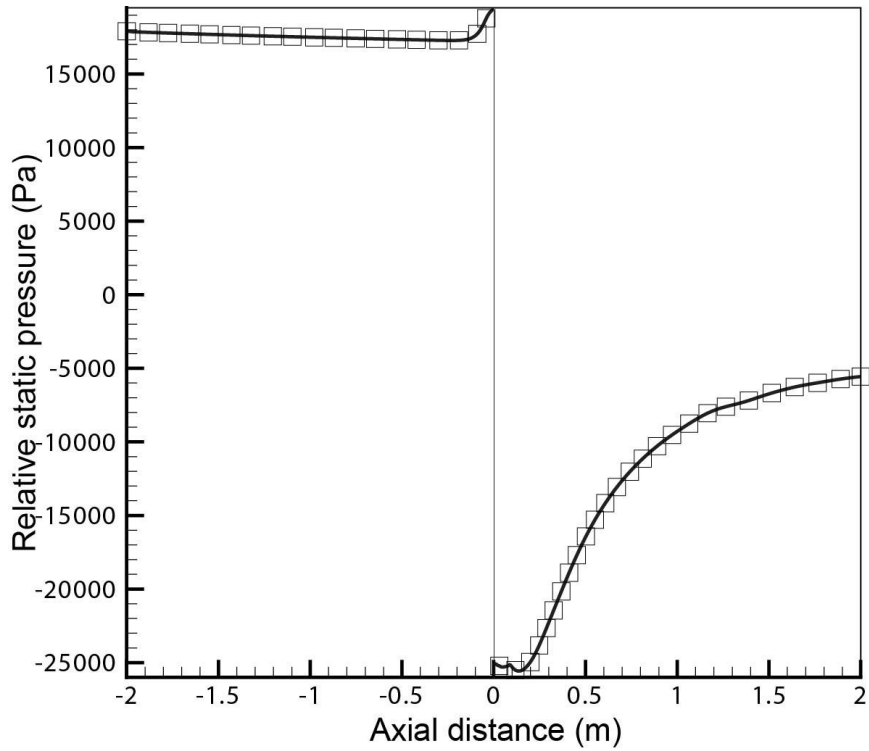Figure 19. Case 3 – Relative static pressure distribution at an x-y mid plane through the orifice plate.

Figure 20 Case 3 – Pressure distribution along the pipe wall

Table 8 Comparison of CFD results with experimental data for Case 3

	DP (mbar)	% Error between CFD and experimental	Uncertainty of measurements	Difference in error between simulations
Case 3 – With correct orifice position and a flow rate of 137047.908 m³/h				
Measured value	439.41			
CFD Simulation 1 – Grid 1 (2347212 cells)	437.87	0.3%	Less than 1%	
CFD Simulation 2 – Grid 2 (2599239 cells)	437.92	0.3%	Less than 1%	between 1 & 2 0%
CFD Simulation 3 – Grid 3 (3011613 cells)	442.41	0.6%	Less than 1%	between 2 & 3

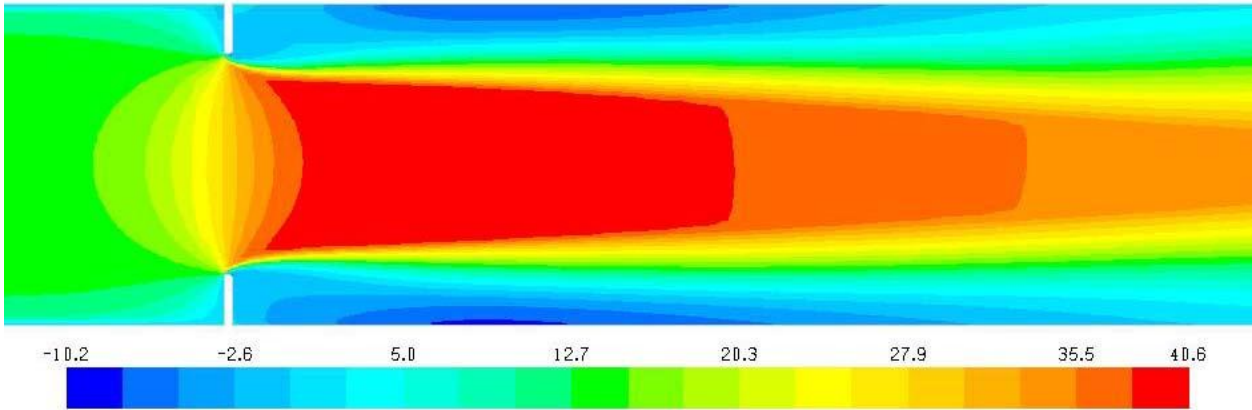|				0.3%

Figure 21. Case 3 – Contours of axial velocity at an x-y mid plane through the orifice plate.

In general it can be seen that CFD methodology used is capable of predicting orifice plate flow situations fairly accurately and the results in all cases have been shown to agree well with experimental data.

6. CFD model of the carrier geometry with eccentric orifice plate positions

The geometry considered here includes the carrier geometry and the orifice plate placed at incorrect positions as described earlier. The geometry is constructed using the drawings provided. When an orifice plate is not in the correct position the upper chamber is exposed to the pipe geometry as the orifice plate is not sealed at the correct position and depending on the position of the orifice plate, a significant part below the skirt of the orifice plate is also fully open to flow. Relevant geometrical details are illustrated below under each case. In construction of the pipe geometry a 2 m pipe length is used for the upstream side of the orifice plate. A separate pipe flow calculation is carried out to obtain inlet flow profile for the inlet. On the downstream side the thermowell is placed at 9D length and the pipe bends after 18D from the orifice location. After the bend a 15m pipe length is used to complete the geometry. Figure 7 shows a photograph of the site arrangement and Figure 22 below shows an outline sketch of the computational model including upstream and downstream pipe sections (applies for cases 99970, 99985 and 99950).
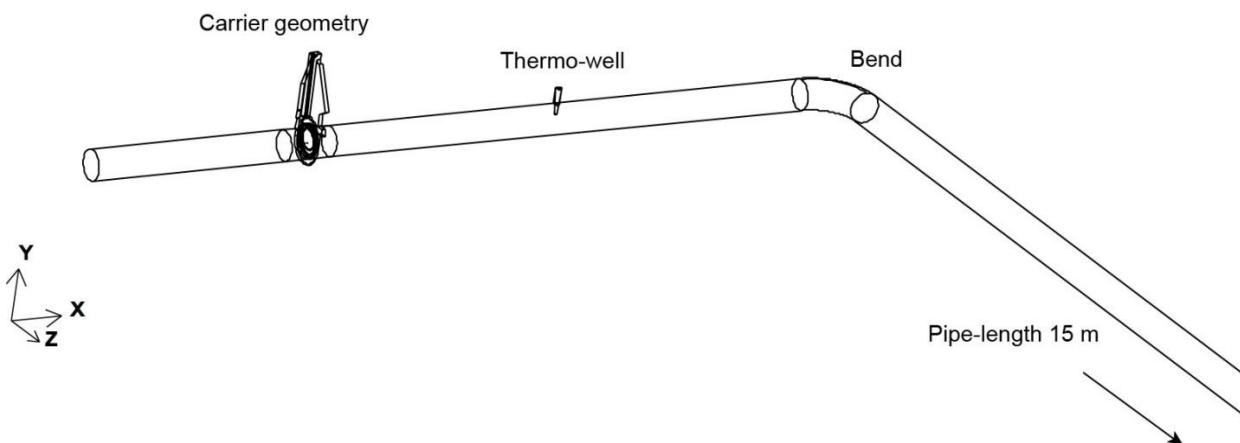
Figure 22. Computational geometry including all pipe lengths, carrier geometry and thermowell.

7. CFD Modelling of test Cases 99970

7.1 The geometry

A selected set of cases from the series of experiments conducted for the orifice plate position identified by 99970 are considered here for the simulations. For this position A and B values for winding down are A = 139.1 mm and B = 25.5 mm. At this position the plate would be touching the carrier geometry and maximum possible B value is used in the

construction. Figure 23 below shows a sketch of the CFD model geometry for the case 99970. Shown in Figure 24 is a view normal to the pipe axis and it shows the degree of eccentricity and the extent of the orifice plate top circumferential part that is inside the upper chamber and open to flow into the chamber. The figure also shows the area under the orifice plate skirt directly open to flow. Table 9 summarises orifice plate data for this case.

Table 9 – Orifice plate data, Plate id: 050/2

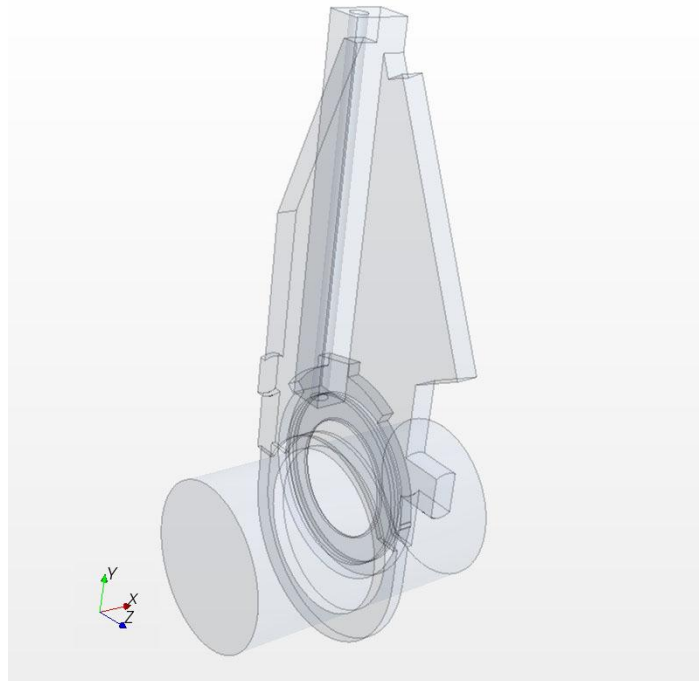| Parameter	Value
Pipe diameter (D)	256.446 mm
Orifice diameter (d)	177.154 mm
Diameter ratio (β)	0.6908
Plate thickness (E)	6.308 mm
Edge thickness (e)	4.699 mm
Bevel angle (α)	38.3 °

Figure 23 – Model details of the orifice plate and its position for the eccentric case 99970, A = 139.1 mm, B= 25.5 mm.
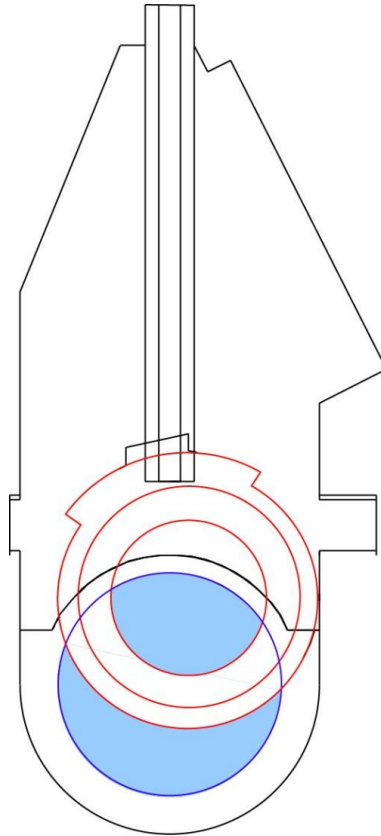
Figure 24 – Cross sectional view of the orifice plate and its position for the eccentric
case 99970, A = 139.1 mm, B= 25.5 mm.

7.2   Gas flow properties and conditions for cases 99970

Table 10 below shows the flow rates and properties used in the simulations for each case
considered. For a typical case the actual volume flow rate, density and viscosity are used
to calculate the velocity boundary conditions in the pipe flow calculation. The resulting
outlet flow profile from the pipe flow calculation is then used in the main calculation as inlet
boundary conditions.

7.3   CFD Model details

The model is based on CFD details described in Section 4. For each simulation a fully
developed flow profile obtained from the pipe flow calculation is used for the inlet boundary
condition. Fluid flow properties are set as Methane gas and given density and viscosity
values are used for properties. The standard $k - \varepsilon$ turbulence model with standard model
constants is used in the calculations. In the solution process the second order upwind
discretisation scheme was used for all equations. Three grid levels are used to conduct
CFD simulations. Table 11 shows details of the grids used. A portion of the mesh of Grid 3
is shown in Figure 25. Table 10 also shows measured DP data for four cases considered in

the modelling. From the simulations, CFD predicted DP is obtained and compared against the measured values.

Table 10 Test conditions for cases 99970

99970 Test number		Test 3	Test 7	Test 8	Test 10
Case identification		970-3	970-7	970-8	970-10
DP (measured)	mbar	140.1955	127.9560	65.18545	133.6162
Density	kg/m^3	57.5855	59.9909	53.1184	53.0649
Std Volumetric Flow Rate	scm/h	182556.673	175801.886	121150.405	172026.929
Mass Flow Rate	kg/h	139976.124	135576.895	92506.608	131209.380
Actual Volumetric Flow Rate	m^3/h	2430.7522	2259.9550	1741.5158	2472.6176
Isentropic Index		1.3643	1.3702	1.3563	1.3567
Dynamic Viscosity	Pa.s	0.0000124	0.0000125	0.0000123	0.0000123

Table 11 – Details of the grids used for 99970 simulation series

Grid 1	Grid 2	Grid 3
1253166 elements	2173194 elements	3007307 elements
(1.25 million grid)	(2.17 million grid)	(3.01 million grid)
Common features		
Tetrahedral elements at complex geometry areas (carrier space, orifice plate area and thermowell). Hexahedral elements at all other parts. Orifice plate area finely meshed. Boundary layer meshes at walls to maintain y+.		

7.4   Results and Discussion – Cases 99970

Table 12 shows results of the cases considered from the test series 99970. For the purpose of the discussion the cases used from this series are given a Case identification number shown in the first column. In Table 12 predicted DP from each CFD simulation (Grid 1, Grid 2 and Grid 3) is compared against measured experimental value and the error between the results as a percentage of the experimental value is shown. The uncertainty of the measurements is also shown in the table. It can be seen that except for the Case 970-8 (Test 8) all other predictions compare very well and Grid 3 errors are less than 1.5 % and more importantly calculated DP values are within the uncertainty of the measurements. For case 970-8 the coarse grid result (Grid 1) gives an error of 11.2%. Improvements can be

seen with Grid 2 and Grid 3. The result of Grid 3 is, however, 4.5% under predicted. For this case the predictions are not with the uncertainty. In general the difference between Grid 2 and Grid 3 results for all cases are less than 1.6% indicating that the overall results are not very sensitive grid density after a certain level of refinement (Grid 2 results are very similar to Grid 3 results). It could be said that CFD predictions of Grid 3 show reasonably good results and more importantly predict DP values close to experimental measurements.

Using results of the case 970-3, general flow features could be illustrated through some vector and contour plots. Figure 26 shows the velocity vectors close to the walls of the carrier geometry and the orifice plate for the case 970-3. It can be seen that vertical vectors leading to the carrier space indicate how the flow leaks into the carrier space from the pipe. This results in a recirculating flow region inside the carrier space. Figure 27 shows a cross sectional view of velocity vectors at an x-y mid-plane through the geometry. The figure shows how the central part of the pipe flow is now obstructed by the orifice plate skirt due to the misalignment and compared to Figure 21 (correct orifice plate flow) the flow is completely different here. Due to the obstruction, a recirculation zone is established behind the orifice plate skirt. Two concentrated flow regions are established at the top and bottom parts of the pipe. Figure 28 shows the vectors across a mid x-z plane. The flow clearly does not resemble an orifice plate flow situation. This is the plane where the pressure data is taken for DP. There is a jet like flow stream where there is space between the orifice plate skirt and the pipe wall. Figures 29 and 30 show static pressure contours on mid x-y and mid x-z planes. It should be noted that pressure tappings are located on the mid x-z plane of the geometry. Pressure contours shows that the pressure around the pressure tapping locations is negative. Figure 31 shows the pressure distribution along a line close to the wall where the pressure tappings are located. The pressure differential in this case results in from the difference between two negative pressures (relative static pressure) values. In correct orifice flows the pressure differential across the plate results in from the difference between a positive and a negative pressure values (see Figure 20 for example).

The leakage of flow into the carrier space and its effect on pressure distribution can be further illustrated by visualising velocity and pressure distribution just before and just after the orifice plate faces. Shown in Figures 32 and 33 are velocity vector plots at y-z planes just before the upstream side of the orifice plate face and just after the downstream face of the orifice plate respectively. It can be seen in Figure 32 that there is a clear stream of flow into the carrier space where the orifice plate is not sealed and the velocities of this stream are high at the sides as there is less space between the plate and the carrier wall. At the back of the orifice plate (Figure 33) the flow comes back into the pipe, again the

velocity magnitudes are high where there is less space (sides). Figures 34 and 35 show pressure contours at y-z planes just before and just after the orifice plate faces. It is clear that flow leakage results in a constant high pressure region inside the carrier geometry. In Figure 34 the area where the front of orifice plate is inside the pipe shows a high pressure region (red). There is a noticeable pressure drop in the flow leakage regions. Figure 34 shows the pressure at a y-z plane behind the orifice plate downstream face. A low pressure region exists behind the blockage area and a high pressure region can be seen in the carrier space.
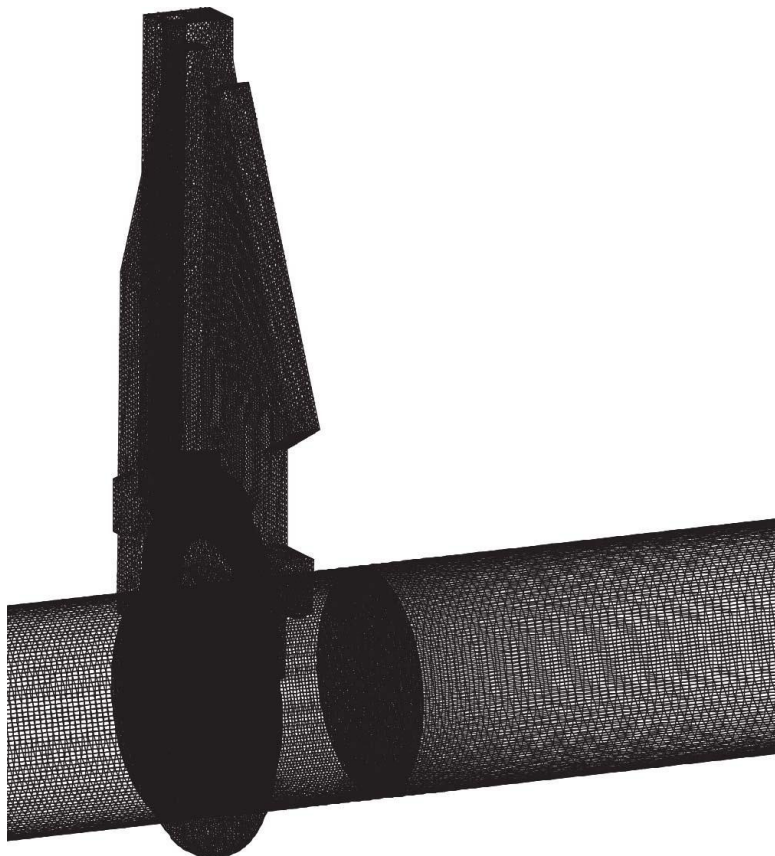
Figure 25. Mid-section of the grid used in the calculation of cases 99970

| 6.60e-03 | 4.63e+00 | 9.26e+00 | 1.39e+01 | 1.85e+01 | 2.31e+01 | 2.78e+01 | 3.09e+01 |
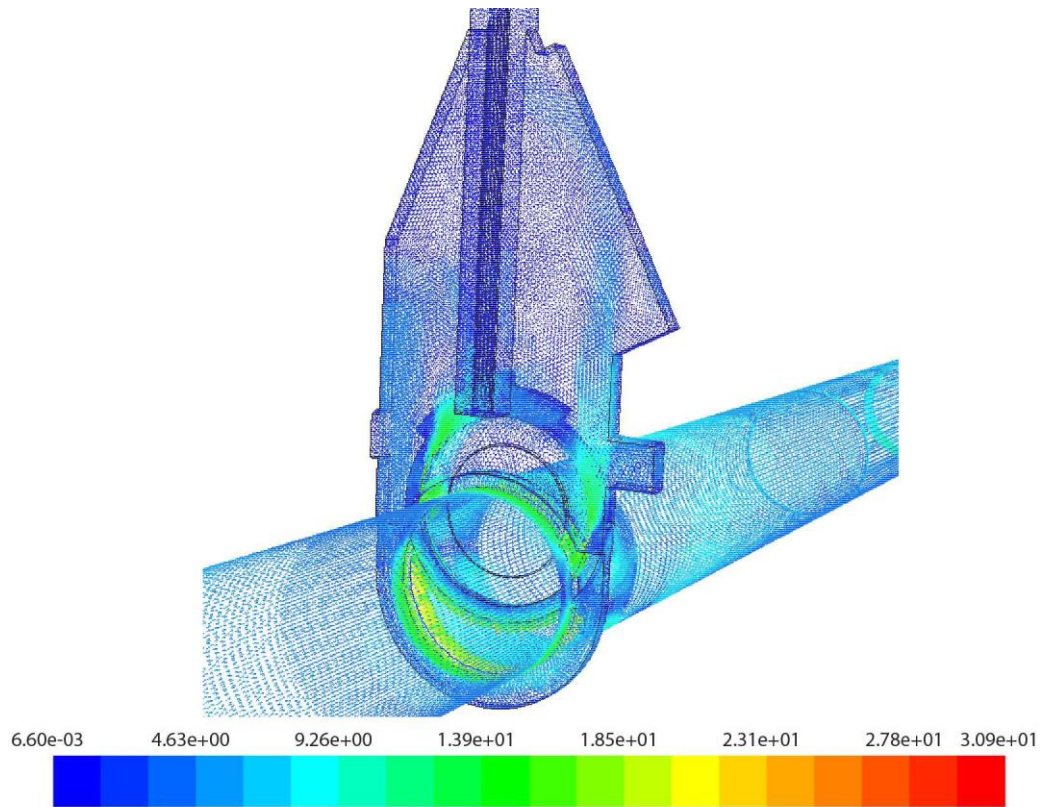
Figure 26. Velocity vector distribution close to walls of the geometry

| 0.0 | 4.6 | 9.3 | 13.9 | 18.5 | 23.1 | 27.8 | 30.9 |
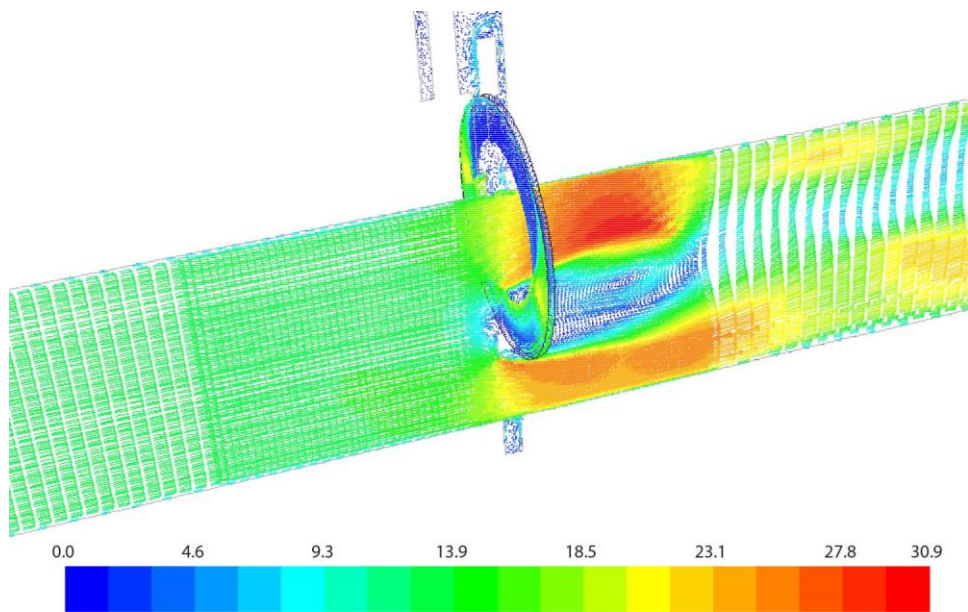
Figure 27. Velocity vector distribution on the mid x-y plane
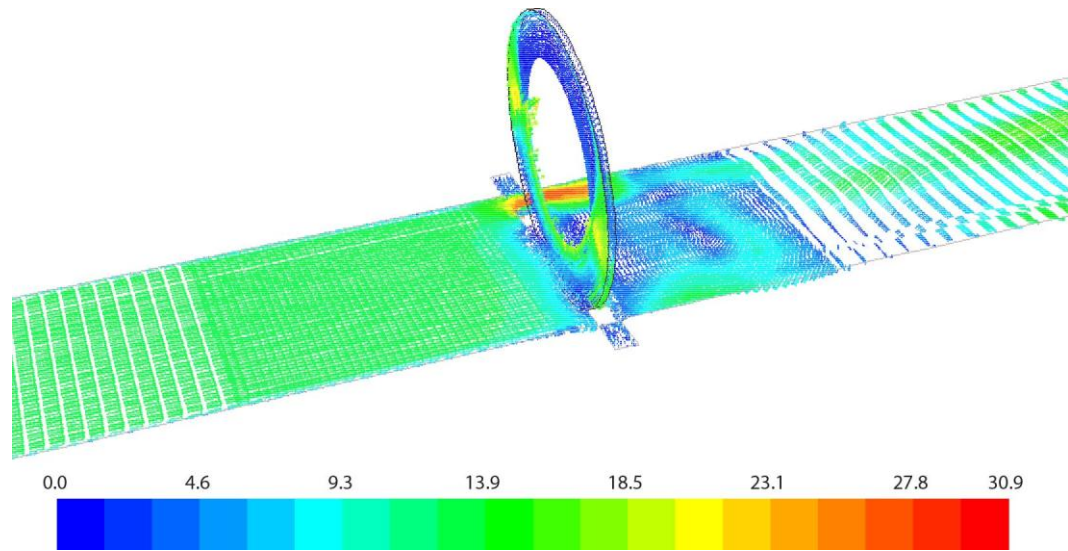
Figure 28. Velocity vector distribution on the mid x-z plane
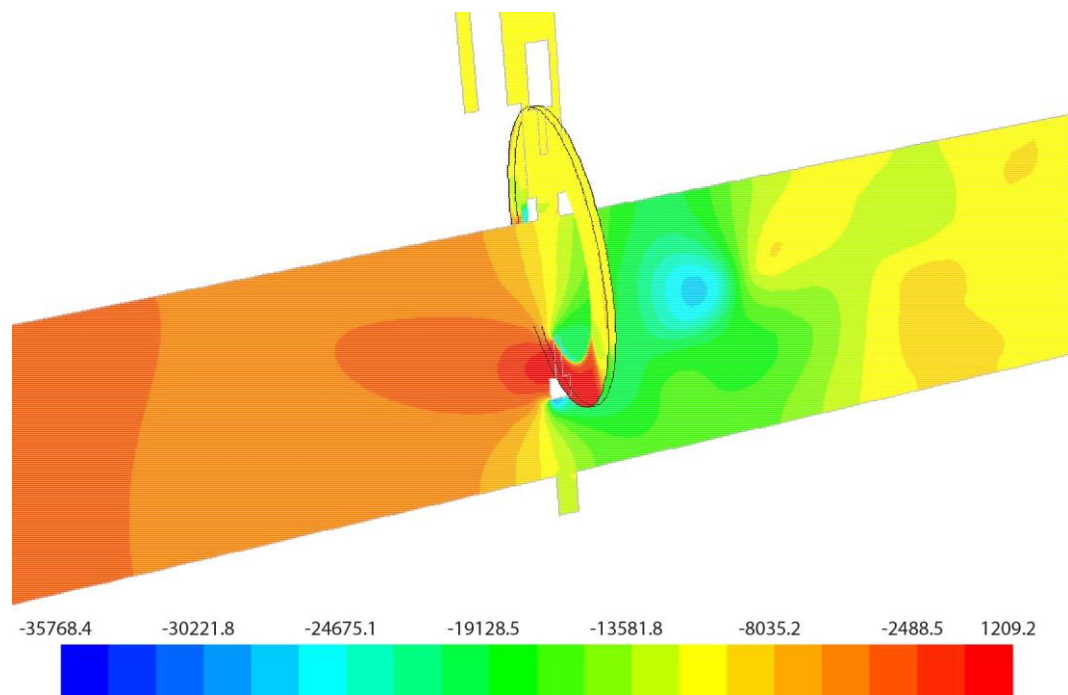
Figure 29. Static pressure distribution on the mid x-y plane
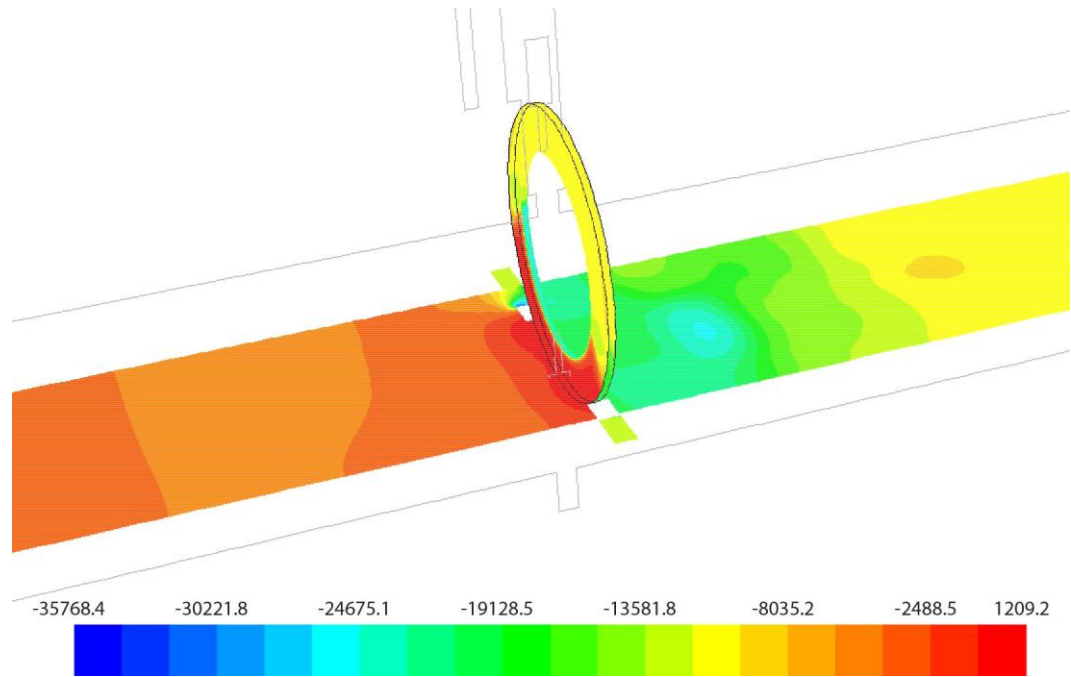
Figure 30. Static pressure distribution on the mid x-z plane
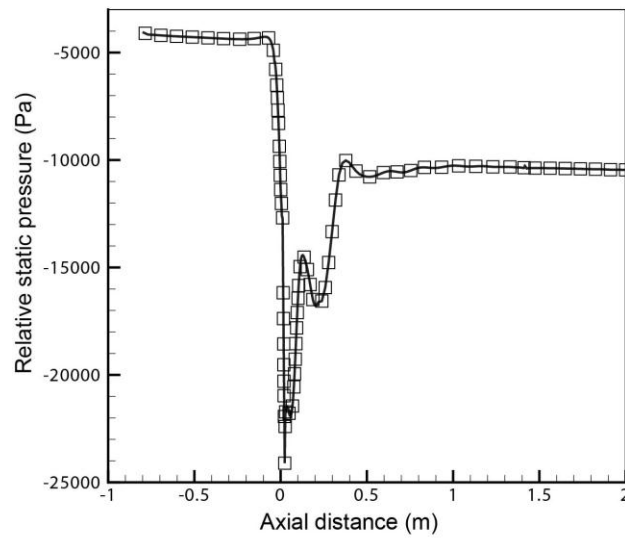
Figure 31. Case 970-1 Pressure distribution along a line near the wall at the x-z plane
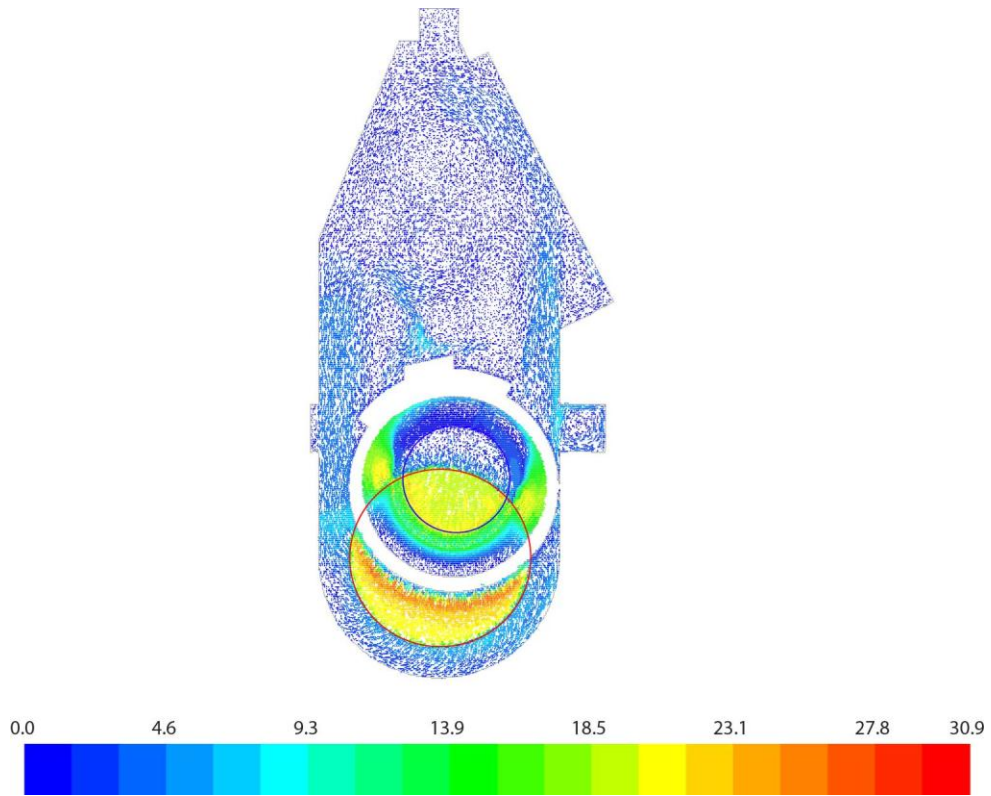
Figure 32. Velocity vector plot on a y-z plane at just before the orifice plate upstream face indicating flow leakage from the front to the carrier space.

Figure 33. Velocity vector plot on a y-z plane at just after the orifice plate downstream face indicating flow back from the carrier space to the pipe
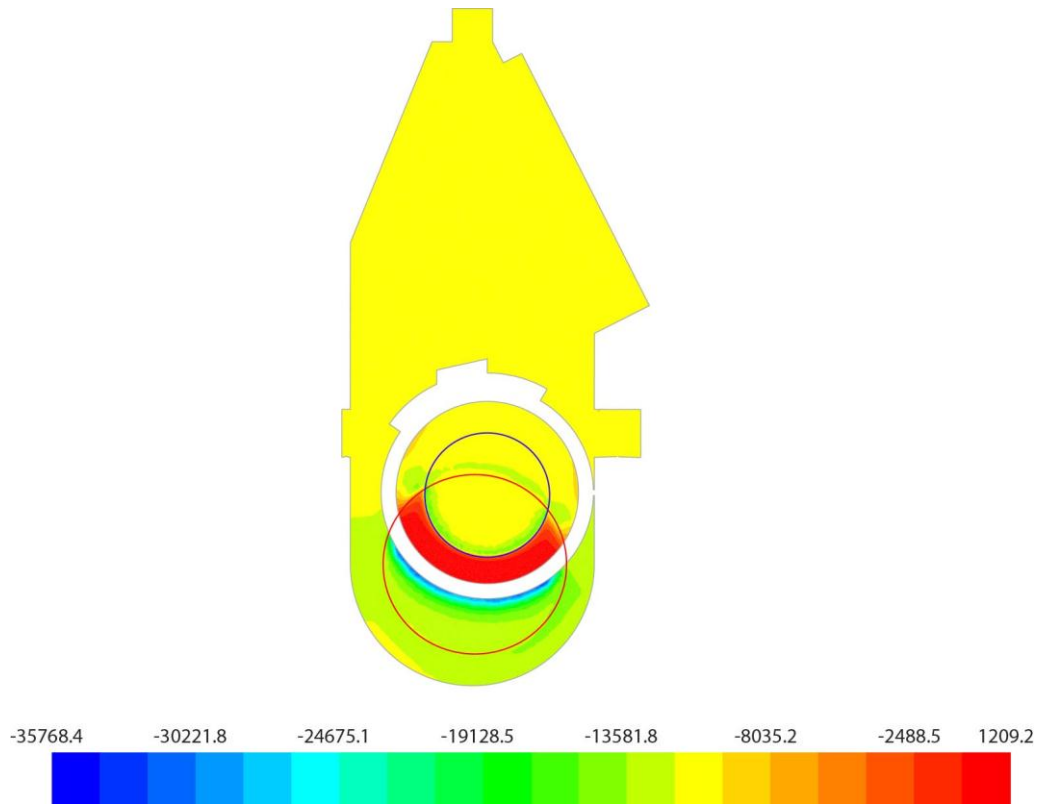
Figure 34. Static pressure contour plot on a y-z plane at just before the orifice plate upstream face.
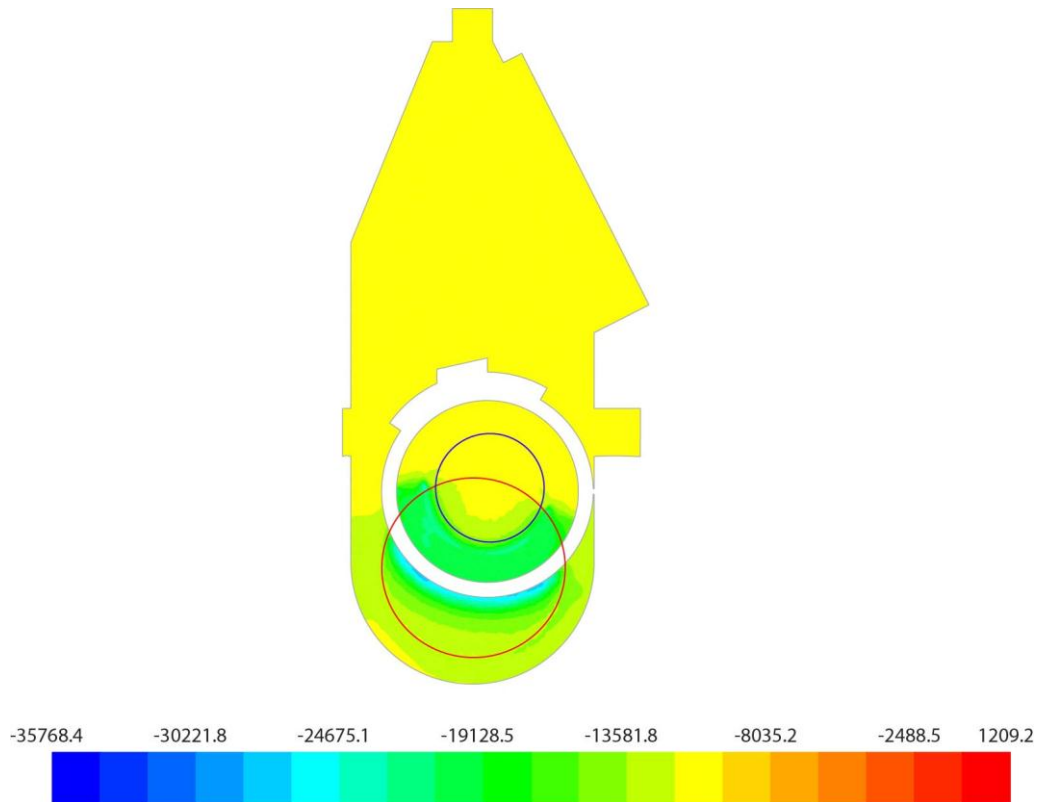
Figure 35. Static pressure contour plot on a y-z plane at just after the orifice plate downstream face.

Table 12 SUMMARY OF RESULTS FOR CASES 99970

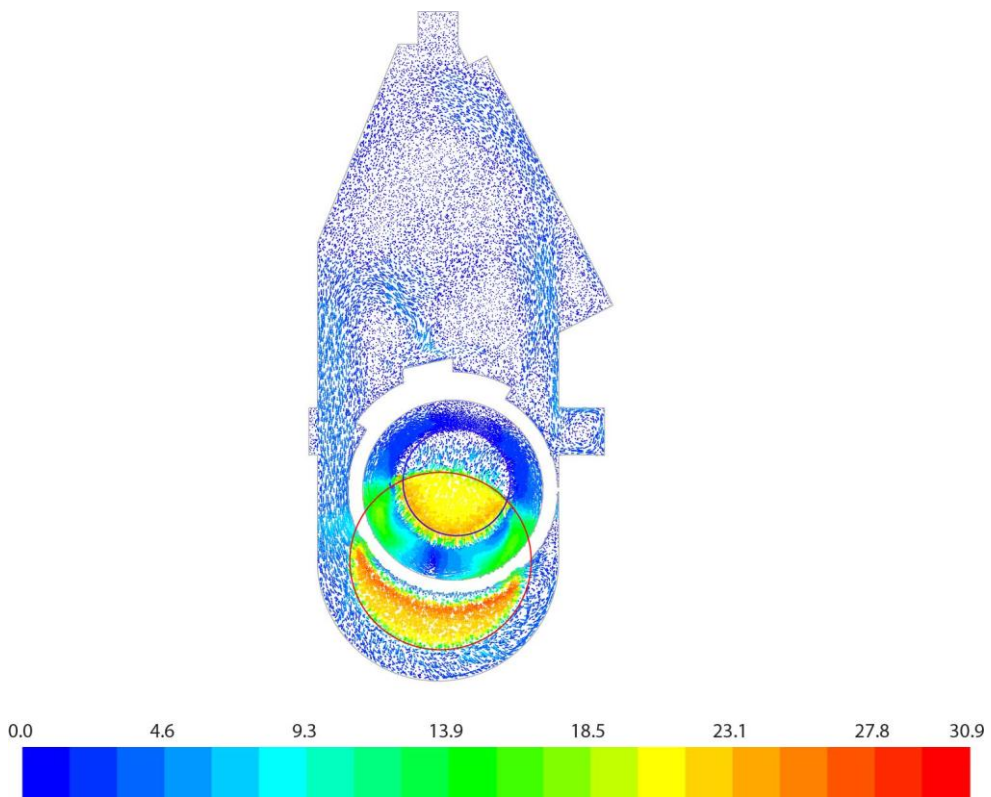| Case id	Case considered and identification details	Actual flow rate (m³/h) and (Mass flow rate, kg/h)	Density (kg/m³) and viscosity	Model variation	Predicted DP (mbar)	Measured DP (mbar)	Error %	Remarks	% Difference of error between models (1&2, 2&3)
970-3	**CASE 99970 – TEST 3** Incorrect position - Eccentric dimensions are A = 139.1, B=25.5 mm (max used touching the wall).	2430.7522 (139976.124)	57.585 1.24e-5	**Grid_1**	**137.32**	140.19	**2.0%**	Uncertainty in measurements < 2 %	**-**
				Grid_2	**142.42**		**1.5%**		**0.5%**
				Grid_3	**142.43**		**1.5%**		**0%**
970-7	**CASE 99970 – TEST 7** Incorrect position - Eccentric dimensions are A = 139.1, B=25.5 mm (max used touching the wall).	2259.955 (135576.895)	59.990 1.25e-5	**Grid_1**	**125.12**	127.96	**2.2%**	Uncertainty in measurements < 2 %	**-**
				Grid_2	**126.41**		**1.2%**		**1.0%**
				Grid_3	**126.73**		**0.9%**		**0.3%**
970-8	**CASE 99970 – TEST 8** Incorrect position - Eccentric dimensions are A = 139.1, B=25.5 mm (max used touching the wall).	1741.5158 (92506.608)	53.118 1.23e-5	**Grid_1**	**57.88**	65.19	**11.2%**	Uncertainty in measurements < 1.5 %	**-**
				Grid_2	**61.19**		**6.1%**		**5.1%**
				Grid_3	**62.23**		**4.5%**		**1.6%**

| 970-10 | **CASE 99970 – TEST 10**
Incorrect position - Eccentric dimensions are A = 139.1, B=25.5 mm (max used touching the wall). | 2472.6176
(131209.380) | 53.064
1.23e-5 | **Grid_1**

Grid_2

Grid_3 | **130.47**

132.42

132.81 | 133.61 | **2.3%**

0.8%

0.5 % | Uncertainty in measurements < 2 % | **-**

1.5%

0.3% |

8.   CFD Modelling of test Cases 99985

8.1   The geometry

The set of cases from the series of experiments conducted for the orifice plate position identified by 99985 are considered here for the simulations. For this position A and B values for winding down are A = 87.23 mm and B = 17.5 mm. Figure 36 below shows a sketch of the CFD model geometry for the case 99985. Shown in Figure 37 is a view normal to the pipe axis and it shows the degree of eccentricity and the extent of the orifice plate top circumferential part that is open to the upper chamber. The figure also shows the area under the orifice plate skirt directly open to flow. The same plate used in Cases 99970 is used here, Table 9 shows the details. Pipe lengths used in the construction of the geometry are the same as in Cases 99970.
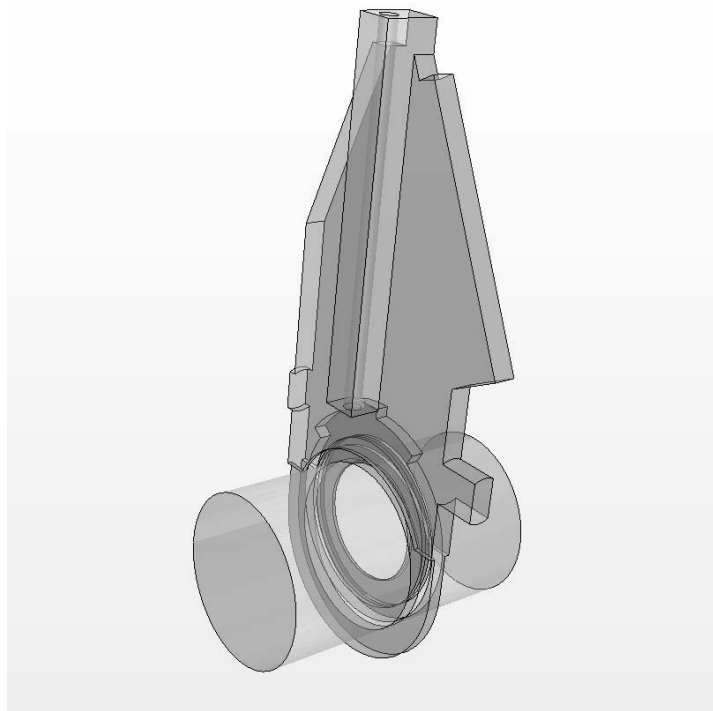
Figure 36 – Model details of the orifice plate and its position for the eccentric case 99985, A = 87.23 mm and B = 17.5 mm.
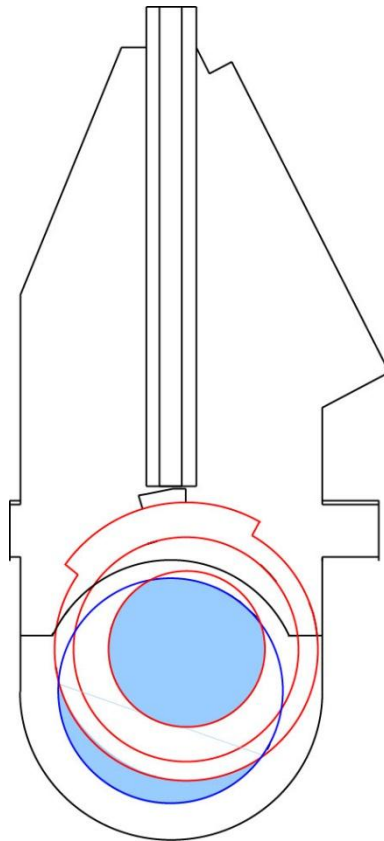
Figure 37 – Cross sectional view of the orifice plate and its position for the case 99985, A = 87.23 mm and B = 17.5 mm.

8.2   *Gas flow properties and conditions for cases 99985*

Ten test cases are considered from this test series. Table 13 shows the flow rates and properties used in the simulations for each case considered. For a typical case the actual volume flow rate, density and viscosity are used to calculate the velocity boundary conditions in pipe flow calculations. In each case the resulting outlet flow profile from the pipe flow calculation is then used in the main calculation as the inlet boundary condition.

Table 13 – Operating conditions, properties and measured DP values for cases 99985

Test number		Test 1	Test 2	Test 3	Test 4	Test 6
Case id.		Case 985-1	Case 985-2	Case 985-3	Case 985-4	Case 985-6
DP	mbar	13.784	103.136	242.939	102.495	12.062
Density	kg/m^3	56.6841	56.8914	57.64797	60.1082	60.1575
Std. Volumetric Flow Rate	scm/h	44091.1488	119001.66	180152.865	120278.43	41739.786
Mass Flow Rate	kg/h	33696.184	90950.243	138132.993	92601.981	32179.620
Actual Volumetric Flow Rate	m^3/h	594.45605	1598.6628	2396.1463	1540.5864	534.92254
Isentropic Index		1.3639	1.3644	1.3644	1.3710	1.3706
Dynamic Viscosity	Pa.s	0.0000124	0.0000124	0.0000124	0.0000125	0.0000125
Test number		Test 7	Test 8	Test 9	Test 10	Test 11
		Case 985-7	Case 985-7	Case 985-9	Case 985-10	Case 985-11
DP	mbar	208.331	112.566	14.067	217.578	15.981
Density	kg/m^3	60.0409	53.1180	53.6954	53.1106	53.3384
Std. Volumetric Flow Rate	scm/h	169280.91	120286.70	42811.8644	168178.55	45290.897
Mass Flow Rate	kg/h	130547.97	91847.11	32754.04	128274.12	34565.349
Actual Volumetric Flow Rate	m^3/h	2174.3146	1729.1119	609.9963	2415.2227	648.0378
Isentropic Index		1.3703	1.3563	1.3568	1.3568	1.3571313
Dynamic Viscosity	Pa.s	0.0000125	0.0000123	0.0000123	0.0000123	0.0000123

8.3 CFD Model details

The model is based on CFD details described in Section 4. A fully developed flow profile obtained from pipe flow calculations is used for the inlet boundary condition. Fluid flow properties are set as Methane gas and given density and viscosity values from Table 13 are used for properties. The $k - \varepsilon$ turbulence model with standard model constants is used in the calculations. In the calculation procedure the second order upwind difference scheme is used for all equations. Three grid levels are used to conduct CFD simulations. Table 14 shows details of the grids used. A portion of the mesh of Grid 3 is shown in Figure 38. Table 13 shows measured DP data for all the cases considered in

the modelling. From the simulations, CFD predicted DP is obtained and compared against the measured values.

Table 14 – Details of the grids used for 99985 simulation series

Grid 1	Grid 2	Grid 3
2445495 elements (2.45 million grid)	2909695 elements (2.91 million grid)	2967564 elements (2.97 million grid)
Common features		
Tetrahedral elements at complex geometry areas (carrier space, orifice plate area and thermowell). Hexahedral elements at all other parts. Orifice plate area finely meshed with 0.5 mm grid spacing on orifice edges. Boundary layer meshes at walls have been used to maintain y+. See Appendix B for further details on meshing and y+ limits.		

8.4   Results and Discussion – Cases 99985

Table 15 shows results of the cases considered from the test series 99985. For the purpose of the discussion the cases used from this series are given a Case identification number shown in the first column. In Table 15 predicted DP from each simulation (Grid 1, Grid 2 and Grid 3) is compared against measured experimental data and the error between the two results as a percentage of the experimental value is shown. The uncertainty of the measurements is also shown.

It can be seen that CFD calculated DP values using the two fine grids (Grid 2 and Grid 3) give results which are close to experimental measurements within respective uncertainties except for Cases 3, 7 and 10. In Cases 985-3, 7 and 10, Grid 3 results respectively show differences of 2.2%, 2.1% and 2.1% when compared with experimental values, which are 1% outside the uncertainty of the measurements. It is noted that still these are reasonably close, maximum error being 2.5% (in Case 985-10, Grid 3). Overall it could be said that the majority of CFD predicted DP values agree very well with the measurements and more importantly in many cases very close to the experimental measurements. The last column of Table 15 shows the difference between the simulations. It can be seen that in all cases the difference between results of Grid 2 and Grid 3 is very small (less than 1%) therefore CFD results of Grid 3 may be treated as mesh independent.

Using results of case 985-3 (Grid 3), which has the highest flow rate, general flow features in this misaligned orifice plate situation could be illustrated through some vector and contour plots. Figure 39 shows the velocity vectors close to the walls of the carrier geometry and the orifice plate for the case 985-3. It can be seen that vertical vectors leading to the carrier space indicate how flow from the pipe leaks into the carrier space. This results in a recirculating flow region inside the carrier space. Figure 40 shows a cross sectional view of velocity vectors at an x-y mid-plane through the geometry. The figure shows how the central part of the flow is now obstructed by the orifice plate skirt due to the misalignment and compared to Figure 21 (correct orifice plate flow) the flow situation is very different. The accelerating jet like flow is attached to the pipe wall and there is no recirculating region around the top side of the pipe here. Due to the obstruction, a recirculation zone is established behind the orifice plate skirt. Two concentrated flow regions are established at the top and bottom parts of the central plane. Figure 41 shows the vectors across a mid x-z plane. Figures 42 and 43 show static pressure contours on mid x-y and mid x-z planes. The pressure tappings are located in the mid x-z plane of the geometry. Pressure contours show that the pressure distribution around the pressure tapping locations. Relative pressure (CFD pressure) is positive on the left side of the orifice plate location and negative on the right hand side of the location (more like a correct orifice plate situation). The pressure differential (DP) in this case results in from the difference between a positive and a negative pressure value besides the plate location. However due to the misalignment of the plate the resultant values would be far from an equivalent correct orifice plate situation. Figure 44 shows the pressure distribution along a line close to the wall on the x-z plane where the pressure tappings are located. It illustrates the pressure differential in this misaligned configuration. It should be noted that that there is no wall between the high pressure and low pressure change and the misalignment provides a clear space at this plane hence middle values are seen in the graph. In a proper orifice flow the pressure change is abrupt as the two sides are separated by walls of the orifice plate.

The leakage of flow into the carrier space and its effect on pressure distribution can be further illustrated by visualising velocity and pressure distribution just before and just after the orifice plate faces. Shown in Figures 45 and 46 are velocity vector plots at y-z planes just before the orifice plate upstream face and just after the orifice plate downstream face respectively. It can be seen in Figure 45 that there is a clear stream of flow into the carrier space where the orifice plate is not sealed and the velocities of this stream are high at the sides as there is less space between the plate and the carrier wall. At the back of the orifice plate (Figure 46) the flow comes back into the pipe

geometry, again the velocity magnitudes are high where there is less space (sides). It is possible that the central jet like flow has an entrainment effect as well and the flow is entrained into the downstream side from the carrier space. Figures 47 and 48 show pressure contours at y-z planes just before and just after the orifice plate faces. It is clear that flow leakage results in a constant high pressure region inside the carrier geometry. In Figure 47 the area where the front of orifice plate is inside the pipe shows a clear high pressure region (red). There is a noticeable pressure drop in the flow leakage regions. Figure 48 shows the pressure at a y-z plane behind the orifice plate downstream face. A low pressure region exists behind the blockage area and a high pressure region can be seen in the carrier space. Similar observations could be made in all other test cases of this series.
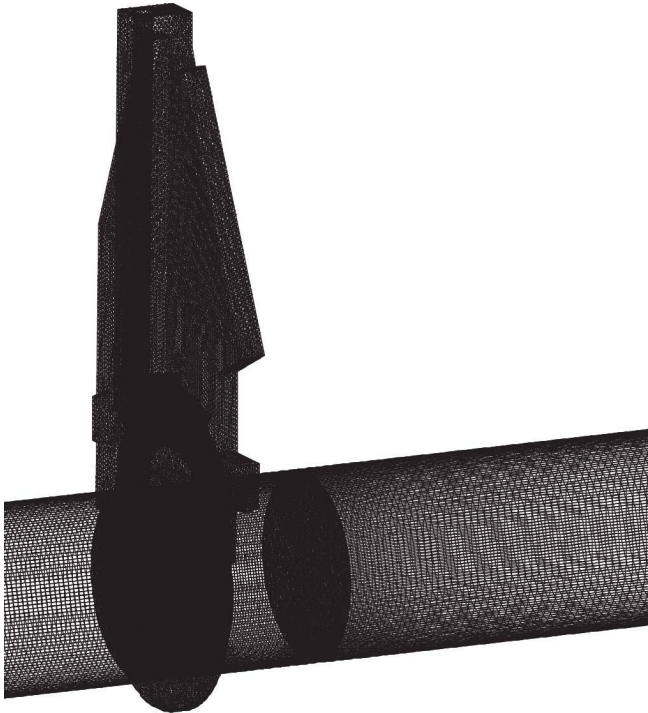
Figure 38. Mid-section of the grid used in the calculation of cases 99985
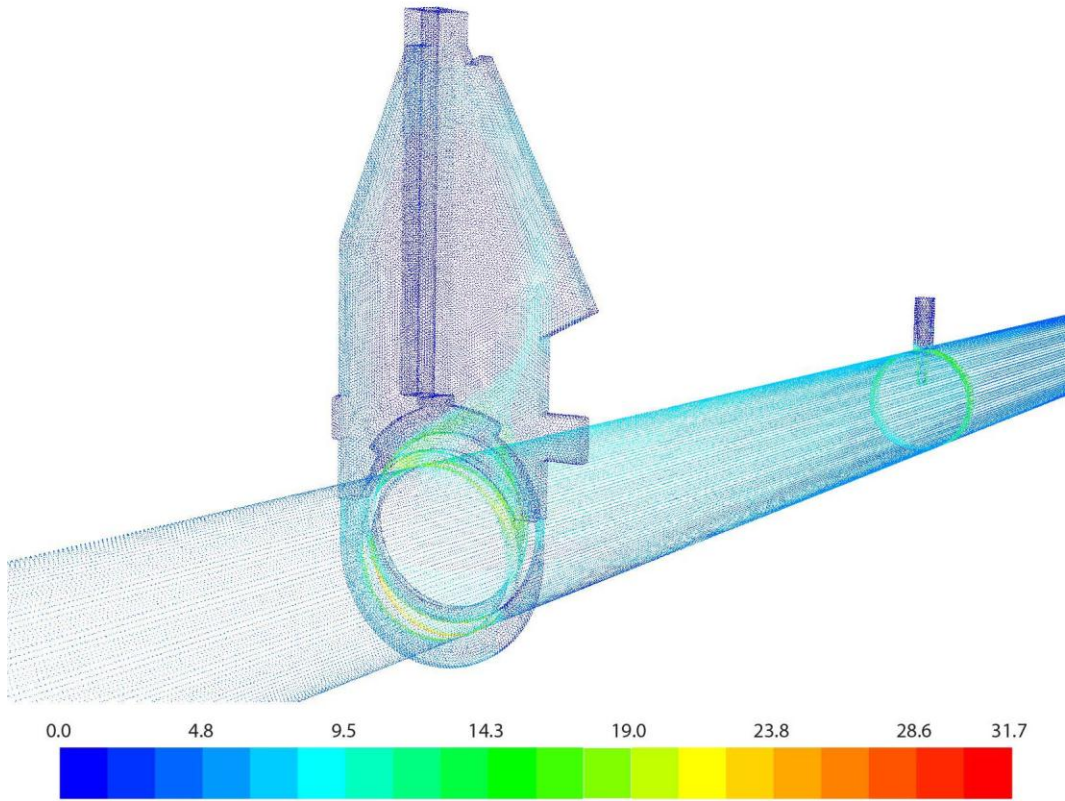
Figure 39. Velocity vector distribution close to walls of the geometry
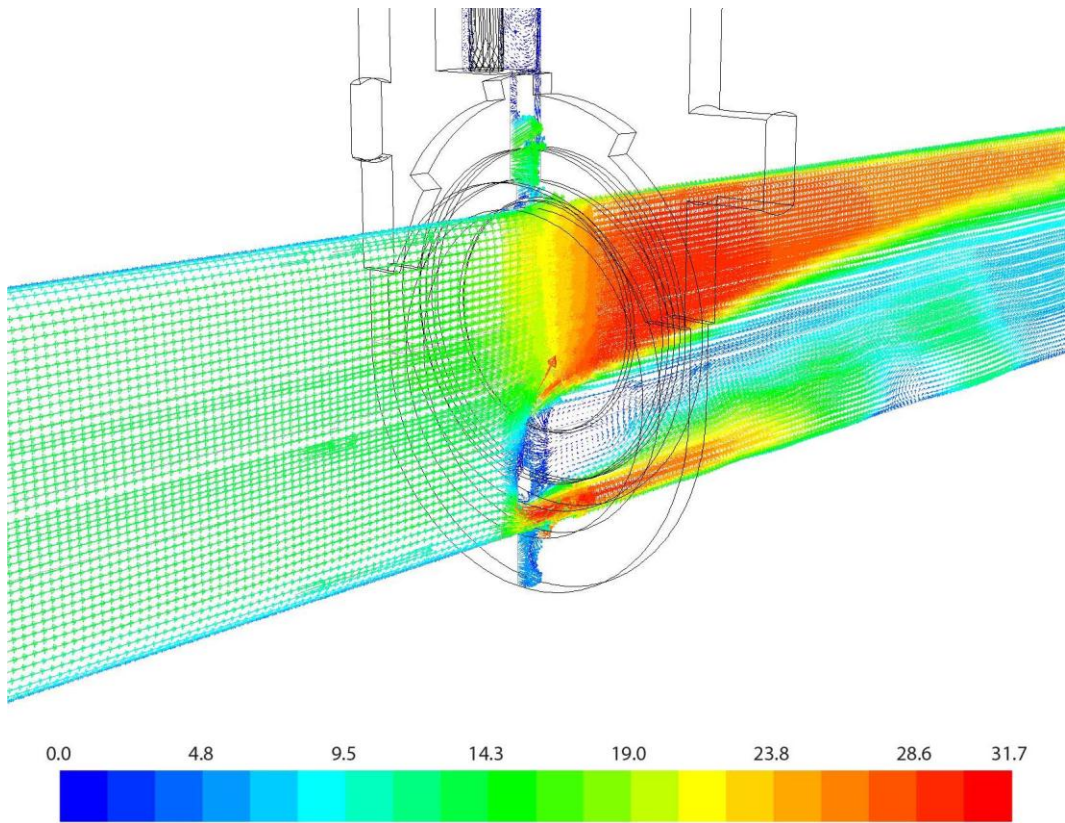
Figure 40. Velocity vector distribution on the mid x-y plane
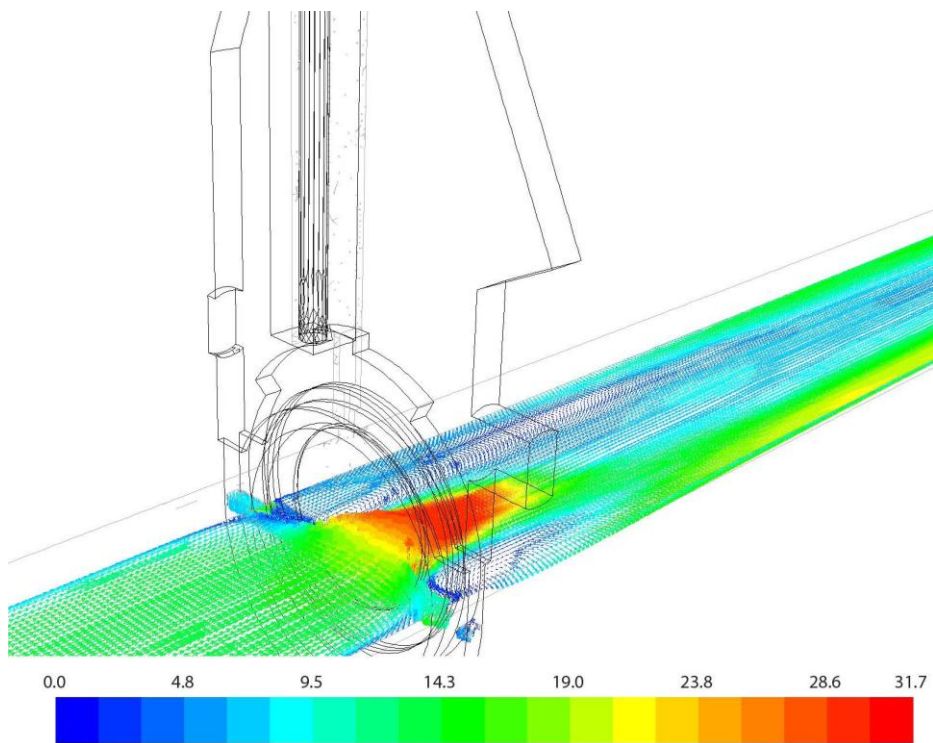
Figure 41. Velocity vector distribution on the mid x-z plane
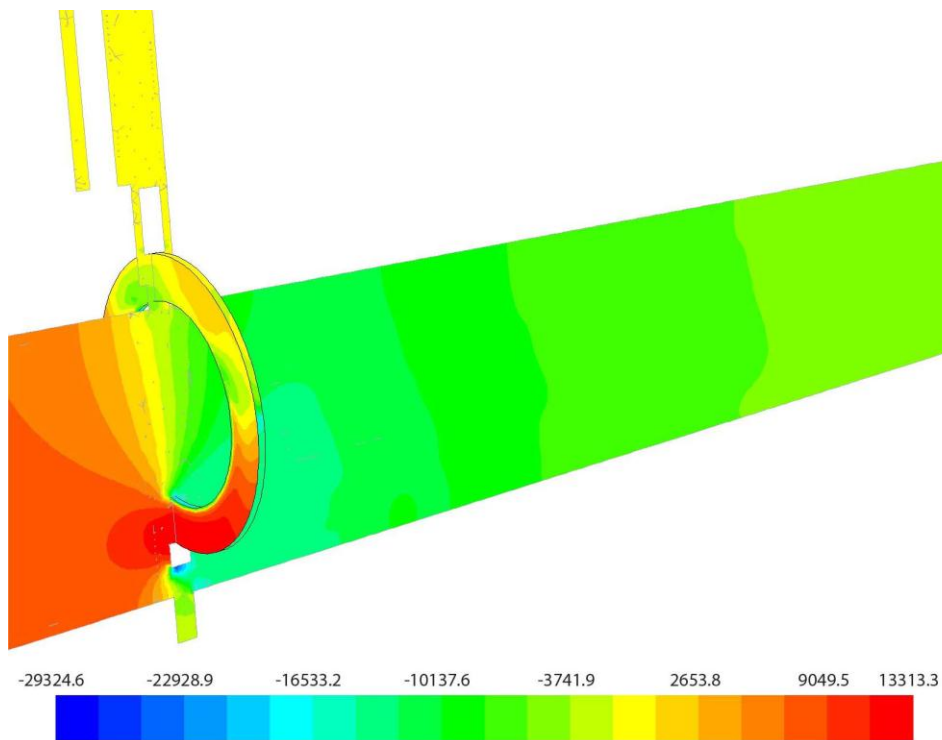
Figure 42. Pressure distribution on the mid x-y plane
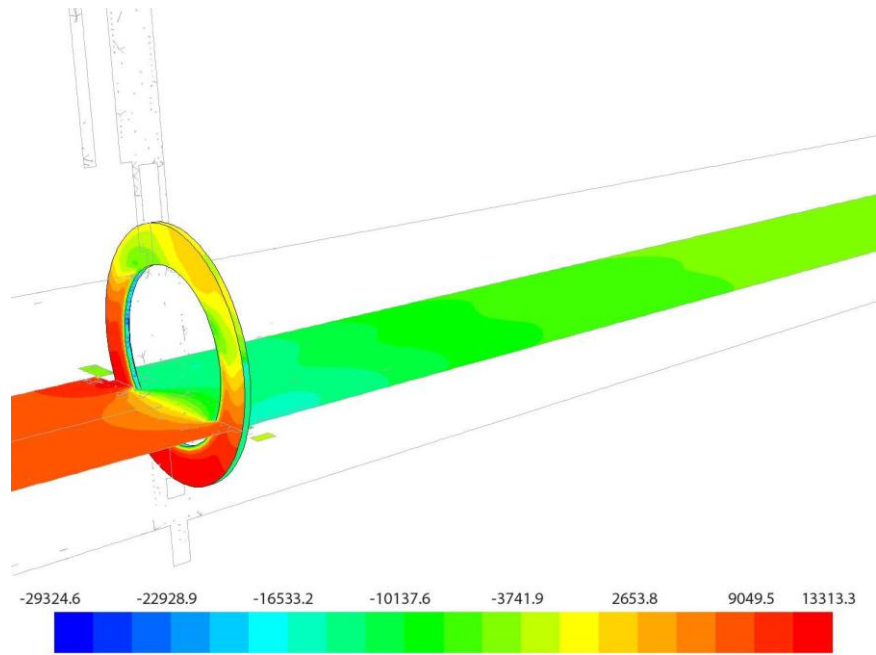
Figure 43. Pressure distribution on the mid x-z plane
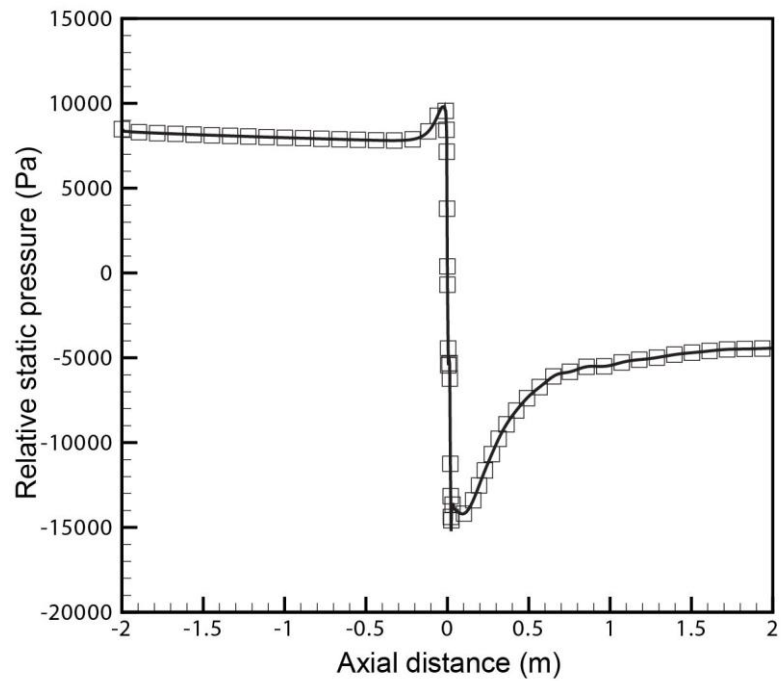
Figure 44. Case 985-3 – Pressure along a line near wall on the x-z plane.
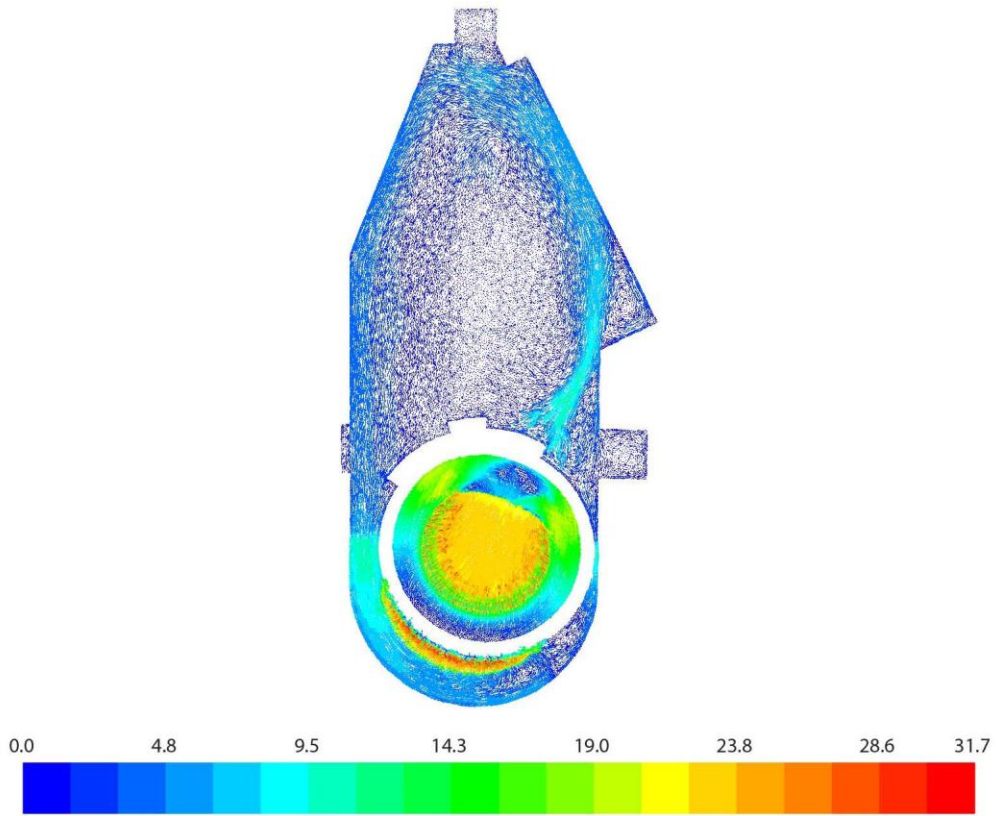
Figure 45. Velocity vector plot on a y-z plane at just before the orifice plate upstream face indicating flow leakage from the front to the carrier space.
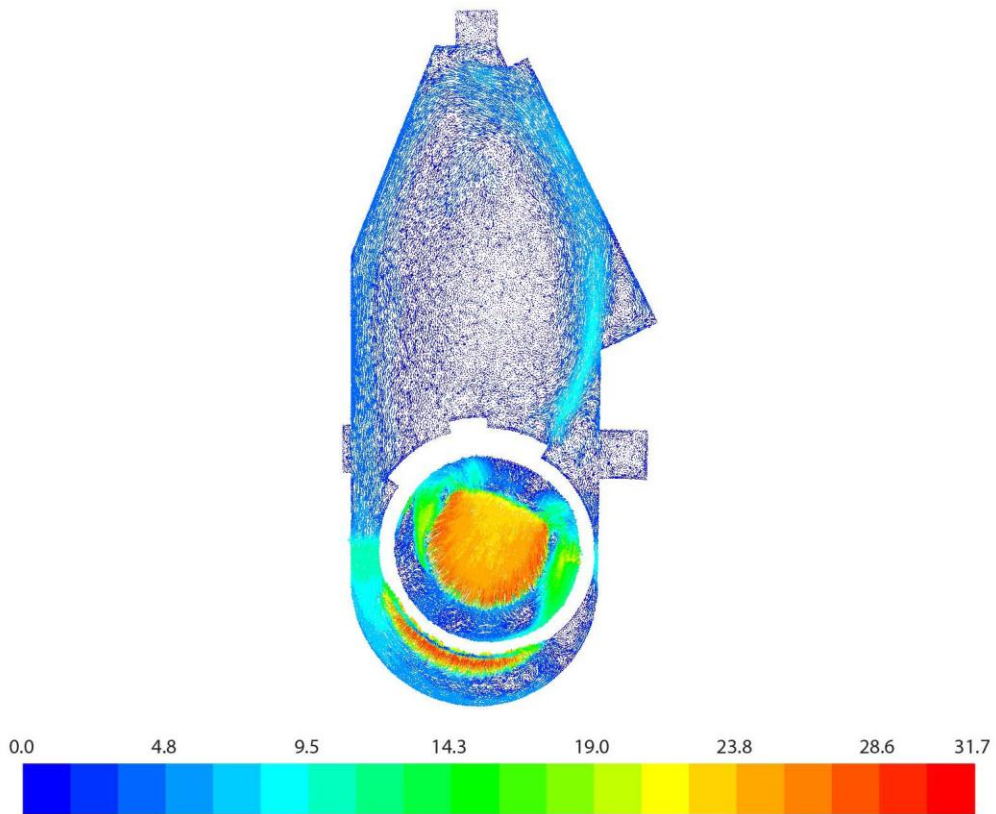
Figure 46. Velocity vector plot on a y-z plane at just after the orifice plate downstream face indicating flow back from the carrier space to the pipe
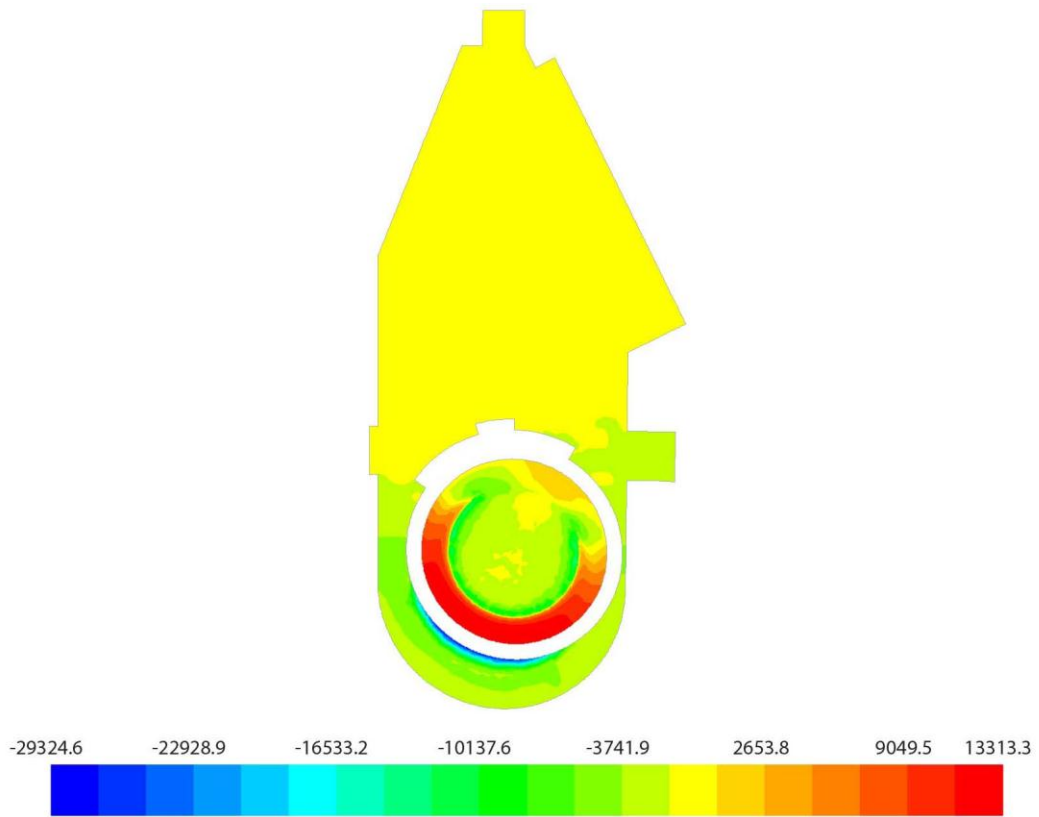
Figure 47. Static pressure contour plot on a y-z plane at just before the orifice plate upstream face.
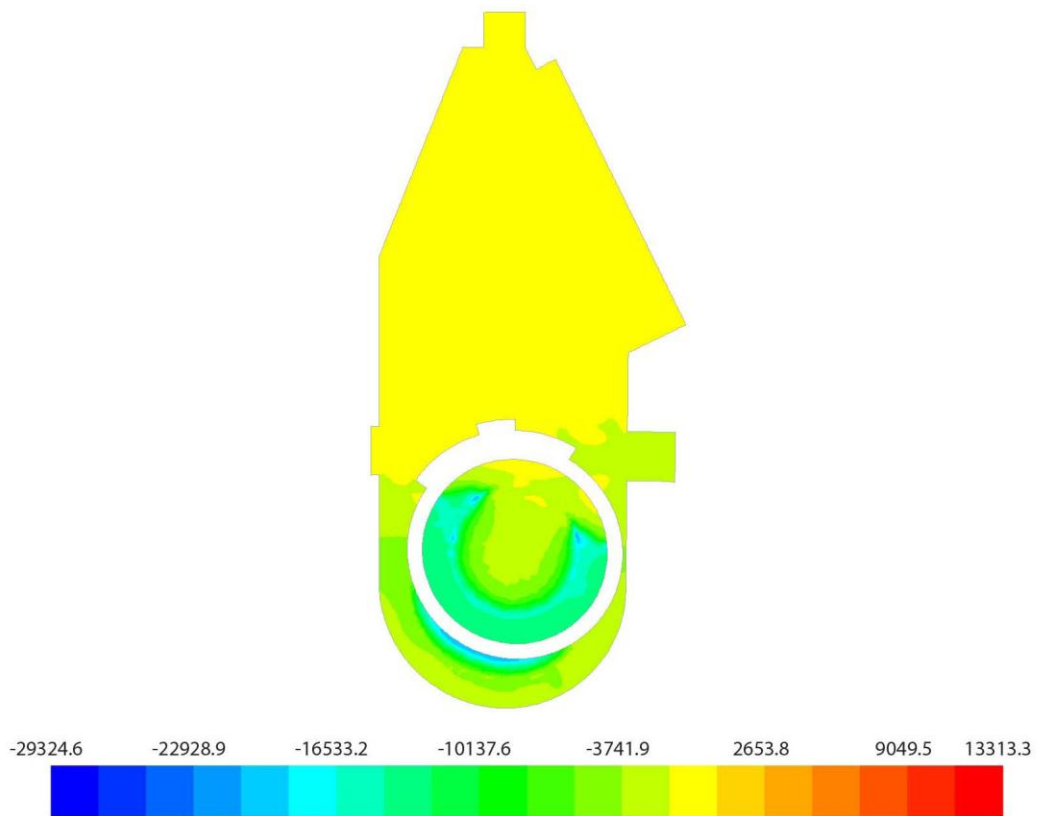
Figure 48. Static pressure contour plot on a y-z plane at just after the orifice plate downstream face.

Table 15 SUMMARY OF RESULTS FOR CASES 99985

Case id	Case considered and identification details	Actual flow rate (m³/h) and (Mass flow rate, kg/h)	Density (kg/m³) and viscosity	Model variation	Predicted DP (mbar)	Measured DP (mbar)	Error %	Remarks	% Difference of error between models (1&2, 2&3)
985-1	**CASE 99985 – TEST 1** Incorrect position - Eccentric dimensions are A = 87.23, B=17.5 mm.	594.4561 (33696.1843)	56.684 1.24e-5	**Grid_1**	**14.68**	13.784	**6.5%**	Uncertainty in measurements < 5 %	**-**
				Grid_2	**14.43**		**4.7%**		**1.8%**
				Grid_3	**14.40**		**4.4%**		**0.3%**
985-2	**CASE 99985 – TEST 2** Incorrect position - Eccentric dimensions are A = 87.23, B=17.5 mm.	1598.6628 (90950.2459)	56.892 1.24e-5	**Grid_1**	**106.25**	103.136	**3.0%**	Uncertainty in measurements < 2 %	**-**
				Grid_2	**104.71**		**1.5%**		**1.5%**
				Grid_3	**104.36**		**1.2%**		**0.3%**
985-3	**CASE 99985 – TEST 3** Incorrect position - Eccentric dimensions are A = 87.23, B=17.5 mm.	2396.1463 (138132.993)	57.647 1.24e-5	**Grid_1**	**241.54**	242.939	**0.5%**	Uncertainty in measurements < 1 %	**-**
				Grid_2	**237.72**		**2.1%**		**1.6%**
				Grid_3	**237.43**		**2.2%**		**0.1%**

985-4	**CASE 99985 – TEST 4** Incorrect position - Eccentric dimensions are A = 87.23, B=17.5 mm.	1540.5865 (92601.981)	60.108 1.25e-5	**Grid_1** **Grid_2** **Grid_3**	**104.23** **102.56** **102.43**	102.495	**1.6%** **0.0%** **0.0%**	Uncertainty in measurements < 2 %	**-** **1.6%** **0.0%**
985-6	**CASE 99985 – TEST 6** Incorrect position - Eccentric dimensions are A = 87.23, B=17.5 mm.	534.9225 (32179.62)	60.158 1.25e-5	**Grid_1** **Grid_2** **Grid_3**	**12.62** **12.31** **12.38**	12.062	**4.6%** **2.1%** **2.6%**	Uncertainty in measurements < 6 %	**-** **2.5%** **0.5%**
985-7	**CASE 99985 – TEST 7** Incorrect position - Eccentric dimensions are A = 87.23, B=17.5 mm.	2174.3146 (130547.98)	60.041 1.25e-5	**Grid_1** **Grid_2** **Grid_3**	**207.52** **203.88** **203.99**	208.331	**0.3%** **2.1%** **2.1%**	Uncertainty in measurements < 1 %	**-** **1.8%** **0.0%**
985-8	**CASE 99985 – TEST 8** Incorrect position - Eccentric dimensions are A = 87.23, B=17.5 mm.	1729.112 (91847.114)	53.118 1.23e-5	**Grid_1** **Grid_2** **Grid_3**	**116.05** **114.17** **113.87**	112.566	**3.1%** **1.4%** **1.1%**	Uncertainty in measurements < 1.5%	**-** **1.7%** **0.3%**
985-9	**CASE 99985 – TEST 9** Incorrect position - Eccentric dimensions are A = 87.23, B=17.5 mm.	609.996 (32754.048)	53.695 1.23e-5	**Grid_1** **Grid_2** **Grid_3**	**14.63** **14.39** **14.35**	14.067	**4.0%** **2.3%** **2.0%**	Uncertainty in measurements < 5 %	**-** **1.7%** **0.3%**

| 985-10 | **CASE 99985 – TEST 10** Incorrect position - Eccentric dimensions are A = 87.23, B=17.5 mm. | 2415.2228 (128274.12) | 53.111 1.23e-5 | **Grid_1** **Grid_2** **Grid_3** | **226.40** **222.93** **223.02** | 217.578 | **4.0%** **2.4%** **2.5%** | Uncertainty in measurements < 1 % | **-** **1.6%** **0.1%** |
| 985-11 | **CASE 99985 – TEST 11** Incorrect position - Eccentric dimensions are A = 87.23, B=17.5 mm. | 648.0378 (34565.349) | 53.338 1.23e-5 | **Grid_1** **Grid_2** **Grid_3** | **16.40** **16.12** **16.08** | 15.981 | **2.6%** **0.8%** **0.6%** | Uncertainty in measurements < 4.5 % | **-** **1.8%** **0.2%** |

9.   CFD Modelling of test Cases 99950

9.1   The geometry

The set of cases from the series of experiments conducted for the orifice plate position identified by 99950 are considered here for the simulations. For this position A and B values for winding down are A = 210.5 mm and B = 22.5 mm. Figure 49 below shows a sketch of the CFD model geometry for the case 99950. Shown in Figure 50 is a view normal to the pipe axis and it shows the degree of eccentricity and the extent of the orifice plate movement into the upper chamber. The figure also shows the area of the pipe at the orifice plate location directly open to flow. It can be seen that much of the pipe in this case is directly open to flow and only a fraction is obstructed by the skirt of the orifice plate. The same plate used in Cases 99970 and 99985 is used here. Table 9 shows the details. Pipe lengths used in the construction of the geometry are the same as in previous cases.
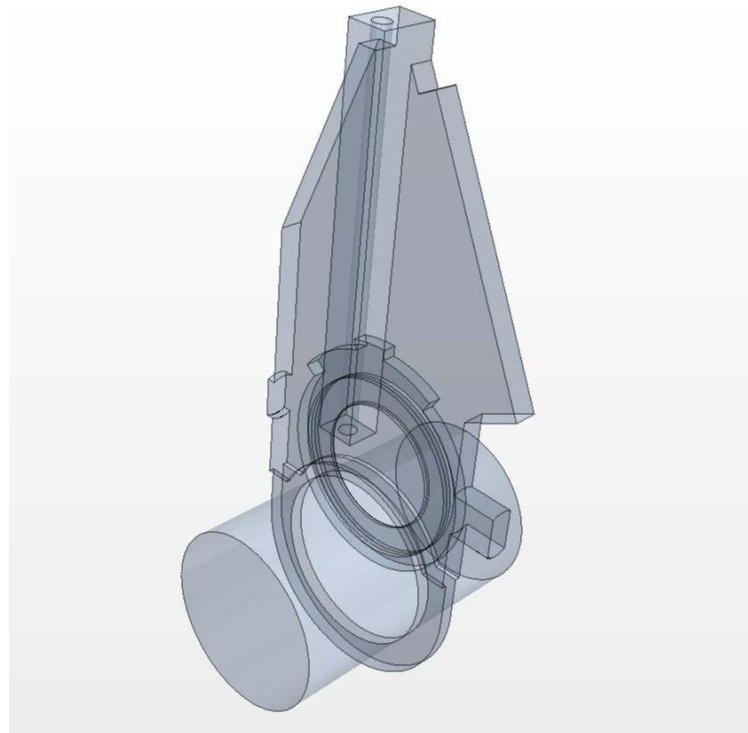
Figure 49 – Model details of the orifice plate and its position for the eccentric case 99950, A = 210.5 mm and B = 22.5 mm.
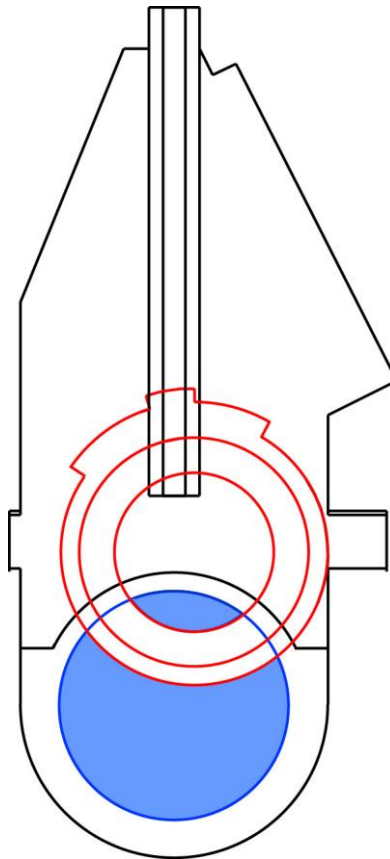
Figure 50 – Cross sectional view of the orifice plate and its position for the case 99985, A = 210.5 mm and B = 22.5 mm.

9.2   Gas flow properties and conditions for cases 99950

Ten test cases are considered from this test series. Table 16 shows the flow rates and properties used in the simulations for each case considered. For a typical case the actual volumetric flow rate, density and viscosity are used to calculate the velocity boundary conditions in the pipe flow calculations. The resulting outlet flow profile from the pipe flow calculation is then used in the main calculation as inlet boundary conditions.

Table 16 Operating conditions and properties for cases 99950

Test number		Test 1	Test 2	Test 3	Test 4	Test 6
Case id.		Case 950-1	Case 950-2	Case 950-3	Case 950-4	Case 950-6
DP	mbar	1.39	16.07	37.28	14.60	1.85
Density	kg/m^3	56.6841	56.8211	57.5534	60.1162	60.1575
Std Volumetric Flow Rate	scm/h	43656.82	120418.3	184639.97	122149.94	42236.20
Mass Flow Rate	kg/h	33364.258	92032.97	141573.50	94042.855	32562.336
Actual Volumetric Flow Rate	m^3/h	588.6003	1619.694	2459.8613	1564.3494	541.2844
Isentropic Index		1.3638	1.3642	1.3642	1.3710	1.3706
Dynamic Viscosity	Pa.s	0.0000124	0.0000124	0.0000124	0.0000125	0.0000125
		Test 7	Test 8	Test 9	Test 10	Test 11
Case id.		Case 950-7	Case 950-8	Case 950-9	Case 950-10	Case 950-11
DP	mbar	33.43	17.42	2.83	34.96	3.07
Density	kg/m^3	59.9844	53.1410	53.6954	53.0649	53.3384
Std Volumetric Flow Rate	scm/h	177719.81	121687.97	42727.96	174409.2	44297.21
Mass Flow Rate	kg/h	137055.98	92917.08	32689.86	133026.4	33806.9
Actual Volumetric Flow Rate	m^3/h	2284.8572	1748.498	608.8009	2506.863	633.819
Isentropic Index		1.3701	1.3563	1.3568	1.3567	1.3571
Dynamic Viscosity	Pa.s	0.0000125	0.0000123	0.0000123	0.0000123	0.0000123

9.3 CFD Model details

The model is based on CFD details described in Section 4. A fully developed flow profile obtained from the pipe flow calculations is used for the inlet boundary condition. Fluid flow properties are set as Methane gas and given density and viscosity values are used for properties. The standard $k - \varepsilon$ turbulence model with standard model constants is used in the calculations. In the calculation procedure the second order upwind

difference scheme is used for all equations. Three grid levels are used to conduct CFD simulations. Table 17 shows details of the grids used. A portion of the mesh of Grid 3 is shown in Figure 51. Table 16 shows measured DP data for all the cases considered in the modelling. From the simulations, CFD predicted DP is obtained and compared against the measured values.

Table 17 – Details of the grids used for 99950 simulation series

Grid 1	Grid 2	Grid 3
2131679 elements (2.13 million grid)	2647723 elements (2.65 million grid)	3032103 elements (3.03 million grid)
Common features		
Tetrahedral elements at complex geometry areas (carrier space, orifice plate area and thermowell). Hexahedral elements at all other parts. Orifice plate area finely meshed with 0.5 mm grid spacing on orifice edges. Boundary layer meshes at walls have been used to maintain y+. See Appendix B for further details on meshing and y+ limits.		

9.4 Results and Discussion – Cases 99950

Table 18 shows results of the cases considered from the test series 99950. As before the cases used from this series are given a case identification number shown in the first column. In Table 18, for each case, the predicted DP is compared against measured experimental data and the error between the two results as a percentage of the experimental value is shown. The uncertainty of the measurements is also shown in the table. From Figure 50 it is clear that the geometry in this situation is such that the orifice plate position has moved very far into the upper chamber and the main flow is disturbed by a small portion of the orifice plate. Therefore the main flow encounters relatively small disturbance due the presence of a part of the orifice plate and its skirt. The resulting pressure differential due to this disturbance is therefore very small compared to previous situations. When the flow rate is low the expected pressure differential is also very low. It can be seen from Table 16 that low flow rate cases show small DP values in the tests. The success of the CFD predictions in this test series depends on the flow rate. From the CFD results comparison shown in Table 18, it can be seen that Case 950-1 (test 1) has the lowest flow rate and the difference between the predicted and measured DP is as large as 43.1%. The other cases where CFD results are far from the experimental values are case 950-9 and Case 950-11. It is interesting to note that these three test cases operate around a Reynolds number of 3.7 x 10^6. It is quite

possible that flow conditions in these cases may be different to other cases and model options used, particularly turbulence models used may not be capable of producing successful predictions. Given that a large portion of the pipe flow is now open to the carrier chamber, the flow situation in general is complex, various stagnant and recirculation regions may be present in the chamber area. The discrepancies may be attributed to errors arising from turbulence modelling. The flow regimes found under very low flow rates may be mixed (laminar, turbulent and transition) and transient (vortex shedding) at various regions of the geometry. Under these conditions standard steady state models based on simple turbulence modelling options may not be capable of producing successful CFD predictions. The rest of the results, although not all of them are within uncertainty of the measurements, are reasonably close to measured values and more importantly reproduce experimentally observed trends. As it can be seen in Table 18, difference between results of Grid 2 and Grid 3 is very small (less than 1%) therefore CFD results of Grid 3 may be treated as mesh independent.

Using results of case 950-3, which has the highest flow rate, general flow features in this situation could be illustrated through some vector and contour plots. Figure 52 shows the velocity vectors close to the walls of the carrier geometry and the orifice plate for the case 950-3. It can be seen that vertical vectors leading to the carrier space indicate how flow from the pipe leaks into the carrier space. This results in a recirculating flow region inside the carrier space. Figure 53 shows a cross sectional view of velocity vectors at an x-y mid-plane through the geometry. The figure shows how the central part of the flow is now obstructed by the orifice plate skirt due to the misalignment and compared to Figure 21 (correct orifice plate flow) the flow pattern is completely different here. The accelerating jet like flow is attached to the bottom pipe wall and there is no recirculating region around the bottom side of the pipe wall. Due to the obstruction, a recirculation zone is established behind the orifice plate skirt, still there is jet like attached flow along the top wall of the pipe at this mid plane. Figure 54 shows the vectors across a mid x-z plane which shows a flow pattern more attached to the pipe walls with a small slower flow region in the middle of the plane. The flow features do not resemble any orifice flow situation at all. Figures 55 and 56 show static pressure contours on mid x-y and mid x-z planes. The pressure tappings are located in the mid x-z plane of the geometry. Pressure contours show the pressure distribution around the pressure tapping locations. Relative pressure (CFD pressure) is positive on the left side of the orifice plate location and negative on the right hand side of the location (more like a correct orifice plate situation). The pressure differential (DP) in this

case results from the difference between a positive and a negative pressure value beside the plate location. Figure 57 shows the pressure distribution along a line close to the wall on the x-z plane where the pressure tappings are located. It illustrates the pressure differential in this misaligned configuration. It should be noted that that there is no wall between the high pressure and low pressure change and the misalignment provides a clear space at this plane hence middle values are seen in the graph. Small pressure changes due to edge effects of the cavity are also seen in this pressure curve.

The leakage of flow into the carrier space and its effect on pressure distribution can be further illustrated by visualising velocity and pressure distribution just before and just after the orifice plate faces. Shown in Figures 58 and 59 are velocity vector plots at y-z planes just before the orifice plate upstream face and just after the orifice plate downstream face respectively. It can be seen in Figure 58 that there is a clear stream of flow into the carrier space where the orifice plate is not sealed and the velocities of this stream are high at the sides as there is less space between the plate and the carrier wall. At the back of the orifice plate (Figure 59) the flow comes back into the pipe geometry, again the velocity magnitudes are high where there is less space (sides). It is possible that the jet like flow through the orifice opening has an entrainment effect as well and the flow is entrained into the downstream side from the carrier space. Figures 60 and 61 show pressure contours at y-z planes just before and just after the orifice plate faces. It is clear that flow leakage results in a high pressure region inside the carrier geometry. In Figure 60 the area where the front of the orifice plate is inside the pipe shows a clear high pressure region (red). There is a noticeable pressure drop in the flow leakage regions. Figure 61 shows the pressure at a y-z plane behind the orifice plate downstream face. A low pressure region exists behind the blockage area and a high pressure region can be seen in the carrier space. Similar observations could be made in all other test cases of this series.
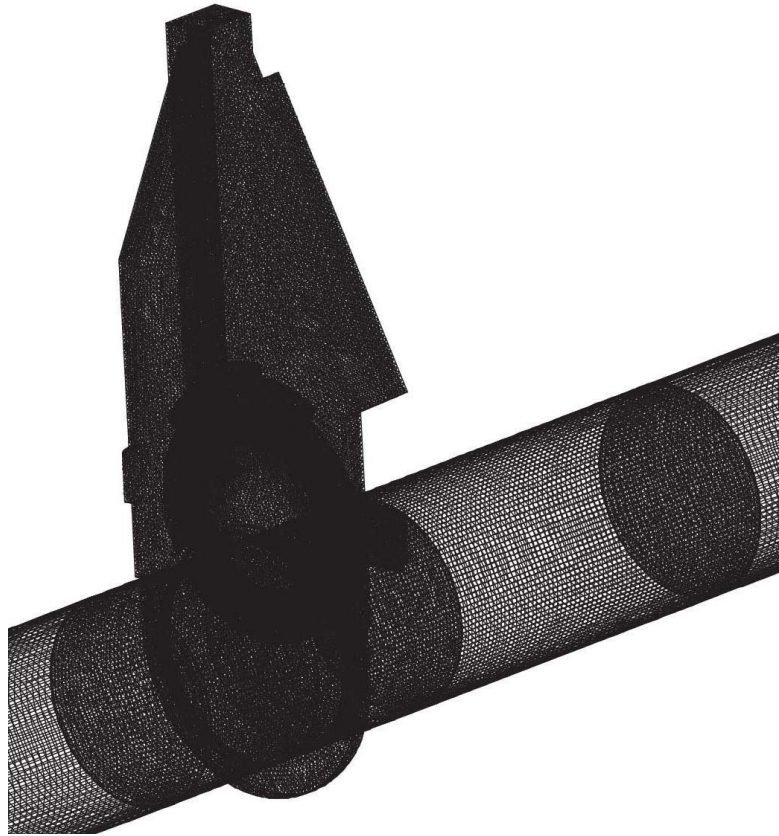
Figure 51. Mid-section of the grid used in the calculation of cases 99950

| 0.0 | 3.6 | 7.1 | 10.7 | 14.2 | 17.8 | 21.3 | 23.7 |
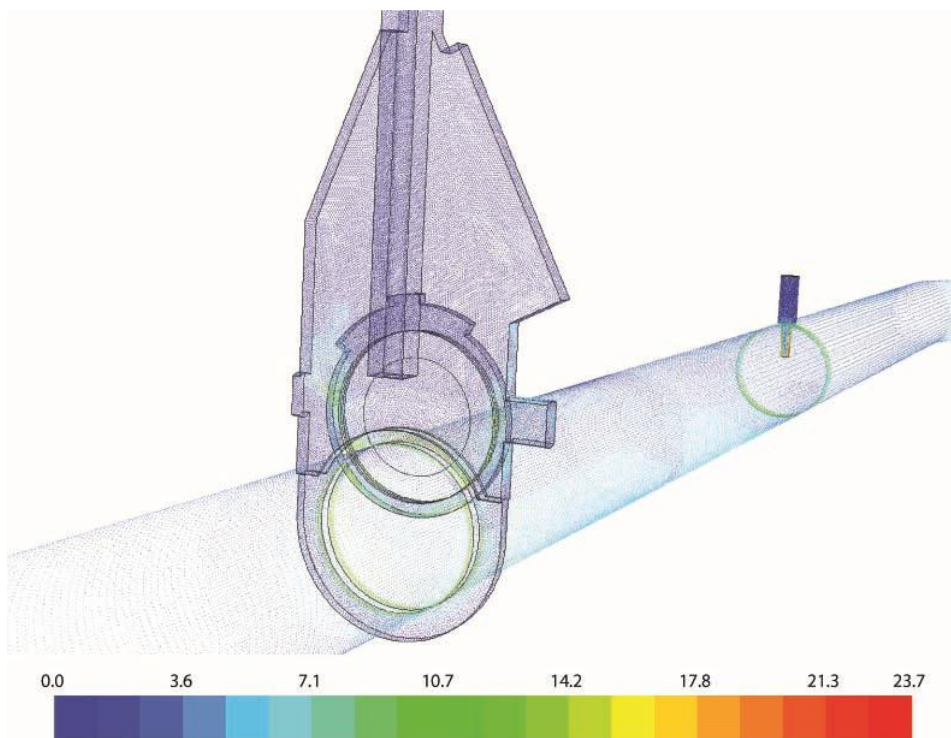
Figure 52. Velocity vector distribution close to walls of the geometry
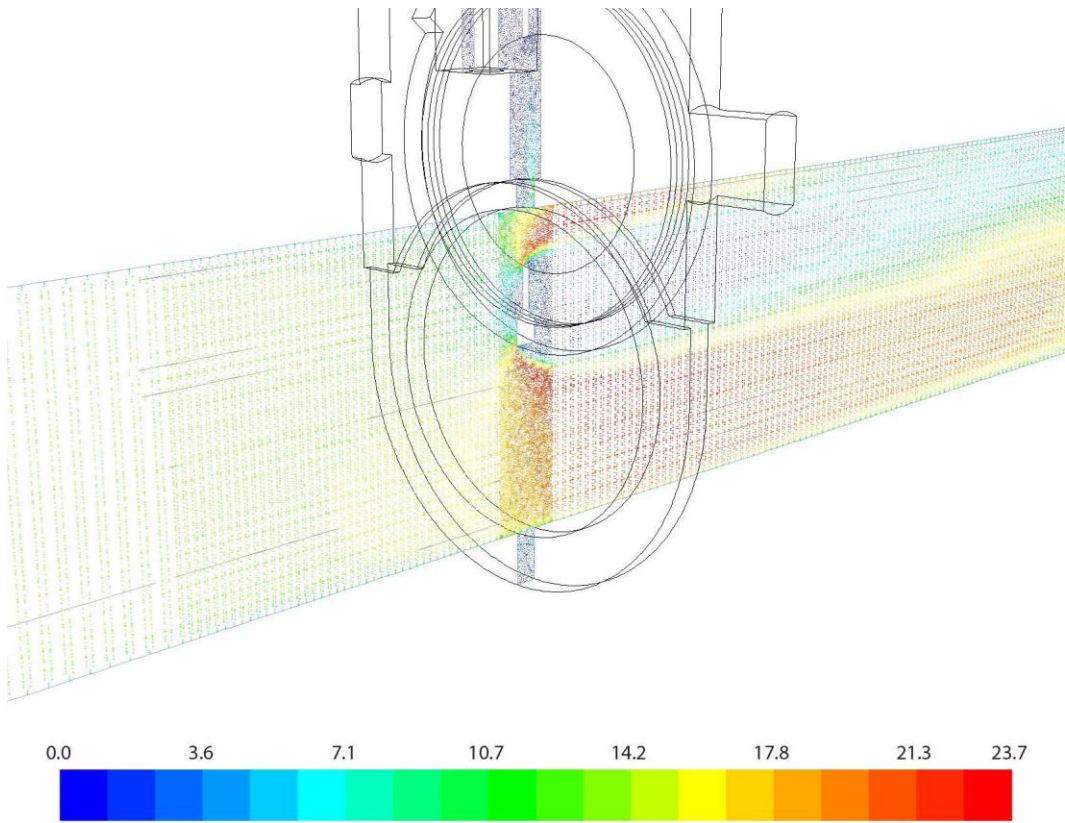
Figure 53. Velocity vector distribution on the mid x-y plane
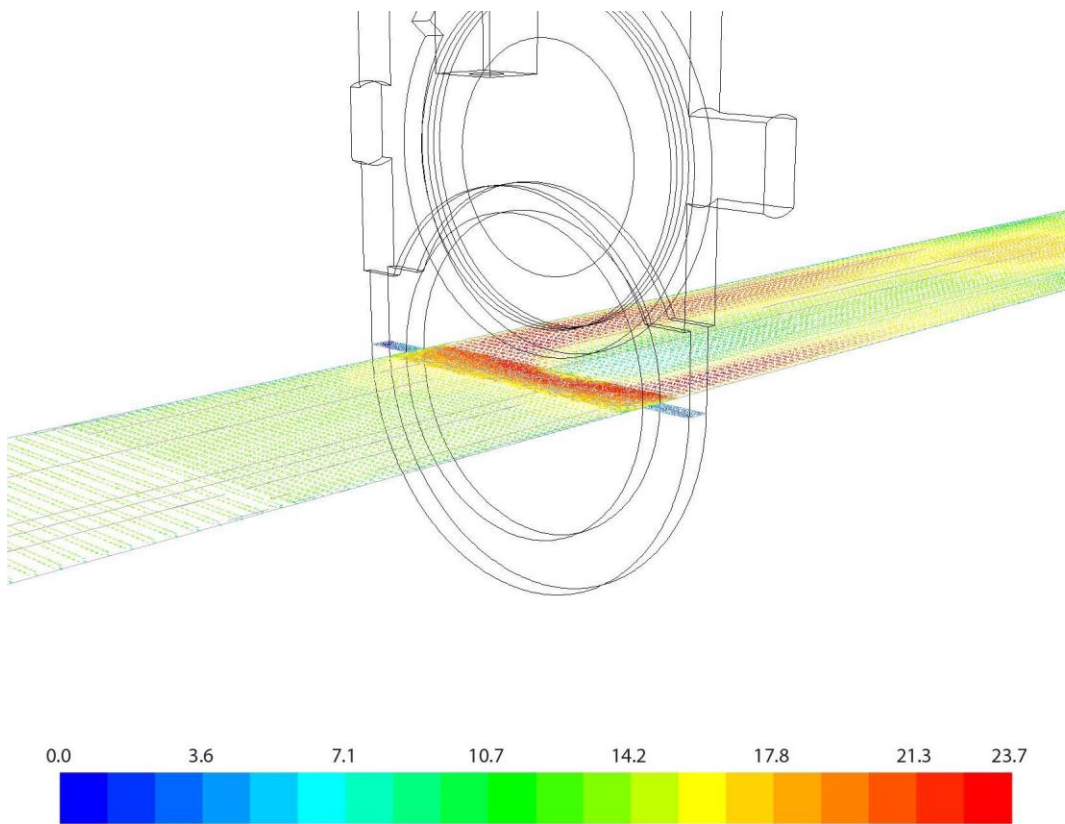
Figure 54. Velocity vector distribution on the mid x-z plane
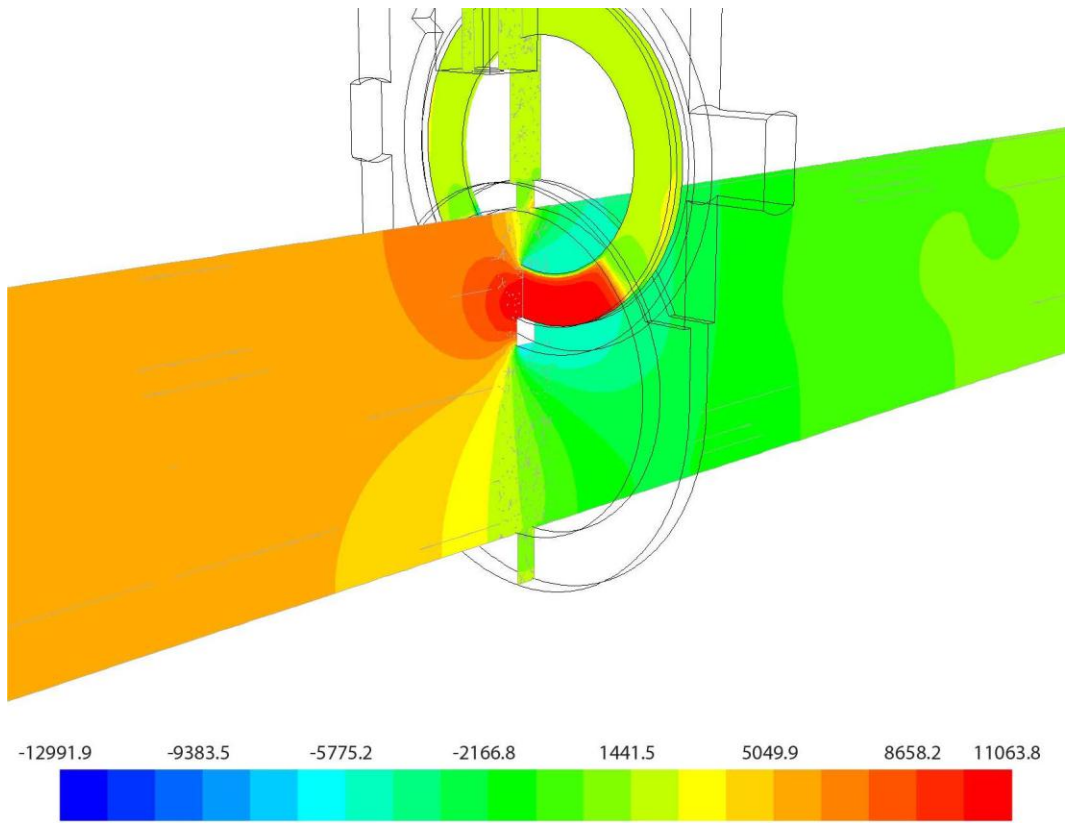
Figure 55. Pressure distribution on the mid x-y plane
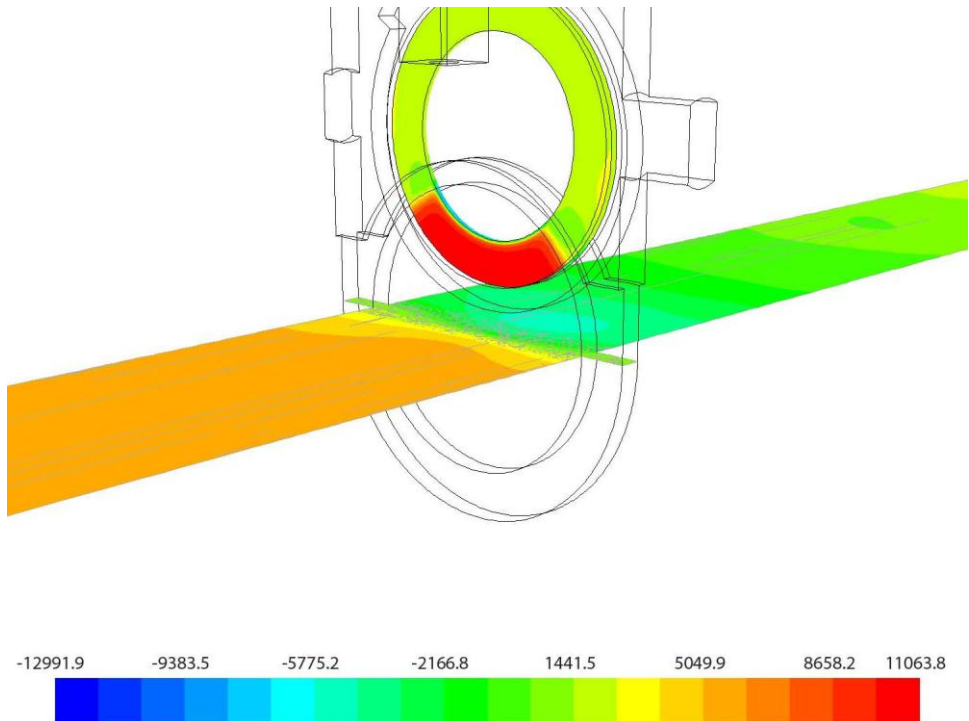
Figure 56. Pressure distribution on the mid x-z plane
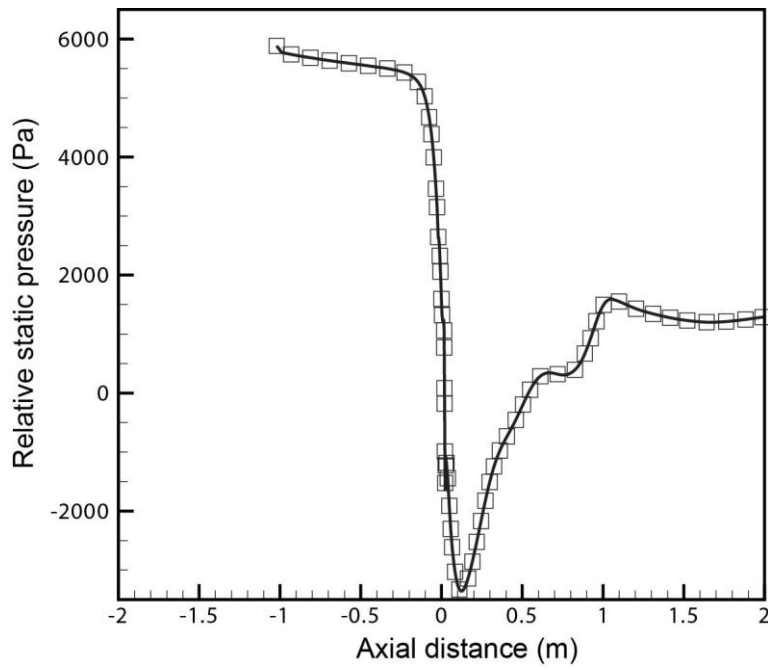
Figure 57. Case 985-3 – Pressure along a line near wall on the x-z plane.
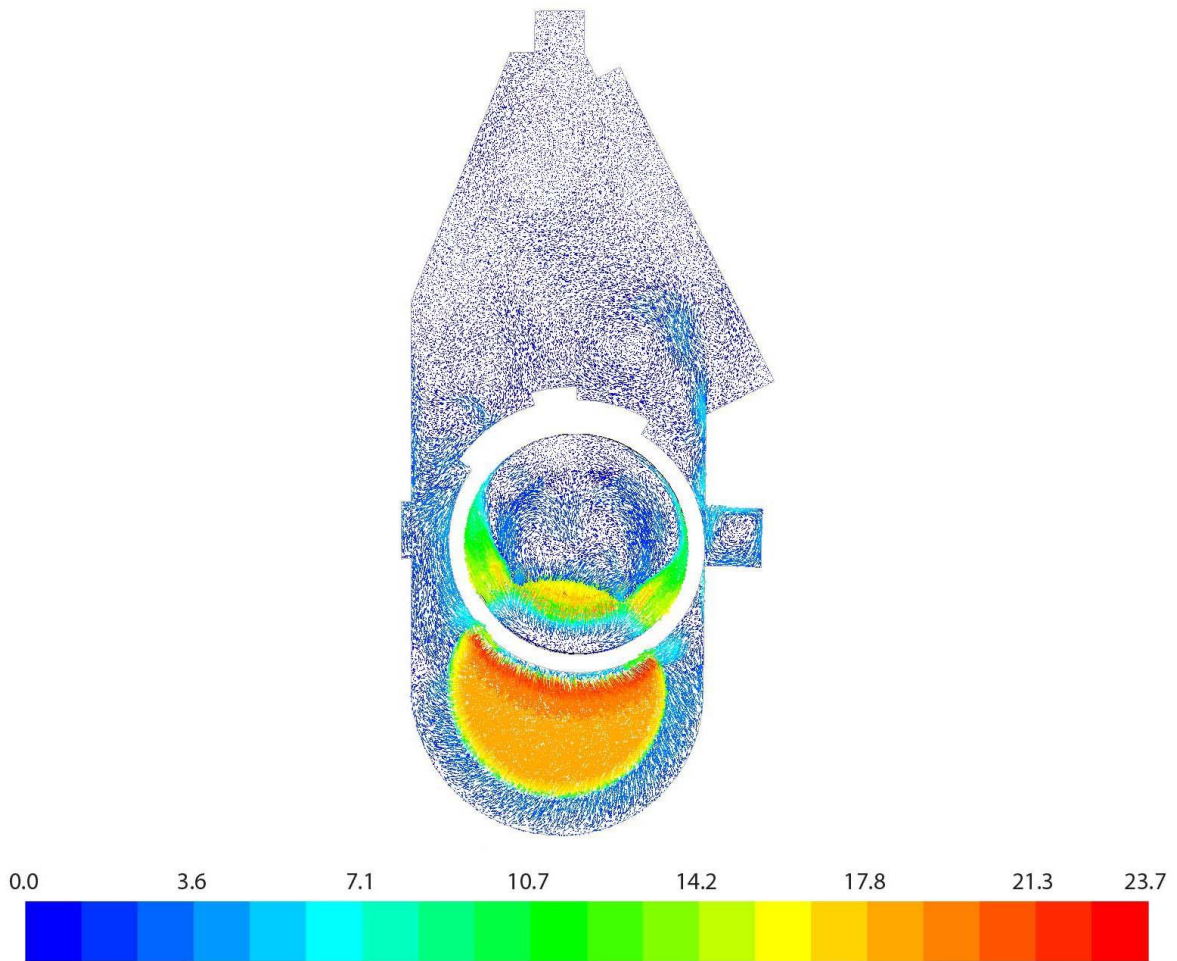
Figure 58. Velocity vector plot on a y-z plane at just before the orifice plate upstream face indicating flow leakage from the front to the carrier space.
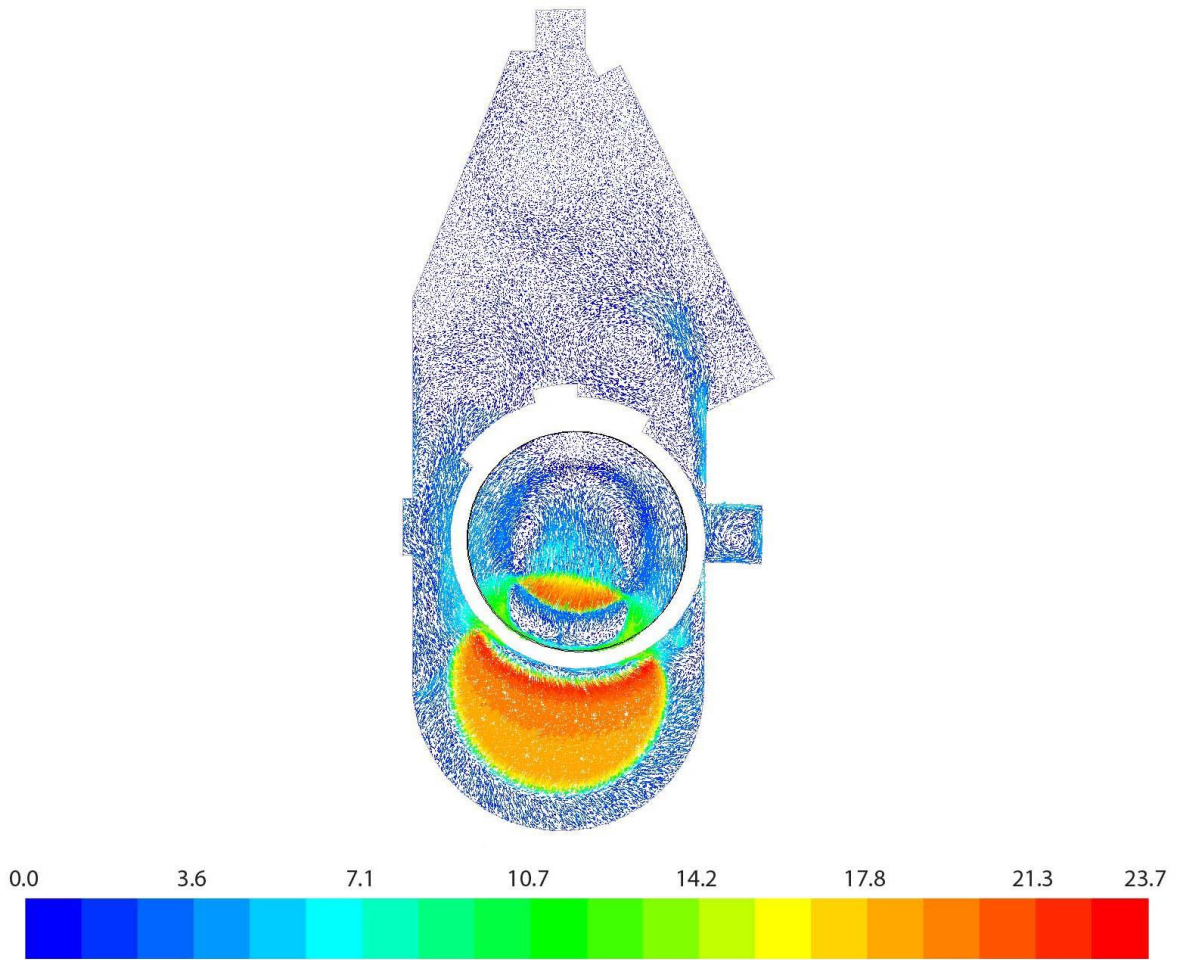
Figure 59. Velocity vector plot on a y-z plane at just after the orifice plate downstream face indicating flow back from the carrier space to the pipe
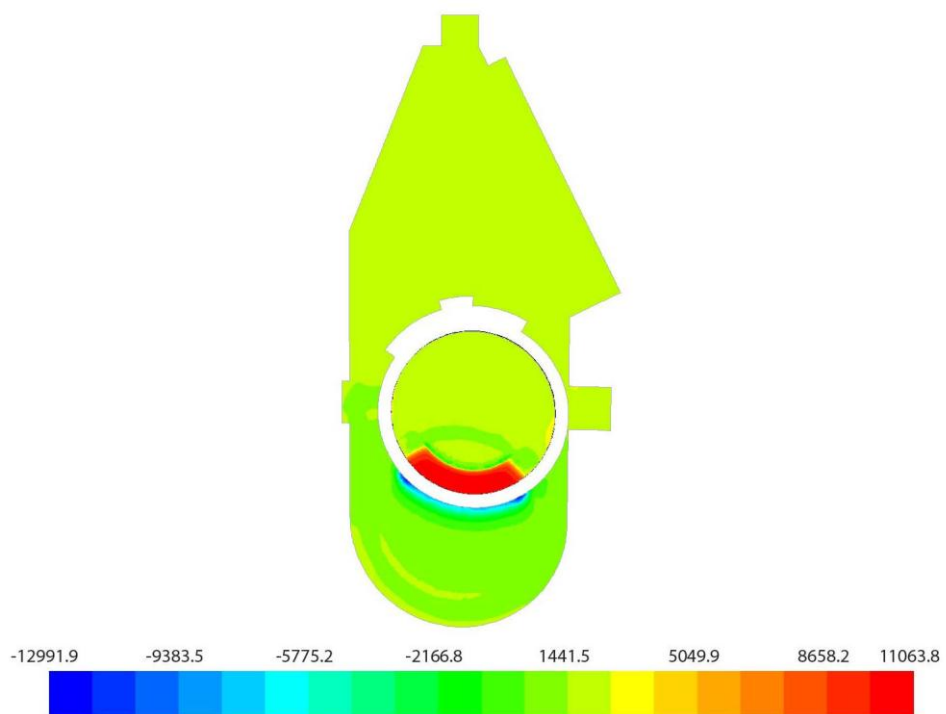
Figure 60. Static pressure contour plot on a y-z plane at just before the orifice plate
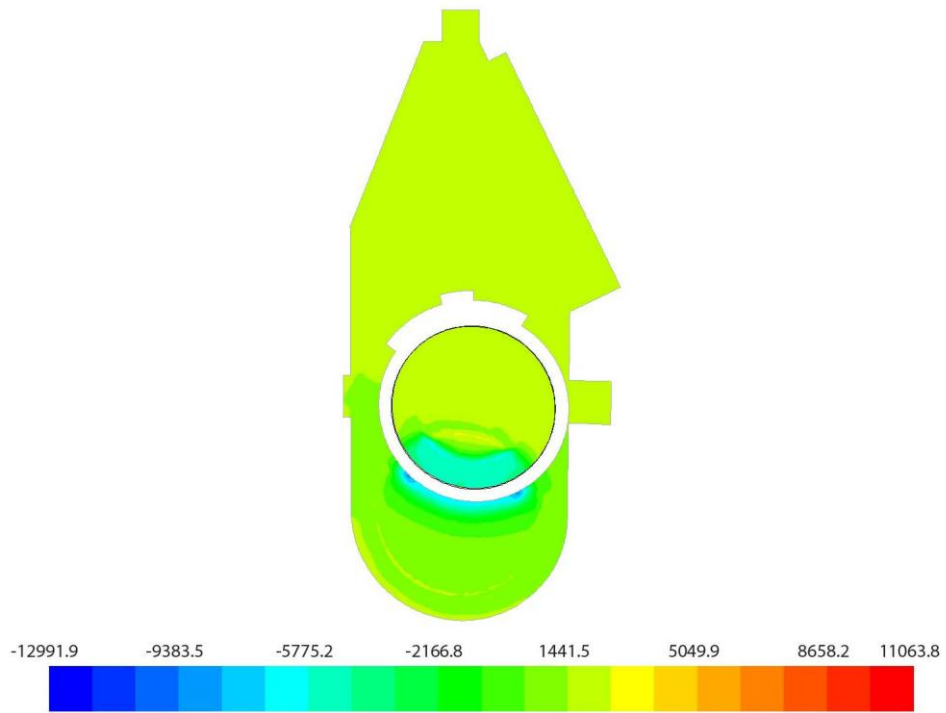
Figure 61. Static pressure contour plot on a y-z plane at just after the orifice plate downstream face.

Table 12 SUMMARY OF RESULTS FOR CASES 99950

Case id	Case considered and identification details	Actual flow rate (m³/h) and (Mass flow rate, kg/h)	Density (kg/m³) and viscosity	Model variation	Predicted DP (mbar)	Measured DP (mbar)	Error %	Remarks	% Difference of error between models (1&2, 2&3)
950-1	**CASE 99950 – TEST 1** Incorrect position - Eccentric dimensions are A = 210.5 mm, B=22.5 mm.	588.60 (33364.2584)	56.684 1.24e-5	**Grid_1** **Grid_2** **Grid_3**	**2.08** **1.98** **1.99**	1.39	**49.6%** **42.4%** **43.1%**	Uncertainty in measurements is above 15%	**-** **7.2%** **0.7%**
950-2	**CASE 99950 – TEST 2** Incorrect position - Eccentric dimensions are A = 210.5 mm, B=22.5 mm.	1619.6945 (92032.9718)	56.821 1.24e-5	**Grid_1** **Grid_2** **Grid_3**	**17.03** **16.23** **16.32**	16.07	**5.9%** **0.9%** **1.5%**	Uncertainty in measurements < 5 %	**-** **5.0%** **0.6%**
950-3	**CASE 99950 – TEST 3** Incorrect position - Eccentric dimensions are A = 210.5 mm, B=22.5 mm.	2459.8613 (141573.504)	57.553 1.24e-5	**Grid_1** **Grid_2** **Grid_3**	**38.47** **38.02** **37.98**	37.28	**3.1%** **1.9%** **1.8%**	Uncertainty in measurements < 2 %	**-** **1.2%** **0.2%**

950-4	**CASE 99950 – TEST 4** Incorrect position - Eccentric dimensions are A = 210.5 mm, B=22.5 mm.	1564.3494 (94042.855)	60.116 1.25e-5	**Grid_1** **Grid_2** **Grid_3**	**16.79** **16.02** **16.09**	14.60	**15.0%** **9.7%** **10.2%**	Uncertainty in measurements < 5 %	**-** **5.3%** **0.5%**
950-6	**CASE 99950 – TEST 6** Incorrect position - Eccentric dimensions are A = 210.5 mm, B=22.5 mm.	541.2844 (32562.3366)	60.157 1.25e-5	**Grid_1** **Grid_2** **Grid_3**	**2.01** **1.92** **1.91**	1.85	**8.6%** **3.7%** **3.2%**	Uncertainty in measurements is above 15%	**-** **4.9%** **0.5%**
950-7	**CASE 99950 – TEST 7** Incorrect position - Eccentric dimensions are A = 210.5 mm, B=22.5 mm.	2284.8572 (137055.98)	59.984 1.25e-5	**Grid_1** **Grid_2** **Grid_3**	**35.90** **34.32** **34.28**	33.42	**7.4%** **2.6%** **2.5%**	Uncertainty in measurements < 3 %	**-** **4.8%** **0.1%**
950-8	**CASE 99950 – TEST 8** Incorrect position - Eccentric dimensions are A = 210.5 mm, B=22.5 mm.	1748.498 (92917.081)	53.118 1.23e-5	**Grid_1** **Grid_2** **Grid_3**	**18.54** **17.84** **17.77**	17.43	**6.3%** **2.3%** **1.9%**	Uncertainty in measurements < 4.5%	**-** **4.0%** **0.4%**
950-9	**CASE 99950 – TEST 9** Incorrect position - Eccentric dimensions are A = 210.5 mm, B=22.5 mm.	608.80 (32689.86)	53.695 1.23e-5	**Grid_1** **Grid_2** **Grid_3**	**2.27** **2.18** **2.18**	2.83	**19.7%** **22.9%** **22.9%**	Uncertainty in measurements is above 15%	**-** **3.2%** **0.0%**

950-10	**CASE 99950 – TEST 10** Incorrect position - Eccentric dimensions are A = 210.5 mm, B=22.5 mm.	2506.863 (133026.445)	53.064 1.23e-5	Grid_1	37.95		8.5%	Uncertainty in measurements < 2.5 %	-
				Grid_2	36.57	34.96	4.6%		3.9%
				Grid_3	36.43		4.2%		0.4%
950-11	**CASE 99950 – TEST 11** Incorrect position - Eccentric dimensions are A = 210.5 mm, B=22.5 mm.	633.819 (33806.983)	53.338 1.23e-5	Grid_1	2.44		20.5%	Uncertainty in measurements is above 15%	-
				Grid_2	2.35	3.07	23.4%		2.9%
				Grid_3	2.35		23.4%		0.0%

9.   Summary of CFD results

CFD analysis of fluid flow to calculate resulting DP in several non-standard orifice plate situations were considered in this study. The situation has arisen from a misalignment of an orifice plate in orifice plate carrier geometry. On site experimental tests have been conducted to investigate the resulting DP at various positions of the orifice plate. For the CFD analysis, cases from three test series known as 99970, 99985 and 99950 were considered. The CFD method used was based on the control volume technique and used Reynolds Averaged Navier-Stokes (RANS) methodology employing the SIMPLE algorithm and a turbulence model. The well-known $k - \varepsilon$ model was used for the turbulence closure. The geometries used in the models were built using available drawings of the carrier geometry, orifice plate data and various other geometrical data relevant to the metering site were also used in the model. Measured flow rates and gas properties were used as boundary conditions in the calculations. The results show that CFD predicted pressure differential values for a majority of cases considered agree reasonably well with measured pressure differentials. However, it should be noted that for very low flow rate test cases of the series 99950 which results in small pressure differentials, CFD predictions show some disagreements in predicting the resulting pressure differential. In general CFD results can also be used to visualise the flow situation in each geometry configuration and they provide an insight into how the flow behaves in a given geometry and provide details of the pressure distribution that gives the DP at pressure tapping locations.

Overall, the majority of the CFD results have agreed very well with the experimental measurements. CFD simulations have reproduced the experimental DP trends seen in several misaligned orifice plate configurations and response to different flow rates under different operating conditions. In this regard CFD simulations confirm the experimental results and the observed experimental trends.

References

[1]   ISO-5167-1, Measurement of fluid flow by means of pressure differential devices inserted in circular cross-section conduits running full - Part 1: General principles and requirements, ISO publication.

[2]   ISO 5167-2:2003, Measurement of fluid flow by means of pressure differential devices inserted in circular cross-section conduits running full -- Part 2: Orifice plates, ISO publication.

[3]   Versteeg, H.K. and Malalasekera, W., An Introduction to Computational Fluid Dynamics : The Finite Volume Method, Second Edition, Pearson Education Ltd., Harlow, Essex, UK, January 2007, 520 pp, ISBN 0-978-0-13-127498-3., Chinese Edition, ISBN 978-7-5100-0557-2, Asian Edition , ISBN 978-81-317-2048-6, Japanese Edition (in Japanese language), ISBN 978-4-627-91972-3.
http://www.amazon.co.uk/Introduction-Computational-Fluid-Dynamics-Finite/dp/0131274988/

http://www.amazon.co.jp/gp/product/images/4627919727/ref=dp_image_text_0?ie=UTF8&n=465392&s=books

[4]   CFD validation studies for incompressible flow through square-edged orifice plates, ESDU TN 10013 Technical Report, 2011, HIS Global Ltd publication.

[5]   CFD Best Practice Guidelines for modelling pressure losses and flow characteristics in square- and knife-edged orifice plates, ESDU CFD BPG 11010 Technical Report, 2011, HIS Global Ltd publication.

[6]   Shah, M., Joshi, J.B., Kalsi, A.S., Prasad, C.S.R. and Shukla, D.S., Analysis of flow through an orifice meter: CFD Simulation, Chemical Engineering Science, Vol. 71, pp. 300-309, 2012.

APPENDIX A

APPENDIX A

Comparison of the results from a short model and a long model for inlet-outlet pipe lengths

Case 99985 test series

During the review of the CFD work, the reviewers suggested the following modifications to the model.

Recommendations from the reviewer's report

1   Reduce the size of the model. The model should be 2D upstream and 10D downstream. No thermowell to be included in the model.

2   Re-mesh the model using hexahedral elements where possible.

3   Refine the elements around the sharp edge of the orifice plate.

4   Demonstrate mesh independence.

Revised CFD work undertaken to accommodate above recommendations

1. The original model used for Cases 99985 was modified using 2D upstream, 10D downstream (without the thermowell) and all test cases of the 99985 test series were re-run with the new short model. Two grids were used in the calculations. These cases are named 985 Short Models 1 and 2. In these meshes boundary layer meshes were incorporated to maintain y+, hexahedral elements were used as much as possible and refined tetrahedral mesh densities were used around orifice edge area of the carrier geometry.

2. The original model was re-meshed to incorporate boundary layer meshes to maintain y+. Hexahedral elements were used as much as possible and refined tetrahedral mesh densities were used around orifice edge area of the carrier geometry. Two grids were used in the initial calculations. These models are identified as Long Model 1 and 2.

3. All results from the above models were compared with experimental data.

TEST CASES 99985 – TESTS 01 to 11

1.1 Details of the case considered (985 Short Model 1)

Plate details and flow situation	Plate 052/2, incorrect position 99985
CFD geometry	2D upstream, 10D downstream
Grid characteristics	Majority hexahedral elements with tetrahedral elements near the plate and carrier space. Fine mesh for orifice edges. Boundary layer mesh for pipe wall surfaces. No thermowell.
Grid size	985 Short Model 1 – Grid 1 **2.78 million cells – majority hexahedral**
Flow rate and properties	See Table A1
Other model details	k-ε turbulence model is used 2nd order upwind discretisation scheme Pipe wall roughness height 32.6 Ra
Measured DP	See table for each case
Name of the model	**985 S_Model 1**
Model characteristics against recommendations 1. Short model 2. Re-mesh the model with hex. elements 3. Refine the elements around sharp edge 4. Sharp edge modelled in accurate details 5. Demonstrate mesh independence	 Yes Yes Yes Yes See below

1.2   Details of the case considered (985 Short Model 2)

Plate details and flow situation	Plate 052/2, incorrect position 99985
CFD geometry	2D upstream, 10D downstream
Grid characteristics	Majority hexahedral elements with tetrahedral elements near the plate and carrier space. Fine mesh for orifice edges. Boundary layer mesh for pipe wall surfaces. No thermowell.
Grid size	985 Short Model 2 – Grid 2 **2.88 million cells – majority hexahedral**
Flow rate and properties	See Table 1
Other model details	k-ε turbulence model is used 2nd order upwind discretisation scheme Pipe wall roughness height 32.6 Ra
Measured DP	See table for each case
Name of the model	**985 S_Model 2**
Model characteristics against recommendations 1. Short model 2. Re-mesh the model with hex. elements 3. Refine the elements around sharp edge 4. Sharp edge modelled in accurate details 5. Demonstrate mesh independence	Yes Yes Yes Yes See below

Table A.1 SUMMARY OF RESULTS FOR CASES 99985 SHORT MODELS 1 & 2

Case id	Case considered and identification details	Actual flow rate (m³/h) and (Mass flow rate, kg/h)	Density (kg/m³) and viscosity	Short Model variation	Predicted DP (mbar)	Measured DP (mbar)	Error %	Remarks
985-1	**CASE 99985 – TEST 1** Incorrect position - Eccentric dimensions are A = 87.23, B=17.5 mm.	594.4561 (33696.1843)	56.684 1.24e-5	**S_Model_1** **S_Model_2** **Diff.**	**15.08** **14.99**	13.784	**9.4%** **8.7%** **0.7%**	Uncertainty in measurements < 5 %
985-2	**CASE 99985 – TEST 2** Incorrect position - Eccentric dimensions are A = 87.23, B=17.5 mm.	1598.6628 (90950.2459)	56.892 1.24e-5	**S_Model_1** **S_Model_2** **Diff.**	**109.21** **108.64**	103.136	**5.8%** **5.3%** **0.5%**	Uncertainty in measurements < 2 %
985-3	**CASE 99985 – TEST 3** Incorrect position - Eccentric dimensions are A = 87.23, B=17.5 mm.	2396.1463 (138132.993)	57.647 1.24e-5	**S_Model_1** **S_Model_2** **Diff.**	**247.76** **247.89**	242.939	**1.9%** **2.0%** **0.1%**	Uncertainty in measurements < 1 %

985-4	**CASE 99985 – TEST 4** Incorrect position - Eccentric dimensions are A = 87.23, B=17.5 mm.	1540.5865 (92601.981)	60.108 1.25e-5	**S_Model_1** **S_Model_2** **Diff.**	**106.99** **106.64**	102.495	**4.3%** **4.0%** **0.3%**	Uncertainty in measurements < 2 %
985-6	**CASE 99985 – TEST 6** Incorrect position - Eccentric dimensions are A = 87.23, B=17.5 mm.	534.9225 (32179.62)	60.158 1.25e-5	**S_Model_1** **S_Model_2** **Diff.**	**12.97** **12.88**	12.062	**7.5%** **6.7%** **0.8%**	Uncertainty in measurements < 6 %
985-7	**CASE 99985 – TEST 7** Incorrect position - Eccentric dimensions are A = 87.23, B=17.5 mm.	2174.3146 (130547.98)	60.041 1.25e-5	**S_Model_1** **S_Model_2** **Diff.**	**212.69** **212.60**	208.331	**2.0%** **2.0%** **0.0%**	Uncertainty in measurements < 1 %

985-8	**CASE 99985 – TEST 8** Incorrect position - Eccentric dimensions are A = 87.23, B=17.5 mm.	1729.112 (91847.114)	53.118 1.23e-5	**S_Model_1** **S_Model_2** **Diff.**	**119.22** **118.68**	112.566	**5.9%** **5.4%** **0.5%**	Uncertainty in measurements < 1.5%
985-9	**CASE 99985 – TEST 9** Incorrect position - Eccentric dimensions are A = 87.23, B=17.5 mm.	609.996 (32754.048)	53.695 1.23e-5	**S_Model_1** **S_Model_2** **Diff.**	**15.04** **14.94**	14.067	**6.9%** **6.2%** **0.7%**	Uncertainty in measurements < 5 %
985-10	**CASE 99985 – TEST 10** Incorrect position - Eccentric dimensions are A = 87.23, B=17.5 mm.	2415.2228 (128274.12)	53.111 1.23e-5	**S_Model_1** **S_Model_2** **Diff.**	**232.40** **232.07**	217.578	**6.8%** **6.6%** **0.2%**	Uncertainty in measurements < 1 %

985-11	CASE 99985 – TEST 11 Incorrect position - Eccentric dimensions are A = 87.23, B=17.5 mm.	648.0378 (34565.349)	53.338 1.23e-5	S_Model_1	16.85	15.981	5.4%	Uncertainty in measurements < 4.5 %
				S_Model_2	16.74		4.7%	
				Diff.			0.7%	

Note: Mesh 2 (or Model 2) is 100197 cells finer than Model 1. It can be seen that the results between Shorter Model 1 and 2 are less than 1%.

1.3   Details of the case considered (985 Long Model 1)

Plate details and flow situation	Plate 052/2, incorrect position 99985
CFD geometry	Original model including the thermowell
Grid characteristics	Majority hexahedral elements with tetrahedral elements near the plate and carrier space. Fine mesh for orifice edges. Boundary layer mesh for pipe wall surfaces.
Grid size	985 Long Model 1 – Grid 1 **2.44 million cells – majority hexahedral**
Flow rate and properties	See Table 2
Other model details	k-ε turbulence model is used 2nd order upwind discretisation scheme Pipe wall roughness height 32.6 Ra
Measured DP	See table for each case
Name of the model	**985 L_Model 1**

Model characteristics against recommendations
   1. Short model
   2. Re-mesh the model with hex. elements
   3. Refine the elements around sharp edge
   4. Sharp edge modelled in accurate details
   5. Demonstrate mesh independence
	
	No
	
	Yes
	
	Yes
	
	Yes
	See below

1.4 Details of the case considered (985 Long Model 2)

Plate details and flow situation	Plate 052/2, incorrect position 99985
CFD geometry	Original model including the thermowell
Grid characteristics	Majority hexahedral elements with tetrahedral elements near the plate and carrier space. Fine mesh for orifice edges. Boundary layer mesh for pipe wall surfaces.
Grid size	985 Long Model 2 – Grid 2 **2.9 million cells – majority hexahedral**
Flow rate and properties	See Table 2
Other model details	k-ε turbulence model is used 2nd order upwind discretisation scheme Pipe wall roughness height 32.6 Ra
Measured DP	See table for each case
Name of the model	**985 L_Model 2**
Model characteristics against recommendations 　1. Short model 　2. Re-mesh the model with hex. elements 　3. Refine the elements around sharp edge 　4. Sharp edge modelled in accurate details 　5. Demonstrate mesh independence	 No Yes Yes Yes See below

Table A.2 SUMMARY OF RESULTS FOR CASES 99985 LONG MODELS 1 & 2 (ORIGINAL GEOMETRY)

Case id	Case considered and identification details	Actual flow rate (m³/h) and (Mass flow rate, kg/h)	Density (kg/m³) and viscosity	Short Model variation	Predicted DP (mbar)	Measured DP (mbar)	Error %	Remarks
985-1	**CASE 99985 – TEST 1** Incorrect position - Eccentric dimensions are A = 87.23, B=17.5 mm.	594.4561 (33696.1843)	56.684 1.24e-5	**L_Model_1** **L_Model_2** **Diff.**	**14.68** **14.43**	13.784	**6.5%** **4.7%** **1.8%**	Uncertainty in measurements < 5 %
985-2	**CASE 99985 – TEST 2** Incorrect position - Eccentric dimensions are A = 87.23, B=17.5 mm.	1598.6628 (90950.2459)	56.892 1.24e-5	**L_Model_1** **L_Model_2** **Diff.**	**106.25** **104.71**	103.136	**3.0%** **1.5%** **1.5%**	Uncertainty in measurements < 2 %
985-3	**CASE 99985 – TEST 3** Incorrect position - Eccentric dimensions are A = 87.23, B=17.5 mm.	2396.1463 (138132.993)	57.647 1.24e-5	**L_Model_1** **L_Model_2** **Diff.**	**241.54** **237.72**	242.939	**0.5%** **2.1%** **1.6%**	Uncertainty in measurements < 1 %

985-4	**CASE 99985 – TEST 4** Incorrect position - Eccentric dimensions are A = 87.23, B=17.5 mm.	1540.5865 (92601.981)	60.108 1.25e-5	**L_Model_1** **L_Model_2** **Diff.**	**104.23** **102.56**	102.495	**1.6%** **0%** **1.6%**	Uncertainty in measurements < 2 %
985-6	**CASE 99985 – TEST 6** Incorrect position - Eccentric dimensions are A = 87.23, B=17.5 mm.	534.9225 (32179.62)	60.158 1.25e-5	**L_Model_1** **L_Model_2** **Diff.**	**12.62** **12.31**	12.062	**4.6%** **2.8%** **1.8%**	Uncertainty in measurements < 6 %
985-7	**CASE 99985 – TEST 7** Incorrect position - Eccentric dimensions are A = 87.23, B=17.5 mm.	2174.3146 (130547.98)	60.041 1.25e-5	**L_Model_1** **L_Model_2** **Diff.**	**207.52** **203.88**	208.331	**0.3%** **2.1%** **1.8%**	Uncertainty in measurements < 1 %

985-8	**CASE 99985 – TEST 8** Incorrect position - Eccentric dimensions are A = 87.23, B=17.5 mm.	1729.112 (91847.114)	53.118 1.23e-5	**L_Model_1** **L_Model_2** **Diff.**	**116.05** **114.17**	112.566	**3.1%** **1.4%** **1.7%**	Uncertainty in measurements < 1.5%
985-9	**CASE 99985 – TEST 9** Incorrect position - Eccentric dimensions are A = 87.23, B=17.5 mm.	609.996 (32754.048)	53.695 1.23e-5	**L_Model_1** **L_Model_2** **Diff.**	**14.63** **14.39**	14.067	**4.0%** **2.3%** **1.7%**	Uncertainty in measurements < 5 %
985-10	**CASE 99985 – TEST 10** Incorrect position - Eccentric dimensions are A = 87.23, B=17.5 mm.	2415.2228 (128274.12)	53.111 1.23e-5	**L_Model_1** **L_Model_2** **Diff.**	**226.40** **222.93**	217.578	**4.0%** **2.4%** **1.6%**	Uncertainty in measurements < 1 %

| 985-11 | **CASE 99985 – TEST 11**
Incorrect position - Eccentric dimensions are A = 87.23, B=17.5 mm. | 648.0378
(34565.349) | 53.338
1.23e-5 | **L_Model_1**

L_Model_2

Diff. | **16.40**

16.12 | 15.981 | **2.6%**

0.8%

1.8% | Uncertainty in measurements < 4.5 % |

Note: Long Model 2 is 464160 cells finer than the Long Model 1.

Conclusions of these comparisons

Short Model 2 mesh contains 2.88 million cells which is finer than the Long Model 1 which is 2.44 million cells. Yet the results of Long Model 1 (Table A.2) are closer to the measured data than the Short Model 2 (Table A.1). Based on these results it was concluded that the longer model based on original geometry was more accurate than the shorter model therefore the long model with new meshes was used as the preferred option to conduct all other test cases. It was also observed that a third Grid is required to demonstrate mesh independence where the differences between results from two grids is less than 1% in majority of the 99985 test cases. It is seen from the vector plots presented in the main report that when the orifice plate is severely misaligned (such as Case 99985) the resulting flow is more wall bound wall-jet like flow and the flow does not recover to a standard pipe flow profile for a long distance therefore a long model is required for successful predictions.

Appendix B

A note on meshes used in each case and y+ values

B.1   Cases 1 and 2 – Grid 3

Figure B.1 shows a cross section of the mesh through the central plane of the geometry. For meshing purposes the overall geometry has been divided into several sections in order to use hexahedral elements where possible and tetrahedral elements are used in geometry sections where geometry details could not be meshed with hexahedral elements. Here the figure shows a cross section containing the orifice plate. Tetrahedral elements are used to mesh the section containing the orifice plate where 0.5 mm grid spacing is used to mesh orifice plate edges. It can be seen that orifice plate edge is accurately represented in the model with a mesh spacing of 0.5 mm. A combination of tetrahedral and hexahedral elements totalling 2997933 cells is used in this mesh. It should be noted that what is shown Figure B.1 is a cross section of the 3D mesh containing tetrahedral elements at the orifice section which has been cut across the centre plane for displaying the cut mesh section; hence the grid shapes displayed do not have regular shapes. The plotting facility does not allow an exact cutting plane hence it should be noted that the location of the shown central plane is approximately close to the true centre. The figure also shows the size change indicated by colour. Mesh size change is a quality measure and a blue colour indicates good quality. Grid expansion ratio is kept below 1.2 (this is the recommended value) and maximum skewness index is kept below 0.8 the recommended maximum value is 0.95.
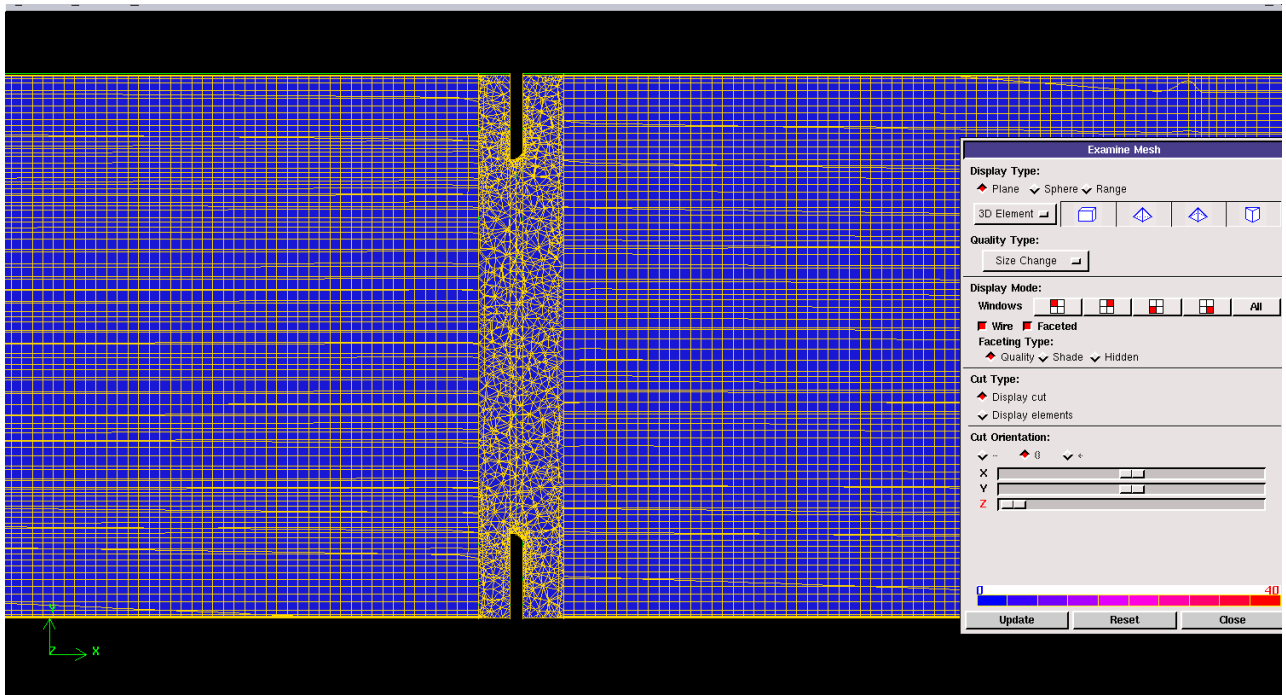

Figure B.1 – A grid plane across the orifice plate and grid quality measure of size change for Cases 1 & 2, Grid 3. Blue colour indicates good quality.

B. 2   Case 3 – Grid 3

Figure B.2 shows a cross section of the mesh through the geometry of Case 3. As before for meshing purposes the overall geometry has been divided into several sections in order to use hexahedral elements where possible and tetrahedral elements are used in geometry sections where details could not be meshed with hexahedral elements. Here the figure shows a cross section containing the orifice plate and 0.5 mm grid spacing is used to mesh orifice plate edges where tetrahedral elements are used to mesh the section containing the orifice plate. It can be seen that orifice plate edge is accurately represented in the model with a mesh spacing of 0.5 mm. A combination of tetrahedral and hexahedral elements totalling 3011613 cells is used in this mesh. It should be noted that what is shown Figure B.2 is a cross section of the 3D mesh containing tetrahedral elements at the orifice section which has been cut across the centre plane for displaying the cut mesh section; hence the grid shapes displayed do not have regular shapes. The plotting facility does not allow an exact cutting plane hence it should be noted that the location of the shown central plane is approximately close to the true centre. The figure also shows the size change indicated by colour. Mesh size change is a quality measure and a blue colour indicates good quality. Grid expansion ratio is kept below 1.2 (this is the recommended value) and maximum skewness index is kept below 0.8 the recommended maximum value is 0.95.
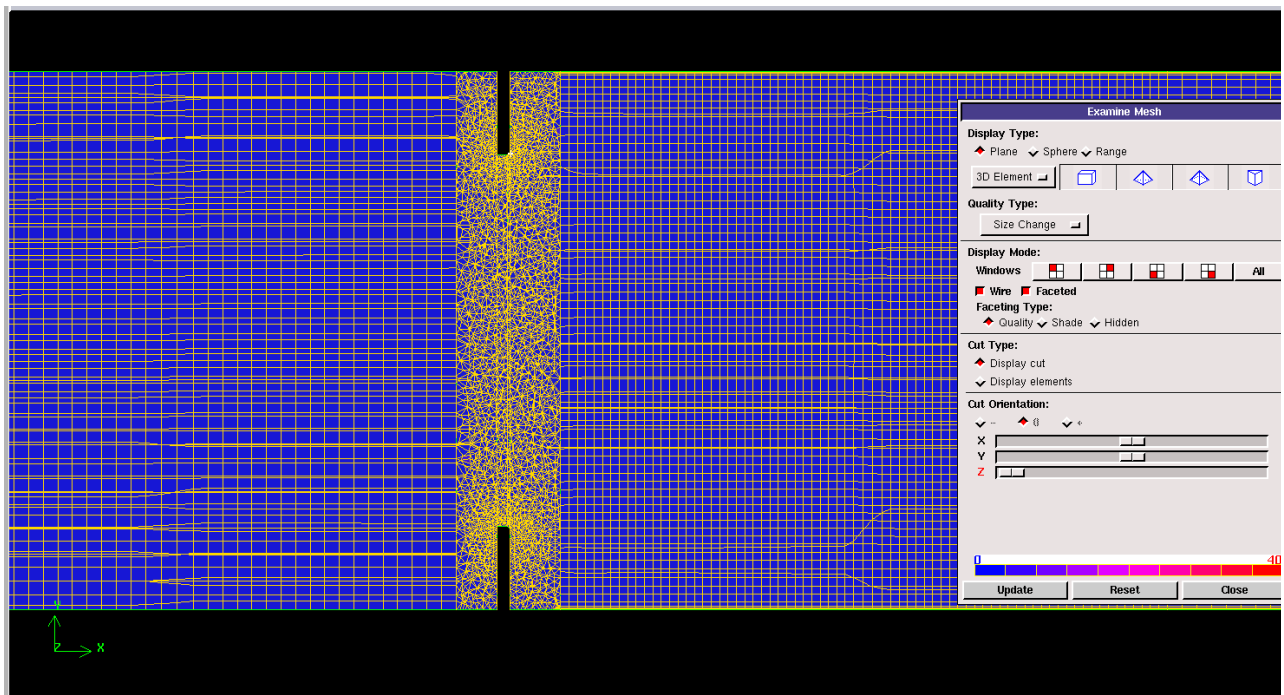
Case 3 – Grid 3

Figure B.2 – A grid plane across the orifice plate and grid quality measure of size change for Case 3, Grid 3. Blue colour indicates good quality.

B. 3   Case 99970 – Grid 3

Figure B.3 shows the cross section of the mesh through the geometry. Here the carrier geometry containing the orifice plate has a large complex volume hence a large number of cells are required for that part alone. For meshing purposes the overall geometry has been divided into several sections in order to use hexahedral elements where possible and tetrahedral elements are used in geometry sections where details could not be meshed with hexahedral elements. Here the figure shows a cross section containing the orifice plate and the carrier geometry. A grid size of 0.5 mm is used to mesh orifice plate

edges and tetrahedral elements are used to mesh the orifice plate area and carrier geometry. It can be seen that orifice plate edge is accurately represented in the model with a mesh spacing of 0.5 mm. A combination of tetrahedral and hexahedral elements totalling 2997933 cells is used in this mesh. It should be noted that what is shown Figure B.3 is a cross section of the 3D mesh containing tetrahedral elements at the orifice section which has been cut across the central plane for displaying the cut mesh section; hence the grid shapes displayed do not have regular shapes. The plotting facility does not allow an exact cutting plane hence it should be noted that the location of the shown central plane is approximately close to the true centre. The figure also shows the size change indicated by colour. Mesh size change is a quality measure and a blue colour indicates good quality. Grid expansion ratio is kept below 1.2 (this is the recommended value) and maximum skewness index is kept below 0.8 the recommended maximum value is 0.95.
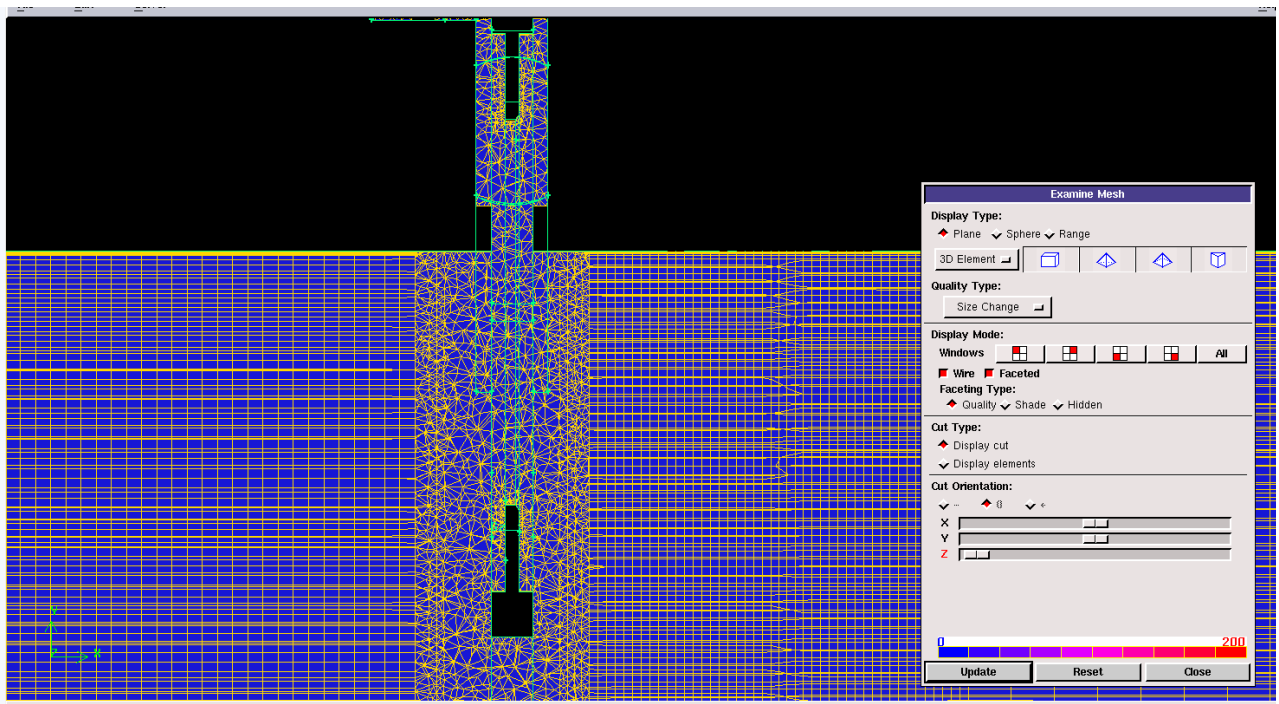
Case 99970 – Grid 3

Figure B.3 – A grid plane across the orifice plate and grid quality measure of size change for Case 99970, Grid 3. Blue colour indicates good quality.

B. 4   Case 99985 – Grid 3

Figure B.4 shows the cross section of the mesh used in Cases 99985. As in the previous case here the carrier geometry containing the orifice plate has a large complex volume hence a large number of cells are required for that part alone. For meshing purposes the overall geometry has been divided into several sections in order to use hexahedral elements where possible and tetrahedral elements are used in geometry sections where details could not be meshed with hexahedral elements. Here the figure shows a cross section containing the orifice plate and the carrier geometry. A grid size of 0.5 mm is used to mesh orifice plate edges and tetrahedral elements are used to mesh the orifice plate area and carrier geometry. It can be seen that orifice plate edge is accurately represented in the model with a mesh spacing of 0.5 mm. A combination of

tetrahedral and hexahedral elements totalling 2997933 cells is used in this mesh. It should be noted that what is shown Figure B.4 is a cross section of the 3D mesh containing tetrahedral elements at the orifice section which has been cut across the central plane for displaying the cut mesh section; hence the grid shapes displayed do not have regular shapes. The plotting facility does not allow an exact cutting plane hence it should be noted that the location of the shown central plane is approximately close to the true centre. The figure also shows the size change indicated by colour. Mesh size change is a quality measure and blue colour indicates good quality. Grid expansion ratio is kept below 1.2 (this is the recommended value) and maximum skewness index is kept below 0.8 the recommended maximum value is 0.95.
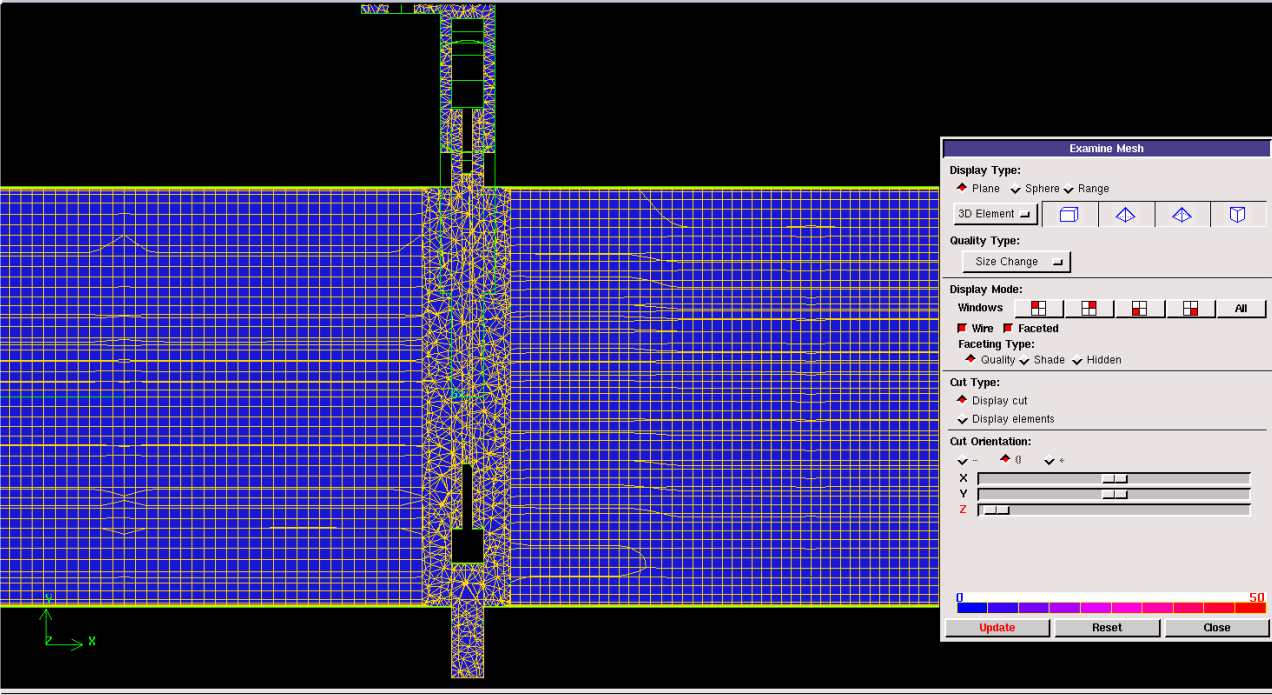
Case 99985 – Grid 3

Figure B.4 – A grid plane across the orifice plate and grid quality measure of size change for Case 99985, Grid 3. Blue colour indicates good quality.

B. 5   Case 99950 – Grid 3

Figure B.5 shows the cross section of the mesh used in Cases 99985. As in the previous case here the carrier geometry containing the orifice plate has a large complex volume hence a large number of cells are required for that part alone. For meshing purposes the overall geometry has been divided into several sections in order to use hexahedral elements where possible and tetrahedral elements are used in geometry sections where details could not be meshed with hexahedral elements. Here the figure shows a cross section containing the orifice plate and the carrier geometry. A grid size of 0.5 mm is used to mesh orifice plate edges and tetrahedral elements are used to mesh the orifice plate area and carrier geometry. It can be seen that orifice plate edge is accurately represented in the model with a mesh spacing of 0.5 mm. A combination of tetrahedral and hexahedral elements totalling 3032103 cells is used in this mesh. It should be noted that what is shown Figure B.5 is a cross section of the 3D mesh

containing tetrahedral elements at the orifice section which has been cut across the central plane for displaying the cut mesh section; hence the grid shapes displayed do not have regular shapes. The plotting facility does not allow an exact cutting plane hence it should be noted that the location of the shown central plane is approximately close to the true centre. The figure also shows the size change indicated by colour. Mesh size change is a quality measure and a blue colour indicates good quality. Grid expansion ratio is kept below 1.2 (this is the recommended value) and maximum skewness index is kept below 0.8 the recommended maximum value is 0.95.
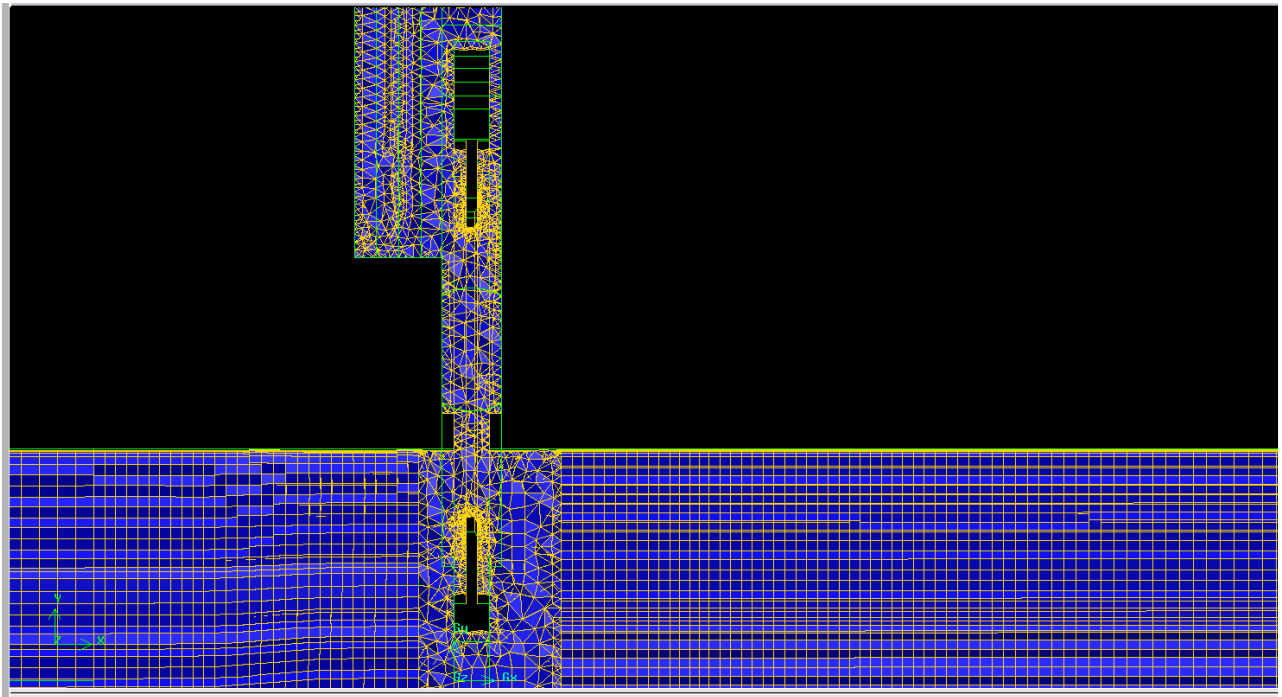

Figure B.5 – A grid plane across the orifice plate and grid quality measure of size change for Case 99950, Grid 3. Blue colour indicates good quality.

B. 6 A note on y+ values

It can be seen in Figures B.1 – B.5 that boundary layer meshes have been employed where possible to maintain a fine grid distribution at wall boundaries. In a CFD calculation the use of wall functions to calculate shear stresses and turbulence quantities at a wall requires a parameter known as y+ to be maintained between 11 and 500. In the cases considered here the use of adequately refined boundary layer meshes ensures y+ to be maintained under 500 for more than 98% of wall cells. Even when the correct thickness of wall cells is maintained to adequately represent the wall boundary layer the value of y+ depends on local flow conditions. In a large calculation with separation and re-attachment it is impossible to meet this y+ criterion at every wall cell, especially where tetrahedral cells are used. This is not a concern as the cases considered here have high Reynolds numbers. The upper limit of the y+ requirement varies with Reynolds number. For high Reynolds numbers the upper limit could be higher. All cases considered in the present calculations have Reynolds numbers above 4×10^6.